Light at the end of the shower: An all-flavour neutrino point-source search with the ANTARES neutrino telescope

Michael, T.

Tino Michael

Light at the End of the Shower

An all-flavour Neutrino Point-Source Search with the ANTARES Neutrino Telescope

Tino Michael

Light at the End of the Shower

An all-flavour Neutrino Point-Source Search with the ANTARES Neutrino Telescope

Light at the End of the Shower

An all-flavour Neutrino Point-Source Search with the ANTARES Neutrino Telescope

ACADEMISCH PROEFSCHRIFT

ter verkrijging van de graad van doctor
aan de Universiteit van Amsterdam
op gezag van de Rector Magnificus
prof. dr. D.C. van den Boom
ten overstaan van een door het College
voor Promoties ingestelde commissie,
in het openbaar te verdedigen in de Agnietenkapel
op vrijdag 13 mei 2016, te 10:00 uur

door

Tino Michael

geboren te Cottbus, Duitsland

Promotiecommissie

Promotor:	prof. dr. P.M. Kooijman	Universiteit van Amsterdam
Copromotor:	dr. A.J. Heijboer	Nikhef
Overige leden:	prof. dr. ir. E.N. Koffeman	Universiteit van Amsterdam
	dr. R. Bruijn	Universiteit van Amsterdam
	prof. dr. F.L. Linde	Universiteit van Amsterdam
	prof. dr. ir. P.J. de Jong	Universiteit van Amsterdam
	dr. D.F.E. Samtleben	Universiteit Leiden
	prof. dr. ing. B. van Eijk	Universiteit Twente
	dr. C. Finley	Stockholm University

Faculteit der Natuurwetenschappen, Wiskunde en Informatica

Light at the End of the Shower
Set in Latex using Linux Libertine

Cover Image:
Toulon beach during sunset taken 2013 by the author during an on-site shift.

The work described in this thesis is part of the research program of the *Stichting voor Fundamenteel onderzoek der Materie* (FOM), which is part of the *Nederlandse organisatie voor Wetenschappelijk Onderzoek* (NWO).
The research was funded by the vidi project "Exploring the Cosmos with Neutrinos" granted to A. J. Heijboer and was carried out at the *Nationaal Instituut voor Subatomaire Fysica* (Nikhef) in Amsterdam, the Netherlands.

Contents

Chapter 1

A brief History of Astronomy

„Daß ich nicht mehr mit sauerm Schweiß
Zu sagen brauche, was ich nicht weiß;
Daß ich erkenne, was die Welt
Im Innersten zusammenhält“
Heinrich Faust – Faust. Der Tragödie erster Teil
by Johan Wolfgang von Goethe

Every civilisation – from prehistoric times to the present – gazed into the night sky and explored ideas of the nature of the universe. All over the world, early cultures performed methodical observations of the celestial objects like Sun, moon and other planets and associated them to gods and other divine beings [1]. Many of these cultures assembled massive structures that they dedicated to their gods and guided them in their astronomical observations. In the third millennium BCE, Stonehenge was built in present day England. The ultimate purpose of the monument is still a mystery but it has been proposed that many of its standing stones were aligned to different celestial phenomena, like the Sunset of the winter solstice and the Sunrise of the summer solstice. At the same time, the Egyptians carefully aligned the great pyramids towards Thuban, a faint star in the constellation of Draco and the pole star at that time [2]. The Great Temple of Amun-Ra at the Karnak Temple Complex was aligned to the rising of the midwinter Sun [3]. In the second millennium BCE, the Babylonians were the first to recognize the periodicity of astronomical phenomena and used mathematical rules to predict their future behaviour. With this realisation the seasons could be predicted and the right time to plant crops determined. Following the Babylonians, Greek efforts in astronomy were characterised from the beginning by seeking rational, physical explanations for the phenomena they observed. In the fourth century BCE, the Greek developed the first three-dimensional, geometric model of the apparent motion of the Sun and planets. They were among the first to propose a heliocentric model of the solar system in which the Earth also

spins around its own axis. Most of the northern hemisphere star constellations derive from Greek astronomy. During the fourth century BCE, the first star catalogue was created by Chinese astronomers. In 185, they were the first to record a supernova explosion as a "guest star" in their Astrological Annals. They also observed the SN1006 supernova – the brightest apparent magnitude stellar event in recorded history – and the supernova that created the Crab Nebula in 1054.

All those observations had to be performed with the naked eye. It wasn't until 1608 that Dutch eyeglass maker Hans Lippershey invented the refracting telescope and started an astronomical revolution. Galileo Galilei improved on Lippershey's design and discovered the four largest satellites of Jupiter, which was the first observation of planetary satellites besides our own moon. He also discovered the moon craters and Sun spots. Additionally, he observed that Venus goes through light-and-shadow phases very similar to the moon's cycles. He argued that his discoveries were incompatible with the then favoured geocentric model with the Earth fixed at the centre of the universe and would rather support the heliocentric system of the work of Nicolaus Copernicus. Johannes Kepler expanded upon Copernicus' work and devised a system of laws of planetary motion that described the planets' orbits with unprecedented accuracy. Later, Isaac Newton was able to derive Kepler's laws from basic principles of his own laws of motion and gravity. Further significant advances came with the introduction of spectroscopy: In 1814, Joseph von Fraunhofer studied the spectrum of the Sun's light and discovered hundreds of fine, dark lines across the spectrum. In 1859, experiments demonstrated that the same lines can be found in hot gasses on Earth, specific lines corresponding to specific elements. Spectral analyses of distant stars proved that they were similar to our own Sun but with a wide range of temperatures, masses and sizes. With the advent of spectroscopy and the discovery of light beyond the visible spectrum, new fields of astronomy spawned: infrared, radio, x-ray and finally gamma-ray astronomy. Fainter objects could be observed with the use of photography. Our own Sun was found to be part of a whole galaxy of 10^{10} stars: the *Milky Way*. Other galaxies were discovered as well and their apparent receding movement from the Milky Way led to the proposal of an initial Big Bang. This Big Bang theory received more heavily supporting evidence with the measured relative abundance of the elements in the observable universe and an isotropic radio signal in form of an almost perfect black body spectrum – the so-called *Cosmic Microwave Background* discovered by Arno Penzias and Robert Wilson. Placing telescopes on satel-

lites in orbits around Earth allows for a view on celestial objects unobstructed by the scattering and absorption in Earth's atmosphere. While analysing very distant supernovae in the 1990s, it was discovered that the expansion of the universe seems in fact to accelerate.

All the astronomical discoveries described here so far where achieved using light – visible or invisible to the human eye but photons nonetheless. But there are also other messengers that can be used to study the universe. In 1912, Victor F. Hess was the first to discover the increasing ionisation of the atmosphere with increasing altitude and to correctly attribute this effect to cosmic rays [4]: High-energy, fully ionised nuclei accelerated outside of our Solar System. Cosmic rays open access to the highest energies and led to many new discoveries in nuclear and particle physics and gave birth to the field of astroparticle physics. Until today, a large variety of ground-, balloon- and satellite-based cosmic ray observatories have spawned. A broad list of celestial objects has been proposed as additional acceleration sites of such very high energy particles. Among these candidates are supernovae and their remnants, active galactic nuclei and gamma ray bursts. As charged particles, cosmic rays are deflected by the magnetic fields that permeate galaxies and intergalactic space. This makes studying the source of their origin quite tedious. High energy neutrinos are predicted to be created at the same site together with charged cosmic rays. These neutrinos propagate virtually unhindered through the universe and point back precisely to their source. An observation of a cosmic neutrino source presents a powerful tool to study the details of the cosmic ray production mechanism.
The neutrinos' biggest advantage goes hand in hand with their biggest challenge: They only interact weakly with an extremely low cross section. To detect neutrino events in sufficient numbers, huge amounts of target material have to be amassed. Several detectors with a large volume of liquid have been constructed in underground caverns to detect neutrinos. The first cosmic neutrino signal was detected by the Kamioka Observatory, the Irvine-Michigan-Brookhaven detector and the Baksan Neutrino Observatory in February 1987 and could be attributed to the supernova SN1987A which took place in the Large Magellanic Cloud, about 160 000 light years away [5,6]. The only other identified, extraterrestrial neutrino source is the Sun which has been studied most notably by SAGE, GALLEX, the Homestake Experiment [7], Super-Kamiokande [8] and the Sudbury Neutrino Observatory [9]. Both, the Sun and SN1987A, produce neutrinos with energies of only a few MeV. To identify sites of high energy cosmic ray acceleration, the detection of more energetic neutrinos is necessary. Since the expected neutrino flux from such

sites is much lower, even larger detector volumes are needed to accumulate sufficient neutrino numbers. So much larger that it is infeasible to artificially compile the target material. The way out of this dilemma is the use of transparent, naturally occurring environments like the permanent glaciers of the polar regions or bodies of water. In 2013, the research group operating the IceCube detector at the South Pole announced the detection of the first high energy cosmic neutrino signal – even though they are not able to pinpoint the signal to any specific source [10].

The ANTARES detector is the largest deep sea neutrino observatory to date. One advantage of using deep sea water over glacial ice is water's much larger scattering length for photons. This thesis describes a search for cosmic neutrino sources with ANTARES. There are three different types (or flavours) of neutrinos and several possible event signatures in the detector. Until now, most analyses solely relied on one specific detection channel: A muon neutrino transforming into a muon through a charged current interaction. This muon induces Cherenkov radiation along its track which in turn gets recorded by the detector's sensor modules. Other neutrino interactions create short cascades (or showers) of charged particles. Using only muon tracks as a signal channel reduces the detector's sensitivity to a fraction of the interactions cosmic neutrinos can undergo. This is of particular importance since it is expected that *neutrino oscillation* equalises the ratio of the fluxes of the different neutrino flavours ($\Phi_{\nu_e} : \Phi_{\nu_\mu} : \Phi_{\nu_\tau} = 1 : 1 : 1$) while they propagate through open space. In this work, for the first time, all three neutrino flavours and all interactions channels are exploited in a search for cosmic neutrino sources. As a first step, a reconstruction algorithm for electromagnetic and hadronic shower events was developed (chapter 5). Later, these shower events were combined with muon candidates from an already existing muon track reconstruction. On this superset of events, searches for significant clustering were performed (chapter 7). A detection of such a cluster would be a hint for a cosmic neutrino source. In the end, stringent limits for point-like and extended sources could be set (chapter 8).

The successor of the ANTARES detector is called KM3NeT and is currently under construction on two different sites in the deep Mediterranean Sea. It will encompass several cubic kilometres of instrumented volume and consist of thousands of optical modules; each housing not one large but 31 small photomultiplier tubes. A first prototype of this multi-PMT optical module has been deployed within ANTARES. The results from the calibration and analysis of this prototype are presented here as well (chapter 4).

Chapter 2

Neutrino Astronomy

"When did you become an expert on thermonuclear astrophysics?"
"Last night."
Maria Hill, Tony Stark – The Avengers

This chapter quickly positions the neutrino as an elementary particle within the Standard Model of Particle Physics. It describes the observed cosmic ray spectrum and outlines a possible acceleration mechanism and several types of astrophysical objects as source candidates. In the end, a proposed neutrino production mechanism within cosmic ray sources is presented along with a short derivation of neutrino oscillation and the current status of the search for high-energy neutrino sources.

2.1 Neutrinos and the Standard Model

In the beginning of the 20th century – at a time where photon, proton and electron were the only known subatomic particles – the continuous energy spectrum of electrons produced in beta-decays posed quite a headache-causing riddle to many physicists. A number of leading figures – Niels Bohr among them – even thought of giving up conservation of energy to explain the phenomenon. In 1930 Wolfgang Pauli, unwilling to let go of this fundamental principle, proposed the existence of a neutral, light-weight particle which gets emitted together with the electron and called it neutron [11]. This neutron would turn this two- into a three-body decay, solving the mystery of the observed energy spectrum. Enrico Fermi effectively renamed this new particle to *neutrino* at a conference in 1932, resolving the naming ambiguity with the particle that is still today known as neutron. It took until 1956 that Clyde L. Cowan and Frederick Reines finally discovered the electron neutrino with their water and cadmium-chloride-based scintillation detector [12]. With the muon [13] and tau [14] neutrino, two more flavours of this elusive particle have been discovered.

Neutrinos are virtually massless, elementary particles without an electric charge. They only interact weakly with an extremely small interaction cross section. With their charged partners – electron, muon and tau – the neutrinos mirror the three quark pairs. Together, they all represent the fundamental particles of matter.

2.2 Cosmic Rays

Earth's atmosphere gets permanently bombarded by high-energy, charged particles. Direct and indirect measurements of the composition of these cosmic rays (CRs) revealed that they are the fully ionised nuclei of hydrogen (to about 90 %), helium (about 9 %), heavier elements (about 1 %) and a tiny fraction of electrons. A collection of the energy spectra of the different particles collected by various experiments can be seen in figure 2.1. The development of the CR flux as a function of energy can be described with a power law:

$$\frac{dN}{dE} \sim E^{-\gamma}, \tag{2.1}$$

where N is the number of CR particles, E their energy and γ the so-called *spectral index*. The measured energy spectrum follows a power law with a spectral index of $\gamma \approx 2.7$ up to an energy of $E \approx 3 \times 10^{15}$ eV. This point is called the *knee* and constitutes the first break in the spectrum and a change in the spectral index. At energies above the knee, the spectrum can be described with an index of $\gamma \approx 3.1$ up to the second break, called the *ankle*, at $E \approx 10^{19}$ eV. For even higher energies, the flux follows a spectrum with $\gamma \approx 2.7$ again. The most powerful CRs exceed energies of 10^{20} eV.
For particle energies up to 10^{14} eV, CRs can be directly measured above earth's atmosphere with balloon and satellite borne experiments. As the flux decreases with higher energies, indirect detection becomes necessary. Such experiments use the atmosphere as target material and measure the secondary particles from the CR interactions. For energies beyond the ankle, the flux of ultra-high-energy cosmic rays (UHECRs) is so low, only 1 cosmic ray particle hits the earth per square kilometre and century [16]. Instruments with extremely large collecting areas are needed to gather sufficient statistics for events of such high energy. For the Pierre Auger Observatory, 1660 water Cherenkov detectors were distributed in an area of 3000 km^2. An additional 6 fluorescence telescopes are set up at the edges of the instrumented area. With its huge area, it was able to detect 69 CRs with energies above 6×10^{19} eV (the ankle) and compared their arrival directions with the directions of 318

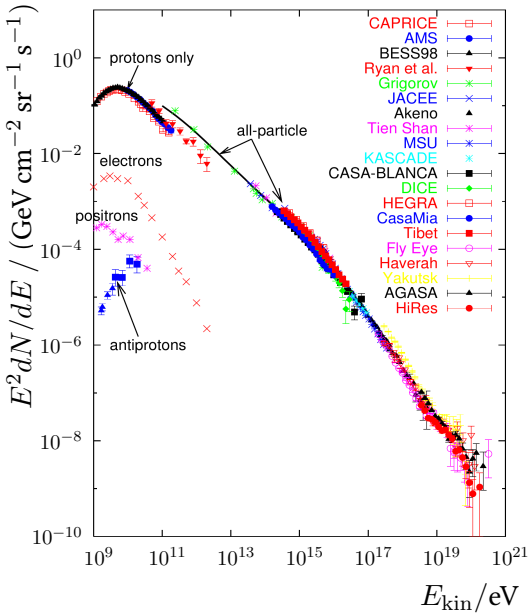

Figure 2.1: The energy spectrum of various kinds of particles constituting cosmic rays. The spectrum follows a power law with different spectral indices depending on the energy. The breaking points are called the knee at $E \approx 3 \times 10^{15}$ eV and the ankle at $E \approx 10^{19}$ eV. Picture taken from [15].

known active galactic nuclei (AGN). Only a weak correlation was found [17]. A skymap of these UHECRs and AGN can be found in figure 2.2.

2.2.1 Cosmic Particle Acceleration

There is general agreement that CRs with energies below 100 MeV originate from the sun [18]. Low energy CRs of galactic origin are effectively blocked out by the solar wind beyond the heliopause in the outer solar system. For energies up to the knee, the most prominent proposal for CR acceleration is the Fermi mechanism [19]: In the collisionless shock wave of two interstellar plasmas with different velocities, charged particles can get accelerated to high energies by repeatedly traversing the shock front. After each crossing, scattering on magnetic irregularities isotropises the particles' velocities with respect to their current host-plasma. Each transition from the unshocked to the shocked medium and back results in an average gain in energy by a constant factor of

$$\frac{\Delta E}{E} = \frac{v_{\mathrm{shock}}}{\mathrm{c}}, \tag{2.2}$$

where c is the speed of light in vacuum and v_{shock} the velocity of the shock front with respect to the stationary interstellar medium. This mechanism is also called *first order Fermi mechanism* because the gain in energy depends

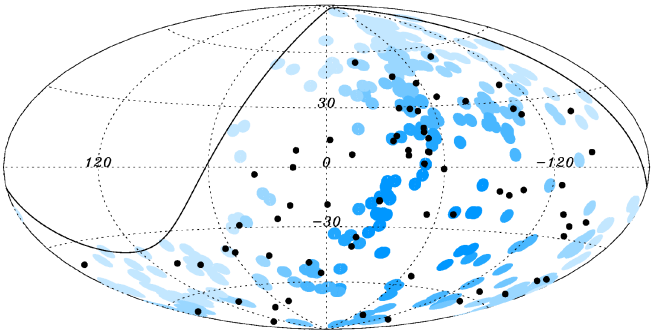

Figure 2.2: Sky map of 69 cosmic rays with energies $E \geq 55$ EeV detected by the Pierre Auger Observatory (black dots) and the comparison of their directions to 318 known Active Galactic Nuclei (blue circles); all plotted in galactic coordinates. A darker shade of blue means a longer relative exposure of that source. Figure taken from [17].

linearly on the plasma's velocity. A schematic description of this mechanism is shown in figure 2.3. For a more detailed mathematical derivation of this mechanism see [20]. The acceleration stops when the particles' gyroradii become bigger than the plasma cloud so that they can no longer be contained and leak out or when the plasma shock itself runs out of energy and dies out.

This mechanism became very popular because it properly predicts the CR spectral index γ: A first order calculation yields a value of $\gamma = 2.0$ to 2.4. The difference to the observed, steeper CR energy spectrum with $\gamma \approx 2.7$ can be explained with the leaky box model [21], according to which high-energy CR particles escape the confinement of our galaxy and are no longer accessible for detection on earth.

To date, there is no consensus on which kind of astrophysical object is responsible for CR energies above the knee. For energies higher than 10^{18} eV it is generally assumed that the CR accelerators are of extragalactic origin. A number of candidates are described in the following sub-sections.

2.2.2 Galactic Accelerators

Many galactic gamma-ray sources show non-thermal photon spectra which hints at active acceleration of charged particles. Galactic sources are thought to be responsible for the majority of CRs below the knee. There is a broad list of proposed candidate sources. The most prominent are described briefly in the following.

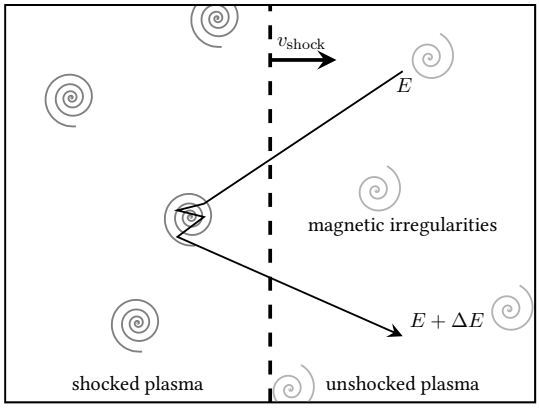

Figure 2.3: Sketch of the acceleration process in the first order Fermi mechanism. A charged particle with energy E (solid black line) drifts across the shock front (dashed line, moving with velocity v_{shock} with respect to the unshocked plasma) from the unshocked into the shocked plasma. Here, it gets scattered on magnetic irregularities (grey spirals) and drifts back to the unshocked plasma. During each scattering process to the shocked plasma and back it gains on average a factor of $v_{\mathrm{shock}}/\mathrm{c}$ in energy: $\Delta E = E \cdot v_{\mathrm{shock}}/\mathrm{c}$.

Supernova Remnants When a star has burned up all its fuel or accretes too much material from an accompanying partner it collapses under its own weight and ultimately explodes in a supernova, ejecting large amounts of material in a form of a plasma shock wave into the vastness of space. The expanding shell of the former star is called supernova remnant (SNR). Charged particles accelerate by scattering back and forth across the produced shock front. SNRs are the most popular candidate to explain the cosmic ray spectrum below the knee since applying the Fermi mechanism predicts the proper spectral index and power output observed in CR measurements. Two popular examples of SNRs are RXJ0852.0-4622 and RXJ1713.7-3946. Both have been identified as gamma-ray sources [22, 23].

Pulsar Wind Nebulae Pulsar wind nebulae (PWN) are clouds of interstellar dust with a pulsar at their centre. The pulsar fuels the nebula with a stream of electrons which get accelerated in the pulsar's rapidly rotating magnetic field. Young PWN can be found still surrounded by the SNR shell from the SN that created the pulsar. The most prominent example of a PWN and first TeV-gamma-ray source detected is the Crab Nebula [24]. The nebula's photon spectrum is well described by purely

leptonic acceleration mechanisms, so no hadronic cosmic rays are expected from this source. The first PWN detected with its SNR still intact is Vela X [25]. Even though purely leptonic models fit well also for Vela X, it has been suggested that a significant fraction of hadrons can get accelerated within the nebula resulting in a considerable number of CRs emanating from this source [26].

Microquasars Microquasars comprise an about-solar-mass neutron star or black hole that accretes material from an accompanying star. The matter falling into the compact object creates an accretion disk with relativistic jets perpendicular to it. If not only leptons but also hadrons get accelerated in this jet, CRs and neutrinos could be emitted from such objects. Neutrino fluxes for a number of galactic microquasars have been predicted [27].

Galactic Centre The central region of our galaxy is interesting for many fields of astronomy and astrophysics. The H.E.S.S. Observatory found several new gamma-ray sources in this region [28]. Of particular interest is of course our very own super-massive black hole (SMBH) that defines the Galactic Centre (GC), Sagittarius A*. Due to the high concentration of candidate sources, it is probable that a diffuse signal from that region will be detected first before identifying individual sources.

Fermi-Bubbles Above and below the centre of our galaxy, huge regions of X- and gamma-ray emission have been detected by the Fermi telescope [29, 30]. These *Fermi Bubbles* reach about 25 000 light years perpendicular to the galactic disc and are assumed to be the jets of the SMBH, Sagittarius A*.

2.2.3 Extragalactic Accelerators

Cosmic rays with energies above the ankle are assumed to be accelerated by sources outside of our own galaxy. Strong source candidates are AGN and gamma-ray bursts (GRBs).

Active Galactic Nuclei It is assumed that most – if not all – galaxies contain a SMBH (10^6 to 10^{10} Solar Masses) in their centre [31]. These black holes form a disc of infalling matter around themselves. A very efficient conversion from potential and kinetic energy to radiation can take place during the accretion causing AGNs to be persistently extremely luminous objects that radiate in a broad range of the electromagnetic

spectrum. AGN form highly collimated, relativistic jets perpendicular to their accretion disc (or parallel to the black hole's spin axis) and are one candidate for high and ultra-high-energy CR acceleration. If the jet axis is aligned towards the direction of the observer (i.e. Earth), such objects are also called Blazars.

Gamma-Ray Bursts GRBs are the brightest and most energetic electromagnetic phenomena since the Big Bang. They can last from fractions of a second to several minutes [32]. Some extraordinary events can even last several hours [33]. The origin of GRBs is still a mystery, though it is believed that most constitute a narrow beam of energy caused by the explosion of a rapidly rotating high-mass star or the merging of two neutron stars. If protons are accelerated within GRBs, they could be the source of the highest energy CRs [34].

2.2.4 Beyond the Ankle – or: The GZK-Cutoff

At the highest energies, extreme-energy cosmic rays (EECR) start to scatter on the Cosmic Microwave Background and produce pions via the Delta-resonance [35, 36]:

$$p + \gamma_{\text{CMB}} \to \Delta^+ \to p + \pi^0 \tag{2.3}$$
$$\to n + \pi^+. \tag{2.4}$$

This process slowly drains the proton's energy and effectively limits the range of EECR to about 160 million light years. The predicted cutoff energy coincides well with a rapid drop in the spectrum of the CR energies (see again figure 2.1).
It is still a mystery what kind of astrophysical objects should be capable of accelerating CRs to energies beyond 5×10^{19} eV. Candidates that have been proposed include fast spinning neutron stars and AGN with spinning SMBHs at their centre. More exotic models encompass decays or annihilations of super-massive particles from the early universe.

2.3 Neutrino Production at Astrophysical Acceleration Sites

Because of their inherent electric charge, CRs are subject to deflection by galactic and intergalactic magnetic fields. Those fields effectively randomise

the arrival direction of the particles and make it virtually impossible to associate them with their astrophysical source for all but the highest energies. Even for UHECRs, the expected offset between the source and the particle's arrival direction can be several degrees. This is one of the major motivations to detect and identify cosmic neutrinos which are necessarily created at astrophysical sites that accelerate charged particles: Considering hadronic models for the acceleration process, protons and neutrons interact with other nuclei and the acceleration site's ambient photons. In the simplest case, these interactions produce pions via Delta-resonances[1]:

$$p + \gamma \to \Delta^+ \to p + \pi^0 \tag{2.5}$$
$$\to n + \pi^+ \tag{2.6}$$

or directly through nucleon-nucleon interactions:

$$p + p \to p + p + \pi^0 \tag{2.7}$$
$$\to p + n + \pi^+ \tag{2.8}$$

$$p + n \to p + n + \pi^0 \tag{2.9}$$
$$\to p + p + \pi^-. \tag{2.10}$$

The charged pions created in these processes subsequently produce neutrinos during their decay chains:

$$\pi^- \to \mu^- + \bar{\nu}_\mu \to e^- + \bar{\nu}_e + \nu_\mu + \bar{\nu}_\mu, \tag{2.11}$$
$$\pi^+ \to \mu^+ + \nu_\mu \to e^+ + \nu_e + \nu_\mu + \nu_\mu, \tag{2.12}$$

while neutral pions simply decay into photon pairs:

$$\pi^0 \to \gamma + \gamma. \tag{2.13}$$

Thus, hadronic acceleration models automatically predict both gamma-ray and neutrino emissions at the same CR acceleration sites. Adding up the neutrinos from the pion-decays yields a flavour ratio of $(N_{\nu_e} : N_{\nu_\mu} : N_{\nu_\tau})_\mathcal{S} = (1 : 2 : 0)_\mathcal{S}$ at the source, while the energy spectrum of the produced neutrinos follows the E^{-2} spectrum of the protons, only that it is shifted by a factor of $\varepsilon \approx 0.05$ [37].

[1] This is the same process that causes the GZK-cutoff for EECRs only that now the ambient photons are of higher energy themselves lowering the necessary CR energy for the interactions.

2.3.1 Neutrino Oscillation and its Implications

When they were discovered, neutrinos were thought to be massless. Nowadays, a non-zero rest mass is known from observations of oscillations between the neutrino flavours. Neutrinos interact in their so-called *flavour eigenstates*, $|v_\alpha\rangle$ – with $\alpha \in \{e, \mu, \tau\}$ – but propagate as *mass eigenstates*, $|v_j\rangle$ – with $j \in \{1, 2, 3\}$. The flavour eigenstates are linear combinations of the mass eigenstates described by the PNMS-matrix, $U_{\alpha j}$ [38, 39]:

$$|v_\alpha\rangle = \sum_j U^*_{\alpha j} \, |v_j\rangle. \tag{2.14}$$

The propagation through space of the mass eigenstate can be described by plane wave solutions in the form of

$$|v_j(t)\rangle = \mathrm{e}^{-i(E_j t - \vec{p}_j \vec{x}_j)} \cdot |v_j(0)\rangle, \tag{2.15}$$

with E_j, the neutrino energy, $\vec{p}_j$ and $\vec{x}_j$ the three-dimensional vectors for momentum and position. The probability that a neutrino, produced with a flavour α, propagates through space for a time t – and distance L – and gets detected as flavour β is therefore:

$$P(v_\alpha \to v_\beta) = |\langle v_\beta | v_\alpha(t)\rangle|^2 = \sum_j U^*_{\alpha j} U_{\beta j} \mathrm{e}^{-i m_j^2 \frac{L}{2E}}, \tag{2.16}$$

with m_j as the mass of the mass eigenstate j. It is instructive to consider the oscillation between only two flavour eigenstates, α and β with two mass eigenstates, j and k. The oscillation probability then becomes (in natural units):

$$P(v_\alpha \to v_\beta) = \sin^2(2\vartheta_{jk}) \cdot \sin^2\left(\Delta m^2_{jk} \frac{L}{4E}\right), \tag{2.17}$$

with ϑ_{jk} as the *mixing angle* and $\Delta m^2_{jk} = m^2_j - m^2_k$ as the mass-squared difference between the two mass eigenstates. It is evident from this equation, that any oscillation experiment that observes the vanishing or arising of flavours can only be sensitive to the mass-squared differences between the mass eigenstates but not the masses themselves.
This neutrino oscillation would effectively equalise a source flavour composition of $(1 : 2 : 0)_\mathcal{S}$ – from a simple pion-decay model as mentioned earlier – so that a measurement on earth would yield a ratio of approximately $(1 : 1 : 1)_\mathcal{E}$ [40]. For any linear combination of $(0 : 1 : 0)_\mathcal{S}$ and $(1 : 0 : 0)_\mathcal{S}$ as the source composition, the flux ratio measured on earth lies linearly between

$(0.6 : 1.3 : 1.1)_{\mathcal{E}}$ and $(1.6 : 0.6 : 0.8)_{\mathcal{E}}$. A contribution of tau neutrinos at the source has a negligible effect on the flavour composition detectable on earth. Though, only a contribution of 10^{-4} to 10^{-2} is expected at astrophysical sources in the first place. Measuring the flavour composition on earth would allow us to draw conclusions on the flavour composition and therefore the physical conditions at the source.
Initially, neutrino telescopes focused on the detection of muons created by charged current interactions of muon neutrinos (see section 3.1.1 for details on the different interactions) since it was assumed that muon neutrinos constitute the majority of the cosmic neutrino flux. After the discovery of neutrino oscillation, it became clear that the muon neutrino charged current channel might only be a small fraction of the detectable signal. The effort shifted to also detect and identify the other neutrino flavours and neutral current interactions in general. This extension of the sensitivity has not only the advantage to drastically increase the number of valuable events in the detector (a challenge with which every high-energy astroparticle experiment has to cope) but also gives access to the basically background free channel of tau neutrino charged current interactions. Due to the lack of high-energy tau neutrinos in any reasonable quantity from terrestrial sources, their observation in a neutrino detector would be strong evidence for their cosmic origin.

2.3.2 The IceCube Signal

In 2013, the IceCube neutrino telescope was the first to detect a number of high-energy neutrinos that are not compatible with the atmospheric background [10]. The majority of these events are shower-like (28 showers compared to 7 tracks) with a median angular resolution around 15°. Even though quite a few of these neutrinos seemingly originate from a common point close to the GC, their low resolution makes associating them to a specific source a difficult task, that to date has not been successful. The significance of this cluster near the GC under the hypothesis of a point-source was determined to $7.2\,\%$ when only shower events are considered and $84\,\%$ when combining track and shower channels.
Assuming an isotropic flux, the energy spectrum has been fitted to a spectral index of $\gamma = 2.3$, which is slightly softer than the traditionally assumed $\gamma = 2$. A softer energy spectrum would mean a higher contribution of lower-energy neutrinos to, which ANTARES has superior sensitivity compared to IceCube.

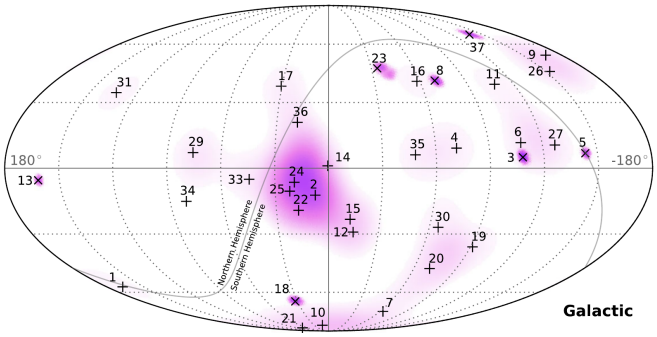

Figure 2.4: Arrival directions in Galactic coordinates of the high-energy neutrino candidates observed by IceCube. Different markers denote different event topologies; namely tracks ($\times$) and showers ($+$). Purple areas show the significance of a point-source likelihood test; deeper shades mean a higher significance. The large spot near the Galactic Centre has a significance of $7.2\,\%$ (considering only showers) and $84\,\%$ (considering track and shower events). Figure taken from [10].

Muons generated in the upper atmosphere by cosmic ray interactions constitute one of the major backgrounds for neutrino telescopes. For this reason, they usually "look downward" and use the earth as a shield against these muons; which can penetrate several kilometres of ice and water but not the Earth as a whole. For such downward-looking analyses, the GC is actually not in IceCube's field of view. To look above their local horizon and study the GC, the analysis has to limit itself to *high-energy starting events* (HESE) which significantly reduces their sensitivity. The ANTARES detector located in the deep Mediterranean Sea, on the other hand, has the GC for the majority of its duty cycle in full view (see section 3.2.6). This makes ANTARES an ideal candidate for a follow-up study of the IceCube "hotspot".

Conclusion

Neutrinos are virtually massless, elementary particles without an electric charge. They only interact via the weak interaction; therefore, they can escape very dense sources and cross huge amounts of matter unobstructedly. Thus, their energy spectrum measured on earth matches the spectrum at their production site. Cosmic neutrinos are thought to be produced along with cosmic rays at various astrophysical objects like supernova remnants, active galactic nuclei or gamma-ray bursts. Unlike cosmic rays, which are fully ionised nuclei, neutrinos do not scatter at the cosmic microwave background nor do they get deflected by magnetic fields permeating interstellar and intergalactic space. Instead, they point straight back to the source of their production. Detecting ultra-high-energy neutrinos and attributing them to a common source would also be strong, indirect evidence for a site of cosmic ray acceleration. Studying the neutrino energy spectrum will be a powerful tool to distinguish between the various models that try to explain the shapes and features of the cosmic ray spectrum. The IceCube collaboration already detected several neutrinos of very high energy but was so far unable to attribute them to a specific source.

Chapter 3

The ANTARES Experiment

A race of hyper-intelligent, pandimensional beings got so fed up with the constant bickering about the meaning of life that they commissioned two of their brightest and best to design and build a stupendous supercomputer to calculate the answer.
The Hitchhiker's Guide to the Galaxy by Douglas Adams

Building and operating a large scale neutrino telescope is quite a complex endeavour. One has to define a signal which is to be measured and understand the physical processes involved in this measurement. A detector capable of measuring this signal has to be designed and constructed; a detector that has to be read out and its signals acquired and stored. As with any modern particle physics experiment, a detailed simulation of the processes and the detector is needed to ensure proper understanding of everything that is going on. Finally, the observed events need to be reconstructed from the detector response and put in a format that can be easily used in high level analyses. This chapter attempts to explain all these steps in as much detail as possible and necessary to provide a proper basis for the chapters to come.

3.1 Detection Principle

Neutrinos have no electric charge and only interact via the *weak interaction*. They can only be detected indirectly through their interaction with the matter they traverse. In case of deep sea neutrino telescopes, this would be water or the rock of the seabed below. Neutrinos can exchange Z or $W^{\pm}$ bosons with ambient atoms and create electrically charged particles in the process. Given that enough energy is transferred to these charged particles, they can reach velocities that are higher than the speed of light in water. In such cases, they will induce Cherenkov radiation: a dim light predominantly in the deep blue to part of the UV spectrum. This light can be picked up by a three-dimensional array of photosensitive detector modules. Subsequently, the po-

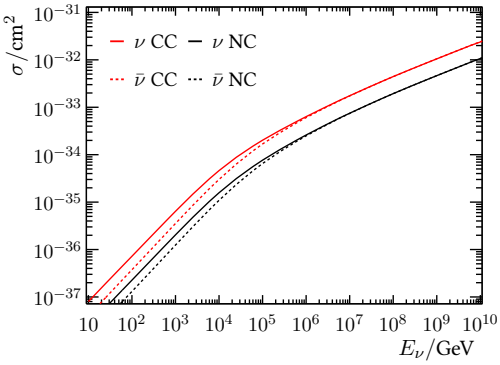

Figure 3.1: Energy-dependent cross sections for neutrinos (solid) and antineutrinos (dashed) scattering on nucleons via a W boson (CC, red) or a Z boson (NC, black). Figure reproduced from [41].

sition of these modules together with the intensity of the measured light and its arrival time can be used to reconstruct the neutrino direction. Due to the neutrinos' extremely small interaction cross section (see figure 3.1 for the energy-dependent neutrino cross sections), a huge amount of target material is necessary to observe a sufficient number of interactions. The depths of the Mediterranean Sea represent a suitable target material: The clear water is transparent for photons in the relevant frequency range and several hundred metres below the surface no daylight can penetrate.

3.1.1 Neutrino Interactions

There are several fundamental neutrino interactions that can be detected with an underwater neutrino telescope. In general, the interactions can be classified as *charged current* (CC, exchange of a charged $W^\pm$ boson) and *neutral current* (NC, exchange of a neutral Z boson). Many of the different interactions have a distinct signature in the detector allowing us to differentiate between them. All the fundamental interactions relevant for a neutrino telescope are presented in figure 3.2.

Muon Neutrinos A muon neutrino can exchange a $W^\pm$ boson with a nucleus from the surrounding medium. While the nucleus disintegrates into a hadronic shower, the neutrino turns into an electrically charged muon (figure 3.2 top left). Depending on the energy that has been transferred to the lepton, the muon can propagate for a few metres (at $E_\mu \approx 1\,\mathrm{GeV}$) up to several kilometres (at $E \gtrsim 1\,\mathrm{TeV}$). The direction of the muon momentum does not necessarily point in the exact same direction as the parent neutrino; the average angle between their momenta rather depends on the energy and can be described as $\langle \measuredangle(\vec{p}_\nu, \vec{p}_\mu) \rangle = 0.7°/(E/\mathrm{GeV})^{0.6}$ [42]. This scattering

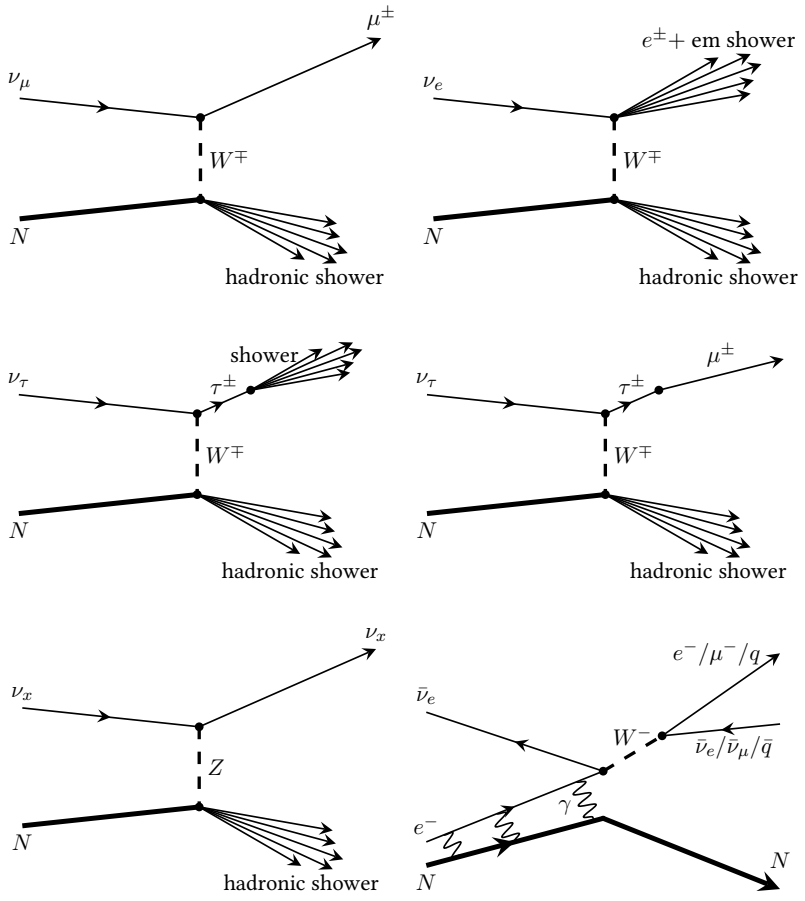

Figure 3.2: Feynman diagrams of the relevant neutrino interactions in a deep sea Cherenkov neutrino detector. Except for the bottom right plot, a distinction between particle and antiparticle is not made. **Top Row:** Left: A muon neutrino exchanges a W boson with an ambient nucleus and turns into a muon. Right: An electron neutrino exchanges a W boson with an ambient nucleus and turns into an electron which creates an electromagnetic shower. **Middle Row:** Left: A tau neutrino exchanges a W boson with an ambient nucleus and turns into a tau lepton. The tau quickly decays into an electron or a quark pair and creates a shower. Right: A tau neutrino exchanges a W boson with an ambient nucleus and turns into a tau lepton. The tau quickly decays into muon. Additionally produced neutrinos are not shown. **Bottom Row:** Left: A neutrino exchanges a Z boson with an ambient nucleus without changing its type. Right: The Glashow Resonance – An electron antineutrino with an energy around $E_\nu = 6\,\text{PeV}$ interacts with an electron from ambient atoms and creates a W^- boson. The boson either decays leptonically into an electron and electron antineutrino pair ($e + \bar{\nu}_e$) or muon and muon antineutrino pair ($\mu + \bar{\nu}_\mu$) or hadronically into a quark-antiquark pair ($q + \bar{q}$). The nucleus stays intact.

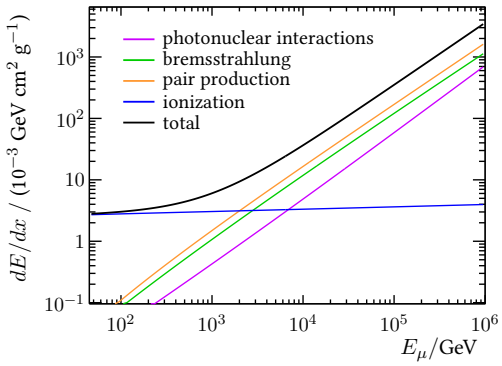

Figure 3.3: The energy-dependence of a muon's various energy losses in water. Shown are losses due to ionization of ambient atoms and through stochastic processes. Figure reprocessed from [43].

angle is therefore only relevant for the lowest energies. Along its way, the muon loses energy through a number of different processes. An overview of the most dominant ones and their dependence on the muon's energy can be seen in figure 3.3. The process used to identify and reconstruct the muon is the Cherenkov radiation which is emitted under a characteristic angle of $\vartheta_c \approx 42°$. Graphically, the muon pushes a cone of light along its track resulting in a clean detector signature. Due to the muon's long track length, the neutrino interaction does not have to happen very close to the detector but can be far away as long as its direction points right through it. This effectively increases the detector's sensitivity beyond the instrumented volume. On the other hand, only a fraction of the muon energy is emitted inside the detector which makes it considerably harder to estimate the total muon energy.

Electron Neutrinos If the initial neutrino interacts via CC in its electron flavour state, the resulting electron has only a very short path length. It loses its energy through *bremsstrahlung*. The generated photons have enough energy to in turn produce additional electrons and positrons via pair production. This process quickly drains the electron's energy so that the resulting *electromagnetic shower* has a typical length no longer than a few metres (figure 3.2 top right). Many particles that are generated within the showering process are relativistic and therefore induce Cherenkov radiation themselves; however since they are not all propagating in the same direction, the resulting light signature looks more like a burst of light in the general forward direction. The shower's short length restricts this channel's effective detection volume to the immediate surrounding of the detector but the concentrated deposit of all the neutrino's energy provides a better handle on the measurement of its energy.

Tau Neutrinos The tau lepton, produced by tau neutrino CC interactions, is very short-lived ($\tau_\tau \approx 2.9 \times 10^{-13}$ s [18]). Depending on its energy, it can travel a few tens of metres before it either decays leptonically into an electron or muon (ignoring the additionally created neutrinos) or hadronically into a quark-antiquark pair. These decay products behave like their directly produced counterparts: The muon produces a long, straight track. The electron and quark-pair produce short showers. Together with the shower from the initial nucleon disintegration, the decays produce two detector signatures very distinct to tau neutrino interactions: two showers whose separation depends on the tau energy (figure 3.2 middle left) – called *double bang* – and an initial shower with a long muon track (figure 3.2 middle right) – called *lollipop*.

Neutral Current Interactions Any neutrino, independent of its flavour or particle/antiparticle state, can exchange a Z boson with a close-by nucleus. The nucleus breaks up and creates a hadronic shower as with any other depicted interaction so far. Though in this case, the neutrino does not change its type. In these neutral current interactions, only a fraction of the neutrino energy is deposited in the detector. The rest is carried away by the neutrino (figure 3.2 bottom left).

Glashow Resonance If an incident electron antineutrino has an energy around $E_{\bar{\nu}_e} \approx 6\,\text{PeV}$, its centre of mass energy with an ambient, "stationary" electron equals the mass of a W^- boson and the production probability of such a boson is highly amplified. This effect is called *Glashow resonance*. The W^- boson then decays through its usual channels (figure 3.2 bottom right).

All of the fundamental neutrino interactions can (hadronic W-decay from Glashow resonance) or will (all others) result in a hadronic cascade. Either because the exchanged boson disintegrates the target nucleus or because of the hadronic decay of one of the particles created in the initial interaction (i.e. tau-lepton or W^- boson). While an electromagnetic shower consists exclusively of electrons, positrons and photons, a hadronic shower contains considerably heavier particles like pions and kaons. Neutral pions can decay into photon pairs and add an electromagnetic component to the hadronic shower. Kaons and charged pions can decay into muons which usually leave the shower, carry away energy and induce Cherenkov light along their path. Due to their heavier constituents and the random muon production, hadronic showers have a more irregular and prolonged shower profile than electromagnetic showers.

3.1.2 Cherenkov Radiation

When a charged particle moves through water or any other dielectric medium, it polarizes the atoms around its path. After the particle passed, these excitations relax back into equilibrium perturbing the surrounding electromagnetic field. If the charged particle moves sufficiently slowly, the perturbations interfere destructively so that no electromagnetic radiation is emitted. If, on the other hand, the charged particle passes the polarized atoms faster than they can adapt to the field changes imposed by the particle, the excitations relax in the wake of the speeding particle. Neighbouring atoms then are always in a similar phase of their relaxation and perturb the electromagnetic field in a coherent manner. The perturbations interfere constructively and a cone-shaped shock-front emerges, radiating off energy as *Cherenkov radiation*. Specifically, the velocity the charged particle has to surpass for this radiation to emerge is the *phase velocity* of light in the ambient medium, v_p. The light will always be emitted under an acute angle, ϑ_c, with respect to the momentum of the particle inducing the effect. The value of this angle depends on the velocity of the speeding particle, v, and the refractive index of the medium, n_p. It can be parametrised as

$$\cos(\vartheta_\mathrm{c}) = (n_\mathrm{p} \cdot \beta)^{-1}, \tag{3.1}$$

with $\beta = v/\mathrm{c}$, $v_\mathrm{p} = \mathrm{c}/n_\mathrm{p}$ and c as the speed of light in vacuum. A simplified sketch of this effect is drawn in figure 3.4. For a neutrino telescope, the velocity of the particle is approximately the vacuum speed of light ($\beta \approx 1$) in the whole relevant energy range. For water in the deep sea with a refractive index of $n_\mathrm{p} \approx 1.35$ the characteristic *Cherenkov angle* then is $\vartheta_\mathrm{c} \approx 42°$. In first order, the Cherenkov light's intensity is proportional to the frequency with a cut-off in the ultra-violet (UV). Most of the photons are therefore emitted in the blue and UV range where water is also most transmissive.

3.2 The ANTARES Detector

The ANTARES (**A**stronomy with a **N**eutrino **T**elescope and **A**byss environmental **Res**earch) detector [44] aims to detect the Cherenkov light induced by electrically charged particles produced in neutrino interactions. It is the biggest neutrino detector in the northern hemisphere and the world's first deep sea neutrino telescope. It is situated in the Mediterranean Sea at a depth of about 2500 m; approximately 40 km off shore of Toulon, France at 42° 48′ N, 6° 10′ E (see figure 3.5 for a map). The detector was completed in mid 2008 but it took already data during its construction throughout 2007 back to early March 2006 when the first line was deployed.

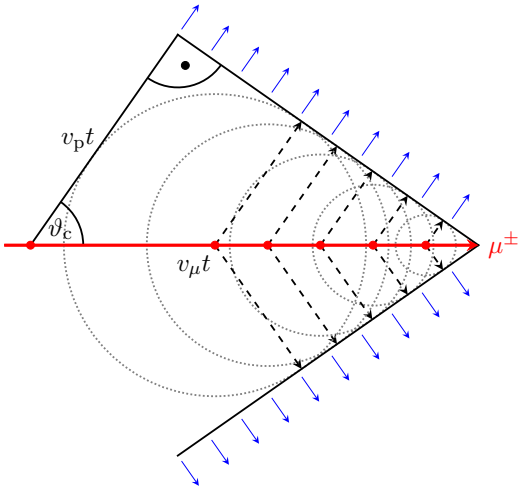

Figure 3.4: Simplified schematic of the Cherenkov effect: A charged particle (here a muon, red line) travels with a velocity greater than the light's phase velocity in this medium: $v_\mu > v_\mathrm{p} = \mathrm{c}/n_\mathrm{p}$. It polarizes the surrounding atoms (red dots) which create perturbations in the electric field (dotted circles). In the time the muon travels the distance $v_\mu t$, these perturbations only propagate $v_\mathrm{p}t < v_\mu t$. The perturbations from the different atoms overlap and create a wave front in form of Cherenkov light (blue arrows). The light propagates with a characteristic angle ϑ_c with respect to the muon direction.

3.2.1 Detector Layout

The detector consists of 12 almost 500 m long, flexible lines (or strings) which are anchored at the sea floor to a dead weight on one end and pulled up straight by a buoy on the other. The lines are horizontally separated by about 60 m (see figure 3.6 for a schematic of the whole detector). Each string is connected to a junction box which provides it with electrical power and connects it to the shore station via an optical data transfer interface. Starting 100 m above the sea floor, every line holds an array of 25 storeys with an inter-storey distance of about 14.5 m. On each storey-position, a metal frame is installed that holds a *local control module* (LCM) and has three optical modules (OMs) attached. The LCMs house electronics and are connected to the OMs. The OMs are horizontally arranged around the LCM with an equal spacing of 120° and face 45° downward (see figure 3.7 for a photograph and a schematic). The upper 5 storeys of line 12 hold acoustic neutrino detection hardware [45] and are not equipped with any OMs. This results in a total of

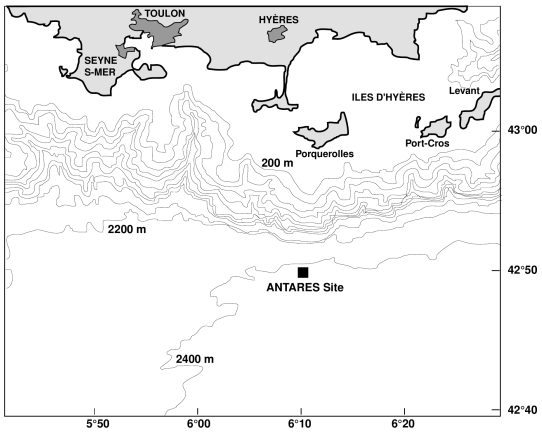

Figure 3.5: The location of the ANTARES detector in the Mediterranean Sea. At a depth of 2.4 km the site is about 40 km off the shore of Toulon, France. The location is marked with black square.

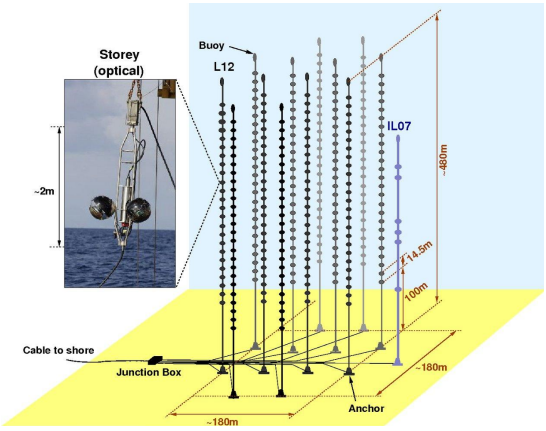

Figure 3.6: Schematic view of the deep sea ANTARES detector: 12 lines with 25 storeys each. Every story houses 3 OMs with a single, large PMT except for the upper 5 stories of the last string; making a grand total of 885 OMs. The instrumentation line carries additional, oceanographic and acoustics equipment.

885 OMs in the detector's final configuration. The OMs consist of pressure-resistant glass spheres with a diameter of 43 cm and a single Hamamatsu photomultiplier tube (PMT) with a photocathode area of 500 cm^2 [46, 47] (see figure 3.8 for a photograph and a schematic view). The photocathode is sensitive to photons with wavelengths between 300 nm and 600 nm, so it matches the frequency range of the Cherenkov radiation. To prevent the Earth's magnetic field from disturbing the electron currents within the PMT and deteriorate the measurements, the whole PMT is surrounded by a cage of high-permeability mu-metal. The PMT is optically connected to the glass through an optical gel with a refractive index of 1.4.

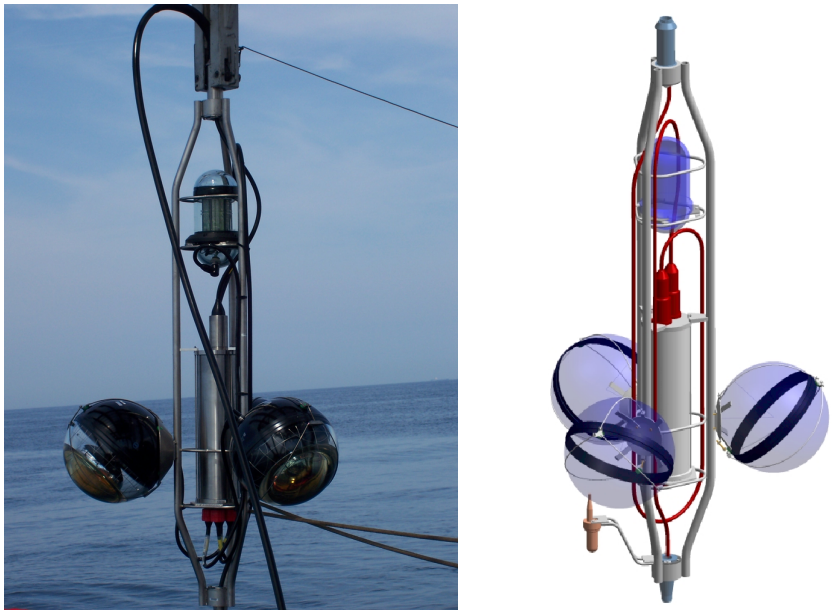

Figure 3.7: The ANTARES LCM: **Left:** a photograph during the deployment and **Right:** a computer model of the module. Visible are the three-pronged titanium structure and electronics cylinder in the middle (in grey), the three OMs around it (blue spheres) and the electro-optical interface (red cables). A number of LCMs are additionally equipped with hydrophones (orange, bottom left) and LED-flashers (blue cylinder at the top).

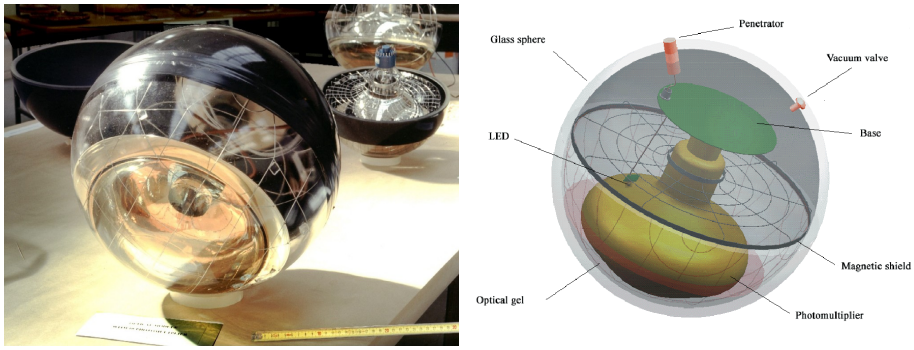

Figure 3.8: The ANTARES OM: **Left:** a photograph of a module after assembly and **Right:** a schematic view of the model's inside.

3.2.2 Data Acquisition

The data acquisition begins with a photon hitting the photocathode area and kicking out an electron. This electron gets accelerated by the PMT's internal electric field and creates an avalanche of secondary electrons on the dynodes inside the tube (hence: photomultiplier tube). The consistency of the time this process takes has a major impact on the time resolution itself. The RMS spread of this time distribution, the *transit time spread* (TTS) has been determined to be 1.3 ns. The electron signal is read out at the base of the PMT as a current spike and digitised by a custom-made front-end chip called *Analogue Ring Sampler* (ARS). Such PMT-level signals are referred to as *hits*. Each PMT is associated with two of these ARS which work in conjunction in a token ring configuration to reduce the impact of the chip's dead time. A local clock on each ARS provides every hit with a time stamp. The ANTARES experiment follows an all-data-to-shore policy: Every hit above a certain threshold – usually corresponding to 0.3 of the mean pulse height produced by a single photon – is collected and arranged into time frames of 104 ms by a Field Programmable Gate Array (FPGA). Subsequently, the time frames are separately sent to shore by a dedicated CPU inside the LCM. The data from every five consecutive LCMs is combined into a single stream and sent to the on-shore computer farm through the main electro-optical cable. For this process, a Dense Wavelength Division Multiplexing (DWDM) technique is used which assigns every stream a separate wavelength and sends them all together over the same optical fibre.

3.2.3 Trigger

Every signal detected by a PMT that passes a pre-determined threshold is digitised and sent to shore. These low-level hits are referred to as L0-hits. Not every time frame contains potentially interesting physics events. To save disc space and later analysis time a number of fast online algorithms filter all incoming data for specific hit patterns. Those algorithms are called *trigger*.
Hits from optical background are usually uncorrelated in time and of low intensity. A first hit pre-selection searches for coincidences on the same storey. If two or more L0-hits on one storey occur within 20 ns, they are combined to a L1-hit. Single hits that surpass a given threshold (usually a signal corresponding to 3 photoelectrons, PE) are picked up as an L1 as well. This set of L1-hits is fed to the actual triggers. Two specific triggers form the standard run set-up. They are referred to as T3 and 3N. The T3 trigger searches for coincidences of L1-hits on adjacent and next-to-adjacent storeys. The co-

incidence window here is 80 ns per storey separation. An event passes the T3 trigger when two of such L1-coincidences have been detected. A more stringent version is the 2T3 trigger which requires four distinct clusters of L1-coincidences.
The 3N trigger makes use of the fact that Cherenkov photons induced by a muon are correlated in space and time. In a first step, all pairs of hits are checked against the criterion

$$|t_i - t_j| \leq \frac{\mathrm{c}}{n_\mathrm{g}} \cdot r_{ij} + 20\,\mathrm{ns}, \tag{3.2}$$

where t_i, t_j are the times of hit i and j, $v_\mathrm{g} = \mathrm{c}/n_\mathrm{g}$ is the group velocity of light in water and r_{ij} the distance between the OMs that recorded the two hits. The additional 20 ns slightly loosen the strict causality criterion to account for potential photon scattering and miscalibration of the time-stamping. If at least five L1-hits pairwise fulfil this inequality, a more stringent criterion is applied. Here, the trigger scans over a coarse, isotropic grid of 210 directions and checks whether any hits are compatible with a hypothetical muon coming from that direction. The time t_i a photon arrives at a PMT can be expressed as:

$$t_i = t_0 + \frac{1}{\mathrm{c}}\left(z_i - \frac{r_i}{\tan(\vartheta_\mathrm{c})}\right) + v_\mathrm{g}\frac{r_i}{\sin(\vartheta_\mathrm{c})}. \tag{3.3}$$

Here, t_0 is the time at which the muon passes $z_i = 0$ and r_i is the assumed muon track's distance of closest approach to the hit PMT. The expected time difference between two hits on different PMTs can then be expressed as:

$$|t_i - t_j| \leq \frac{z_i - z_j}{\mathrm{c}} + \frac{R_{ij}}{\mathrm{c}}\tan(\vartheta_\mathrm{c}) + 20\,\mathrm{ns}, \tag{3.4}$$

with R_{ij} as the distance between PMTs i and j perpendicular to the assumed muon direction. Also here, an offset of 20 ns accounts for uncertainties due to scattering and calibration. If still at least five L1-hits fulfil this last causality criterion, the event passes the trigger selection and is stored for further analysis.

3.2.4 Calibration

The quality of high level physics analyses is limited by the quality of the event reconstruction. To minimise uncertainties on the reconstructed parameters it is essential that the status of the detector is well understood at any given time. The position of the OMs has to be known at the order of 10 cm and the timing has to be reliable down to the nanosecond.

Position Calibration

The detector lines are flexible and pulled up straight by a buoy. They are thus subject to drag from the deep sea current and move around in the water. To track the shape of each line a High Frequency Long Base Line (HFLBL) acoustic system is in use. Every fifth storey is equipped with a hydrophone picking up the acoustic signals from emitters at the anchor of each string. The position of each of the hydrophones is then obtained by triangulation. These positions are subsequently fitted with a polynomial to obtain the shape of the whole string. With this, the positions of the OMs can be determined with a precision of 10 cm [48]. For the orientation of the OMs, compasses and tiltmeters are used and produce an accuracy of a few degrees.

Time Calibration

An LED on each OM right at the photocathode area is used to measure the transit time it takes for an electron that is released from the cathode to reach the readout electronics at the end of the PMT where the signal is recorded and supplied with a time stamp according to the internal ARS clock. These local clocks on the LCMs are synchronised with the master clock at the shore station. Additional LED beacons on storeys 2, 9, 15, 21 of each line and laser beacons at the bottoms of line 7 and 8 are used for intra and inter storey time calibration. With these systems, a timing accuracy of below 1 ns has been achieved [49].

Charge Calibration

The reconstruction of muon tracks depends mostly on the time and position of the hits. Shower events, on the other hand, are usually approximated as point sources with an isotropic time emission spectrum. Shower reconstruction algorithms make heavy use of the number of photons arriving on a PMT and depend on precise values for this quantity. The front end electronics that reads out the PMT signal also converts the voltage pulse caused by the electrons into a measurement of the number of photons that hit the cathode area. This measurement needs to be properly calibrated as well. This charge calibration is done on separate *minimum bias* runs where the PMT signal is digitized at random times. With these random readouts, the pedestal – the electric signal the PMT puts out when no photons hit the photocathode – and the single electron peak can be sampled. With this information, the transformation from measured voltage to number of photo-electrons can

be determined. The readout electronics saturates at about 20 PE, so that for higher charges no further differentiation is possible.

3.2.5 Background

Only a tiny fraction of the hits recorded by the OMs originates from secondary particles created by neutrino interactions. The vast majority is caused by various background sources. A proper understanding of these sources is important in order to distinguish the signals events from them.

Optical Background

The ANTARES detector has been built at depth of 2500 m which blocks out all daylight. However, it is not completely dark in these depths. Microscopic life forms (mostly bacteria) communicate by creating their own light. This effect is called *bioluminescense* and is one of the main contributors to the count rate of the PMTs. Bioluminescense occurs localised in short bursts of a few seconds and can cause count rates of several megahertz. The bioluminescense rates increase significantly during spring time and slowly fade towards the end of the year. A correlation with the velocity of the local sea current has been observed as well.
At the ANTARES site, the seawater contains potassium at a concentration of about 416 ppm. Of this, $0.0118\,\%$ is the radioactive isotope ^{40}K with a half-life time of $t_{1/2} = 1.28 \times 10^9$ years. About $90\,\%$ of the times, ^{40}K decays into ^{40}Ca while emitting a relativistic electron with an energy up to 1.33 MeV. These electrons can induce up to 150 Cherenkov photons and pose a continuous, ubiquitous background of around 40 kHz. An inherent dark noise contributes an additional 3 kHz to the rate of each PMT. Figure 3.9 shows the rate over time for two reference OMs during data taking.

Atmospheric Sources

Earth's atmosphere gets constantly bombarded by cosmic rays. In the decay chain of those hadronic interactions, muons and electron- and muon-neutrinos can be found. Due to their production site, they are also called *atmospheric muons* and *atmospheric neutrinos*. Because of relativistic effects, atmospheric muons can travel several kilometres before they decay; they can reach the depths of the sea and leave a signal in the detector. Light from atmospheric muons constitute one of the major backgrounds for a Cherenkov neutrino telescope like ANTARES. These muons cannot, however, traverse the whole diameter of earth. Only considering events that are identified as

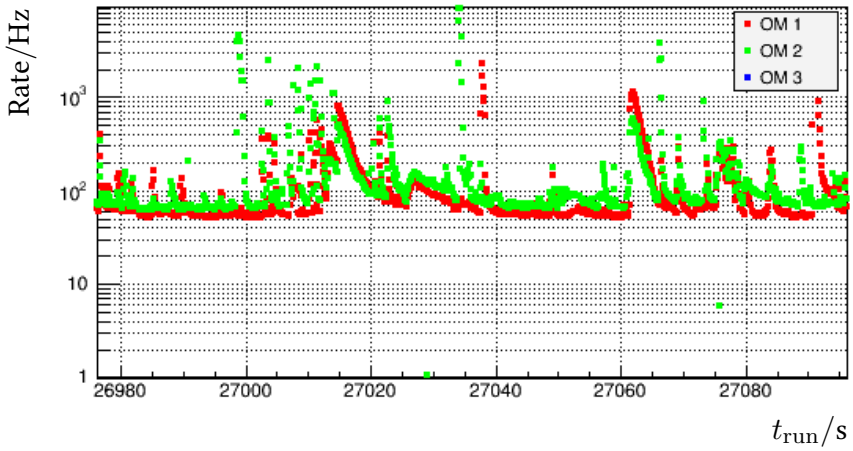

Figure 3.9: Online rate of two PMTs during a short period of one run. Visible is the baseline around 50 kHz and frequent bursts up to several megahertz.

up-going is an effective means to reject these atmospheric muons. Neutrinos, on the other hand, can freely propagate through earth's rock and pose an almost irreducible background to the cosmic signal. Only their energy spectrum is slightly softer than the expected E^{-2} spectrum from cosmic sources. See for example figure 3.10 for the energy dependence of the number of triggered events from atmospheric and cosmogenic neutrinos.

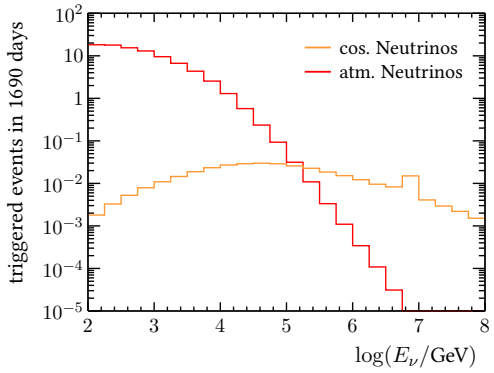

Figure 3.10: Monte Carlo predicted number of triggered events in the ANTARES detector in the data period covered by this work (see chapter 6) caused by atmospheric neutrinos (red) and cosmogenic neutrinos with an assumed flux of $E^2 d\Phi_\nu/dE = 10^{-8}\,\mathrm{GeV\,cm^{-2}\,s^{-1}}$ (orange).

3.2.6 Visibility

Since down-going events are generally rejected because of an overwhelming background rate of atmospheric muons, the OMs are mounted on their LCMs facing downward at 45° from the LCM axis. This increases the sensitivity to the Cherenkov light of up-going particles which is emitted at $\vartheta_c \approx 42^\circ$: Neutrino telescopes usually "look downwards" and utilise the Earth as a shield against atmospheric muons. This considerably reduces the field of view to the part of the sky below the local horizon. A neutrino telescope on the poles like IceCube always sees the same hemisphere. Because of the latitude of ANTARES, the detector's field of view gets constantly rotated around, allowing for the survey of a larger fraction of the full sky. The fraction f of time a stellar object at declination δ is in the field of view of a purely downwards looking experiment at latitude ϕ can be described by [50]

$$f = 1 - \frac{\operatorname{acos}^*(-\tan(\delta) \cdot \tan(\phi))}{\pi}, \tag{3.5}$$

with $\operatorname{acos}^*(x)$ as a continuation of the usual $\operatorname{acos}(x)$: For arguments beyond $|x| > 1$ this function computes to $\operatorname{acos}(x)$ at $x = 1$ or $x = -1$, respectively. The visibility of a few selected sources depending on the detector latitude and the visibility of ANTARES at $\phi = 42.8^\circ$ depending on the source declination are shown in figure 3.11. The galactic centre region around $\delta = -29^\circ$, for example, is visible to ANTARES $67\,\%$ of the time but never in the field of view of a detector at the South Pole like IceCube[1].

3.3 Simulation

No modern high energy physics experiment can work without a proper simulation. The distributions of observable quantities can be compared to ensure a proper understanding of the fundamental processes from first interactions to the behaviour of the hardware. Particle reconstruction algorithms are developed on simulated events and their quality assessed by comparing reconstructed quantities to the simulated ones, e.g. the direction of a muon created in a neutrino interaction. Simulations in particle physics are often referred to as *Monte Carlo* according to the underlying methods used in the generation. In ANTARES, the simulation of events is done in three distinct steps: event generation, photon tracking and detector response.

[1] As shown in section 2.3.2, the IceCube experiment can provide visibility by using high-energy starting events.

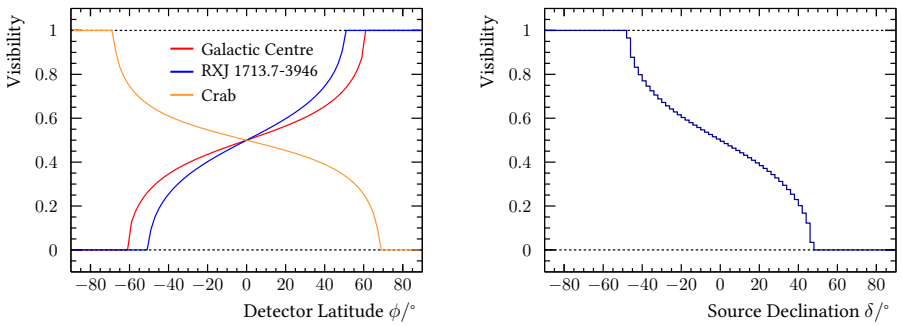

Figure 3.11: Visibility **Left:** of different sources depending on the detector latitude and **Right:** for the ANTARES detector at $\phi = 42.8^\circ$ depending on the source declination. The visibility is the fraction of the time the source spends in the experiments field of view below the local horizon.

3.3.1 Event Generation

An event generator defines a sufficiently large volume in which the detector is still sensitive to potentially emitted Cherenkov light. This volume is called the *can*. For an event generated outside the can, electrically charged particles will be tracked and propagated to the edge of the can in case they cross its boundary. No Cherenkov light is generated; only energy losses are taken into account. For neutrino interactions, this is done by the GENHEN package [51], for atmospheric muons by the MUPAGE package [52,53]. The neutrino directions are generated isotropically while the energy spectrum follows a $E^{-1.4}$ power law. This ensures sufficient statistics at higher energies. The neutrinos are generated within an energy range of $10^2 \leq E_\nu/\text{GeV} \leq 10^8$. Atmospheric muons are simulated with the observed energy spectrum but due to their high flux, the generated statistics has been reduced by a factor of 3. To include the simulated samples in high-level analyses, they have to be rescaled by an event-by-event weight. For atmospheric muons, this is simply done by weighting every event by a factor of 3, atmospheric neutrinos are scaled to follow the Bartol flux [54]. For astrophysical neutrinos, traditionally a flux in the form of an E^{-2} spectrum is assumed but spectral indices other than 2 are considered as well. This means that the same set of simulated neutrino events can be used for the cosmic signal and the atmospheric background. The underlying physics is no different; only spectra have to be rescaled accordingly.

3.3.2 Photon Tracking

The charged particles that reached the can boundaries (or were generated already inside) are picked up by the program *km3* which keeps track of the particles' energy losses and the photons they would generate through various processes. The km3 tool then determines the number of photons that reach every PMT. It would be computationally too expensive to track every single photon generated in every event. Instead, km3 works with tabulated PDFs to determine the photon-intensity on the PMTs. These tables have been filled in advance by fully simulating a number of events with GEANT [55]. Every time a photon crosses one of several predefined spheres around the photon's point of emission, its position, direction and time are recorded. These photon distributions are later convoluted with various PMT orientations – the PMTs have a detection efficiency which depends on the photon incident angle – to estimate the number of photoelectrons on such a PMT.

3.3.3 Detector Response

The detector response to the photons provided by km3 is simulated by the TriggerEfficiency tool [56]. The photons are collected over the integration time of the ARS and combined in a single hit. Random, uncorrelated background hits from bioluminescense and ^{40}K are added as well. The mean rates for these backgrounds is taken directly from data, so that the noise level of every Monte Carlo set matches its corresponding data run. The time between the first photon hit and the detection and time-stamping of the electronic signal is taken into account as much as its uncertainty, the TTS. The uncertainty on the transit time is lower when more photons hit the photocathode. This is taken into account by smearing the measured transit time with a Gaussian with a standard deviation that incorporates the determined TTS of the single photoelectron peak (typically around 1.3 ns):

$$\sigma = \frac{1.3\,\mathrm{ns}}{\sqrt{N_{\mathrm{PE}}}}, \tag{3.6}$$

where N_{PE} is the number of photoelectrons in the integration window. Two ARS for every PMT and the ARS dead time of 250 ns are considered as well. The uncertainty on the charge reconstruction is simulated by smearing the number of arriving photons with a Gaussian with width $\sigma = 0.3\,\mathrm{PE}$. After this stage, the simulation is technical equivalent (in terms of data format) to recorded data and the same trigger and reconstruction algorithms can be applied.

3.4 Muon Track Reconstruction

Atmospheric neutrinos are expected to be isotropically distributed over the whole sky while neutrinos from a cosmic source cluster around the source location. A reliable reconstruction of the neutrino's direction of origin is essential to identify these astrophysical objects above the atmospheric background. A muon's track can be described by its position $\vec{p} = (p_\mathrm{x}, p_\mathrm{y}, p_\mathrm{z})$ at an arbitrary time t_0 and the direction of its momentum vector $\vec{d} = (d_\mathrm{x}, d_\mathrm{y}, d_\mathrm{z})$. Since its normalisation is of no importance, the latter can be parametrised by two angles ϕ and ϑ as $\vec{d} = (\sin\vartheta\cos\phi, \sin\vartheta\sin\phi, \cos\vartheta)$. Therefore, there are 5 independent parameters that fully describe a muon track and need to be determined by a reconstruction. One of the most used muon reconstruction algorithms in ANTARES has been dubbed *AAFit*. It was developed and is described in greater detail in [57]. AAFit reconstructs muon tracks in four distinct steps. The last step reaches a median angular resolution of less than half a degree but is also the most sensitive to the a required a priori estimate of the track parameters. A so-called *prefit* of sufficient quality is necessary for this last step to reach its optimal reconstruction performance. The objective of the earlier steps is to provide this prefit to the final reconstruction step.

linear Prefit

This first step does not need a first guess on the track parameters and its output can be used as a very first estimate of the track parameters needed by the following steps. The linear prefit works on a subset of hits of local coincidences (two L0-hits within 25 ns on the same storey) and hits with a measured charge of at least 3 PE. It simplifies the relation between the muon tracks and the hits by assuming that all hits lie directly on the track itself. In this case, equation (3.3) can be rewritten as:

$$\vec{y} = \boldsymbol{H}\vec{\Theta}. \tag{3.7}$$

with $\vec{y} = (x_1, y, \ldots, z_n)$ as a vector containing the positions of all selected hits, $\Theta = (p_x, d_x, \ldots, d_z)^\mathrm{T}$ as the vector containing the track parameters and n as the number of selected hits. These two vectors are linearly connected

using matrix $\boldsymbol{H}$ containing the hit times:

$$\boldsymbol{H} = \begin{pmatrix} 1 & ct_1 & 0 & 0 & 0 & 0 \\ 0 & 0 & 1 & ct_1 & 0 & 0 \\ 0 & 0 & 0 & 0 & 1 & ct_1 \\ 1 & ct_2 & 0 & 0 & 0 & 0 \\ 0 & 0 & 1 & ct_2 & 0 & 0 \\ \vdots & \vdots & \vdots & \vdots & \vdots & \vdots \\ 0 & 0 & 0 & 0 & 1 & ct_n \end{pmatrix}. \tag{3.8}$$

The estimates on the track parameters $\vec{\Theta}$ are obtained by minimising χ^2, defined as:

$$\chi^2 = \left(\vec{y} - \boldsymbol{H}\vec{\Theta}\right)^{\mathrm{T}} \boldsymbol{V}^{-1} \left(\vec{y} - \boldsymbol{H}\vec{\Theta}\right). \tag{3.9}$$

Here, $\boldsymbol{V}$ is the covariance matrix storing the uncertainties on the hit positions. Uncertainties on the hit times are neglected. The track parameters that minimise equation (3.9) can be determined analytically with:

$$\vec{\Theta} = \left(\boldsymbol{H}^{\mathrm{T}}\boldsymbol{V}^{-1}\boldsymbol{H}\right)^{-1} \boldsymbol{H}^{\mathrm{T}}\boldsymbol{V}^{-1}\vec{y}. \tag{3.10}$$

M-Estimator

The next step performs a new hit selection by selecting all hits that are closer than 100 m to the track given by the linear prefit and whose time residuals are within a ± 150 ns time window. Hits with an amplitude above 2.3 PE are selected as well. The time residual t_{res} is defined as the difference between the expected time given by equation (3.3) and the actually measured time. A quality parameter similar to the χ^2 is the M-estimator:

$$M_{\mathrm{Est}} = \sum_i 2 \cdot \sqrt{1 + \frac{t_{\mathrm{res}}^2}{2}} - 2. \tag{3.11}$$

For small errors, the M-estimator behaves quadratically like the χ^2 test; but for bigger values it becomes linear. The M-estimator is therefore more robust against outliers which is useful for data samples that contain background. The minimum of M_{Est} gets determined through numerical methods while using the parameters of the prefit as starting values. Note that the factor 2 at the beginning and the -2 term at the end are irrelevant for the minimisation and often ignored in the implementation of the method.

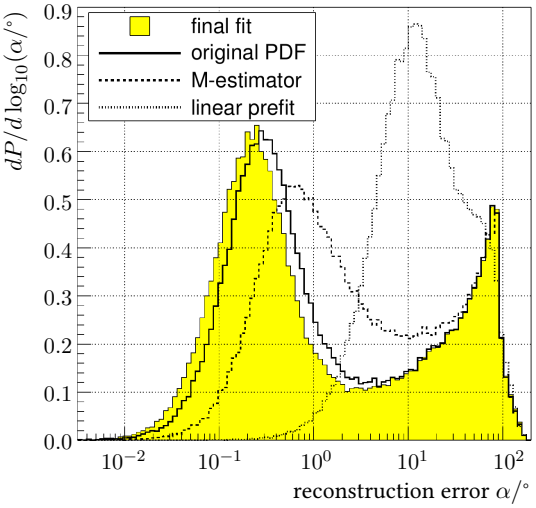

Figure 3.12: Distribution of the angular separation between the simulated muon's direction and the reconstructed direction after each step in the reconstruction procedure of AAFit.
Figure taken from [57].

simple Likelihood

After the M-estimator fit, a maximum likelihood fit is performed (see section 7.1 for a description of likelihood estimates). A new hit selection picks all hits with a measured charge above 2.5 PE or a time residual within $[-R/2, R]$, with R being the root-mean-square of the hit time residuals of all hits selected in the previous fit. The likelihood uses a parametrisation of the time-residual distribution of signal hits. The starting value of the likelihood fit is the result of the preceding M-estimator fit.
The M-estimator and subsequent likelihood fit are repeated an additional nine times from various pre-defined starting directions to ensure that the global and not some local maximum has been found.

full Likelihood

After the repeated execution of the M-estimator and simple likelihood fits, the result with the best likelihood is used as the starting track for the final full likelihood. This step includes an improved likelihood that takes the measured hit charge into account as well as contributions from background sources. All hits in a broad time residual window of $[-250\,\text{ns}, 250\,\text{ns}]$ are included. A contamination with background hits is no big problem since it is accounted for in the likelihood itself. The distribution of the angular separation between the reconstructed and simulated muon direction after each of the fit steps can be seen in figure 3.12. The final fit reaches a median angular resolution of about 0.4°.

With the likelihood value of the best fit, a quality parameter can be constructed:

$$\Lambda = \frac{\log(\mathscr{L}_{\max})}{N_{\text{hits}} - 5} + (N_{\text{comp}} - 1)/10, \tag{3.12}$$

where $\mathscr{L}_{\max}$ is the maximum likelihood that was obtained in the fit, N_{hits} the number of hits used in the fit and N_{comp} as the number of trials of the repeated execution of steps two and three that produced compatible results. The factor $1/10$ was chosen to maximise the separation between signal and atmospheric muons. Cutting on this parameter (usually around $\Lambda > -5.2$) gives a powerful handle of rejecting badly reconstructed events.
The implementation of the algorithm also provides a covariance matrix for the fitted parameters. From this matrix, error estimates for the two fitted angles ϕ_{tr} and ϑ_{tr} can be extracted as σ_ϕ and σ_ϑ. The two error estimates for the separate angles can be combined to a total angular error estimate:

$$\beta_{\text{tr}} = \sqrt{(\sigma_\phi \cdot \sin(\vartheta_{\text{tr}}))^2 + \sigma_\vartheta^2}. \tag{3.13}$$

Pull distributions for the two angles – defined as the ratio of the actual errors and the error estimates – are shown for an E^{-2} spectrum in figure 3.13. The standard deviations of the Gauss fits are slightly bigger than 1: The error estimate underestimates the actual error on the reconstructed angle.

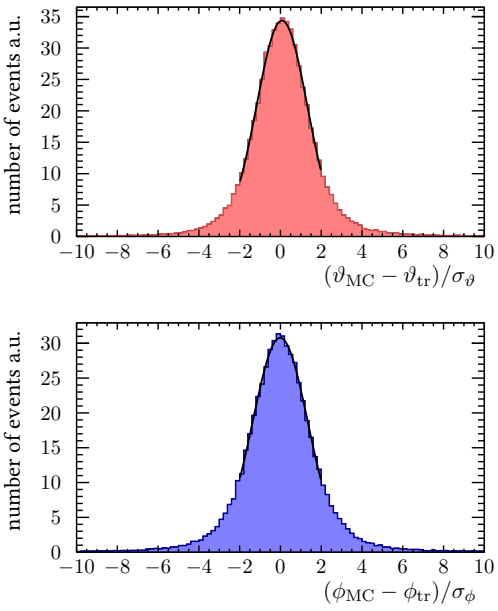

Figure 3.13: Pull distributions for the reconstructed angles after the final "full likelihood" step of the AAFit algorithm. **Top:** zenith angle and **Bottom:** azimuth. Quality cuts of $\Lambda_{\text{tr}} > -5.2$ and $\beta_{\text{tr}} < 1^\circ$ have been applied. The Gauss fits have a standard deviation of 1.24 for the zenith angle pull and 1.36 for the azimuth pull.

Conclusion

The ANTARES detector is located in the deep Mediterranean Sea and consists of 885 optical modules, on 12 vertical strings, mustering an instrumented volume of about $0.01\,\mathrm{km}^3$. This device is well equipped to detect the faint light produced by charged particles that are created in neutrino interactions. An extensive "run-by-run" simulation effort is carried out where for each run a corresponding Monte Carlo set is simulated taking the run's actual hardware and environmental conditions into account. Several detector signatures are possible: Muons propagating on long, straight tracks and inducing Cherenkov light under a characteristic angle of $\vartheta_\mathrm{c} \approx 42^\circ$ along their way; electromagnetic or hadronic showers quickly depositing their complete energy and sending off one burst of light. Double-shower or shower+track signatures are possible in events where a tau emerges from the neutrino interaction. Each of these signatures have to be properly reconstructed to estimate the properties of the parent neutrino. Dedicated reconstruction algorithms have been developed to achieve this task. An algorithm to reconstruct muon tracks has been presented. This reconstruction algorithm achieves a median angular resolution of below half a degree. For this PhD project, a separate shower reconstruction algorithm was developed which will be presented in one of the following chapters.

Chapter 4

Outlook on KM3NeT

"Look, if we build this large, wooden badger..."
Sir Bedevere – Monty Python and the Holy Grail

This chapter gives a short introduction to the ANTARES successor: the KM3NeT detector [59, 60]. Subsequently, it will focus on my work on the first prototype digital optical module (DOM) housing 31 small PMTs. Most of the results presented in this chapter have already been published in [61].

4.1 The KM3NeT Neutrino Observatory

KM3NeT (**km^3 Ne**utrino **T**elescope) is a distributed neutrino observatory that is currently being built in the Mediterranean Sea. It will be constructed in building blocks of 115 strings with 18 DOMs each. To cover a wide range of physics topics, KM3NeT will be realised in two configurations as the ORCA and ARCA detectors.
ORCA (**O**scillation **R**esearch with **C**osmics in the **A**byss) will have a small, densely instrumented detector layout and is to be deployed about 10 km east of the ANTARES site off the coast of France (KM3NeT-Fr). With 20 m horizontal inter-string spacing and a vertical DOM spacing of 9 m, it will focus on low energy neutrino interactions and investigate neutrino oscillations. Its main goals will be the determination of the neutrino mass hierarchy and the measurements of one of the neutrino mixing angles, ϑ_{23}.
ARCA (**A**stroparticle **R**esearch with **C**osmics in the **A**byss) constitutes the high energy configuration. With a line-to-line spacing of around 90 m and an inter-DOM distance of 36 m, it will concentrate on the detection of a cosmic neutrino flux – whether point-like, extended or diffuse. In its final stage, it will encompass a volume of several cubic kilometres. ARCA will be built about 100 km off the coast of Portopalo di Capo Passero on Sicily, Italy at a depth of 3500 m (KM3NeT-It).

A key feature common to both the ORCA and ARCA configuration is the novel multi-PMT optical module. It houses 31 3-inch PMTs in a pressure-resistant glass sphere 432 mm in diameter. The left picture of figure 4.1 shows an assembled DOM with this new layout: The PMTs are arranged in five horizontal rings of 6 PMTs each at zenith angles of 56°, 72°, 107°, 123° and 148°. Neighbouring PMTs within a ring are separated by 60°, consecutive rings staggered by 30°. The final PMT is installed in the centre of the lowermost ring facing straight down. Every PMT is surrounded by a reflector ring increasing its effective photon-collecting area [62]. Each PMT is read out by its own low-power-high-voltage base with an adjustable threshold for the signal discrimination [63]. The time-stamp of the detected signal pulses together with its *time over threshold* (ToT) is sent in digital form to shore via an optical interface [64, 65].
Compared to traditional optical modules with a single large PMT [46, 66, 67], this multi-PMT design has a three to four times larger photocathode area that covers almost the full solid angle with a uniform acceptance. Beyond that, the segmentation of the photocathode allows for efficient suppression of ambient background and provides photon counting capability in a broad dynamic range and coarse direction information for single photons.

4.2 The Pre-Production Model Digital Optical Module (PPM-DOM)

A first prototype realising this multi-PMT design was deployed within the ANTARES observatory on the 16th of April 2013. It was installed as an autonomous detector on the ANTARES Instrumentation Line (IL). The IL provided the interface for the DOM's power supply and data connection to the shore station. Located at a depth of 2375 m and about 100 m above the sea bed, it collected data for almost a year. The right picture of figure 4.1 shows the PPM-DOM mounted on an ANTARES LCM just before its deployment.

4.2.1 First Deep-Sea Runs

The first data taken in the deep-sea were used to calibrate the high voltage and time stamps of the individual PMTs. A part of the early runs were taken in conjunction with ANTARES laser calibration runs [49, 68]. The ANTARES detector is equipped with green lasers ($\lambda = 532$ nm) mounted on a number of anchors at the bottom of the strings. These lasers produce pulses with lengths of less than 1 ns and enough light to illuminate almost the whole de-

Figure 4.1: Left: A KM3NeT DOM with 31 small PMTs after assembly in the Nikhef workshop. The PMTs are arranged in horizontal rings of various zenith angles. Neighbouring PMTs within a ring are separated by 60°, consecutive rings staggered by 30°. **Right:** The PPM-DOM during deployment. It is connected on the first storey of the ANTARES Instrumentation Line. The metal structure is a standard ANTARES LCM which provides the DOM with power and data read-out.

tector and are used for inter-string time calibrations. Figure 4.2 shows on the left-hand side the ToT of a typical PMT during such a laser run where the flashing laser was located at the bottom of a neighbouring string (DOM-laser-distance about 125 m). The left, high peak is caused by the detection of single photons. The high voltage of the individual PMTs was adjusted so that this single-photon peak is situated at about 30 ns. The second peak at larger ToT around 250 ns can be attributed to the light from the ANTARES calibration laser. The right-hand side of the figure shows the time difference between consecutive hits on the same PMT. The slope has been fitted with an exponential $f(t) = A \cdot e^{-t/\tau}$ with $\tau = 1.05 \times 10^{-4}$ s (red line in the plot). This corresponds to a pure background rate of 9.5 kHz. On top of the exponential slope of the pure background, a peak at values close to zero is visible. This peak is caused by afterpulses which have a 5 % chance to occur about 3 µs after a signal hit has been detected. Due to its low operation-frequency of 1 kHz, the signal from the laser does not show up in this plot.

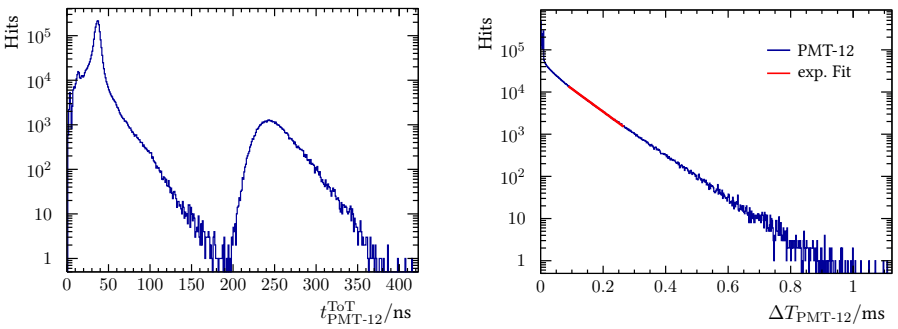

Figure 4.2: Left: ToT distribution of a typical PMT during an ANTARES laser calibration run. Visible are the sharp single-photon peak at around 30 ns and broader peak at higher ToT caused by the calibration laser. **Right:** Time difference between consecutive hits on the same PMT. An exponential fit with a characteristic time $\tau = 1.05 \times 10^{-4}$ s is indicated by the red line.

PMT Coincidences

The large number of PMTs in one single DOM, allows for a study of the correlations between hits in different PMTs. For this, the *coincidence level* (CL) is defined as the number of PMTs that detected a signal within a time window of 20 ns. The red histogram in figure 4.3 shows the single-photon rate averaged over the duration of a time frame of 2^{27} ns $\approx$ 134 ms. The length of a frame is based on the data format that reserves 27 bits for the time information of each hit. The base line of the count rate is stable at an average 8 kHz per PMT. Frequent increases of the hit-rate to up to 20 MHz – which can be attributed to bioluminescence bursts – are visible. The figure also shows the rate at which two or three PMTs are hit within a time window of 20 ns: the two- and threefold coincidence rate. Because of the low statistics, the threefold coincidence rates have been averaged over three time frame bins. The histogram for the twofold coincidence rate shows peaks in the same time frames as the singles rate: An increased background rate in one PMT also increases the rate of incidental twofold coincidences containing this PMT. The threefold coincidence rate shows increases only for the highest bioluminescence bursts. This shows that the combinatorial background contributes much less to the rate of three- (and higher-) fold coincidences. These rates are dominated by genuinely correlated photons emitted by the same ^{40}K decay.
This is also evident from figure 4.4. The black dots show the full singles and two- to fourfold coincidence rates averaged over each run taken from early July to late December of 2013. To determine the coincidence rates from ran-

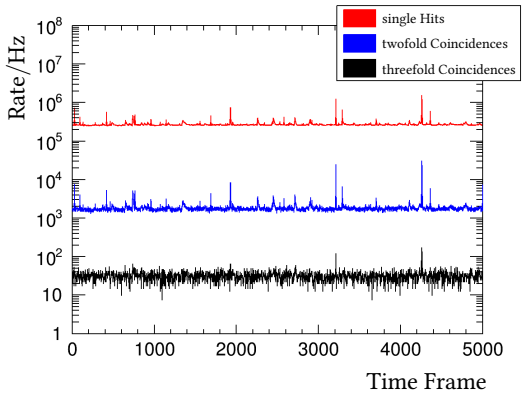

Figure 4.3: Rates during a typical run averaged over the frame time of approximately 134 ms. The rate of single-photon hits is shown in red, the rate of two- and threefold coincidences is plotted in blue and black, respectively.

dom background, the correlation between the hits of a genuine ^{40}K coincidence has to be broken. To do so, the time for all hits on each PMT has been shifted by 100 ns multiplied by the internal PMT-channel ID. The resulting coincidence rates correspond to the contributions of a purely random background. The red triangles show the difference between the full and the time-shifted coincidence rates and can be attributed to the genuine coincidences from ^{40}K decays. The rates presented by the black data points show a decreasing trend towards higher run number which can be explained by a decreasing activity of luminescent organisms from summer to winter. For some runs, large increases in rate – up to 1.2 MHz of single hits rate for the full DOM – are visible in all coincidence levels. The ^{40}K rate on the other hand is completely stable over the year at 340 Hz, 30 Hz and 2.7 Hz for two-, three- and fourfold coincidences, respectively. The combinatorial background contributes only very little to the fourfold coincidence rates.

Angular Dependence of the Coincidence Rate

Figure 4.5 shows the distribution of the hit-time differences, $\Delta T_{ij} = T_i - T_j$, between a number of selected PMT pairs. The angular separation of the PMTs constituting the pairs are (in reading order) 33°, 65°, 120° and 165°. All distributions show a more or less pronounced peak around 0 ns on top of a flat baseline. From these plots the reason for the length chosen for the coincidence window of 20 ns gets evident as it corresponds to the base-width of the peaks in the ΔT distributions. For every distribution, a Gauss-plus-constant fit is shown as a red line. The Gaussian contribution to the count rate decreases with increasing angular separation of the PMTs and can be attributed to photons from the same ^{40}K decay (see section 3.2.5). Usually, the transit times of

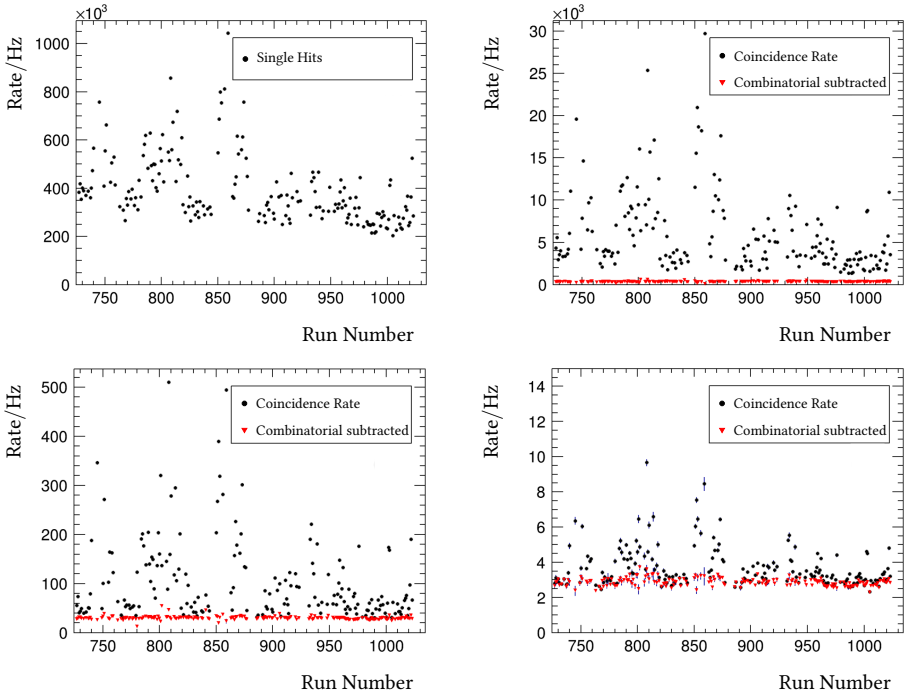

Figure 4.4: Development of the coincidence rates as a function of the run number for (in reading order) single hits, two-, three- and fourfold coincidences shown as black dots. The red triangles show the rate with the combinatorial background subtracted and can be attributed to the genuine ^{40}K coincidence rate.

different PMTs vary by a few nanoseconds. The presented ΔT_{ij} histograms are excellent candidates to calibrate the time-stamping of the hits. Before the calibration, the mean positions of the different Gaussian peaks are distributed around 0 ns. The recorded hit times of all PMTs can be individually offset so that the means of all Gaussian peaks simultaneously shift to 0 ns. The plots in figure 4.5 show the already calibrated timing.

The coincidence rates of all individual PMT pairs in the DOM are shown in figure 4.6. Those rates are depicted as red data points and include *combinatorial background* from uncorrelated single hits on two PMTs. To remove this background and only show the ^{40}K coincidence rates, the baseline from the fits shown in figure 4.5 have been subtracted. The result can be seen in the blue data points in figure 4.6. This figure shows that the twofold coincidence rates of pairs of PMTs that are separated by more than about 90° are

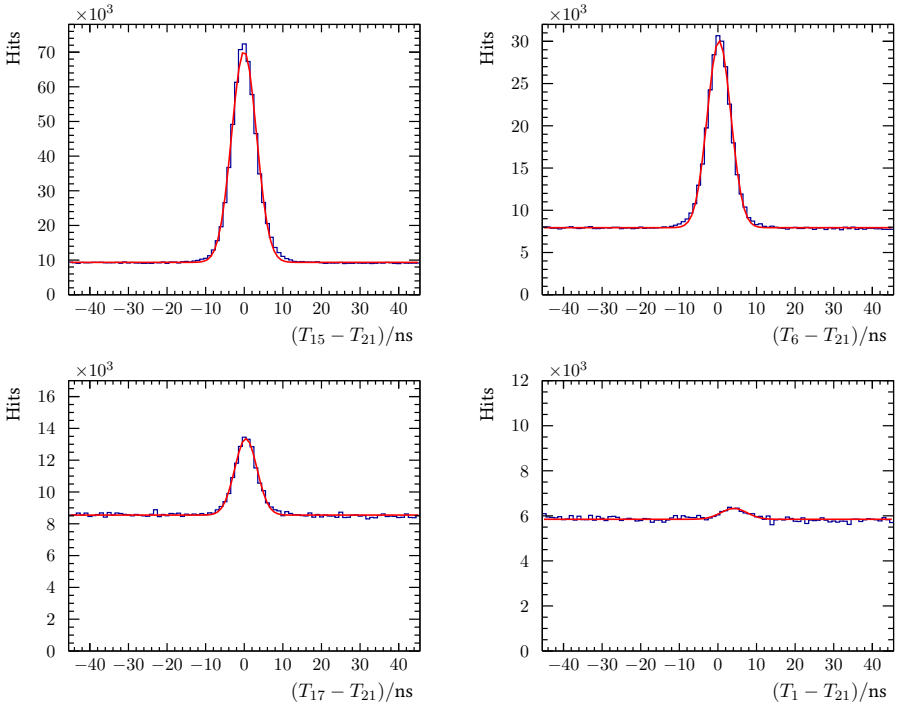

Figure 4.5: Distribution of the hit time differences between various PMT pairs. The angular separation of the PMTs constituting the pairs are (in reading order) 33°, 65°, 120° and 165°. The red lines are fits of a Gaussian normal distribution on top of a flat baseline.

completely dominated by combinatorial background. This should to be taken into account if one wants develop a trigger algorithm based on the number of PMTs hit on a single DOM.

Angular Dependence of Rate Bursts

The bursts in the count rate – dubbed as *spikes* – are not uniformly distributed over all PMTs but have a preferred direction. Here, a spike is considered when a PMT's count rate is more than 5 % higher than its average throughout a run. When consecutive time frames exceed this rate threshold, the subsequent frames are considered a continuation of a single spike. As can be seen in figure 4.7, there is a clear asymmetry in spike counts towards upwards-looking PMTs around $\varphi \approx 0°$. Those PMTs face the ANTARES LCM on

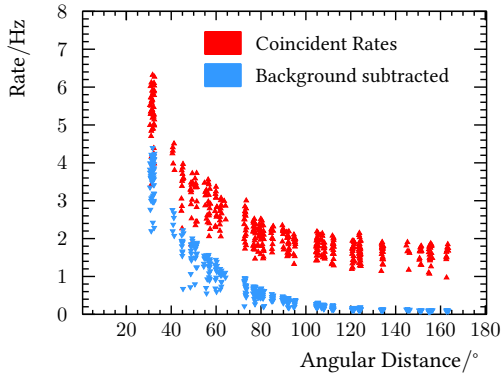

Figure 4.6: Coincident rate of all individual PMT pairs as a function of the angular distance of the PMTs. Red triangles consider all coincidences; for the blue triangles, the contribution of the combinatorial background has been subtracted.

which the DOM is mounted. The metal support structure causes turbulences in the wake of the underwater sea current. A possible explanation is that in such turbulences, micro-organisms increase their bioluminescence activity and emit more light which is more likely to get picked up by the PMTs facing the LCM causing the observed asymmetry. In the final KM3NeT string design, the DOMs will be suspended between two, 4 mm Dyneema ropes without any additional metal structure. Thus, such a shadowing will not occur in the final detector.
To not distort the distribution of rates as a function of the coincidence level presented in the following section, a somewhat rigorous high rate veto is applied: As soon as a single PMT is declared as spiking, the complete time frame gets rejected. For a future apparatus, of course, more elaborated veto techniques can be implemented, e.g. just masking the spiking PMT instead of dropping the whole DOM.

4.2.2 Atmospheric Muons

The segmentation of the photocathode area allows for photon counting in a high dynamic range. The number of photons arriving on the DOM in quick succession can be used as a simple event type estimator. While bioluminescent organisms can emit a large number of photons, they usually do so over many milliseconds causing an increased rate of single, isolated hits. The photons from the electrons produced in ^{40}K decays on the other hand arrive on the DOM in a time window of a few ten nanoseconds. High energy muons can induce so much time-correlated light at once that – also through scattering – as much as every PMT can be hit by photons almost simultaneously. Figure 4.8 compares in the left-hand plot the event rates for the different coincidence levels in the recorded data with Monte Carlo simulations. With

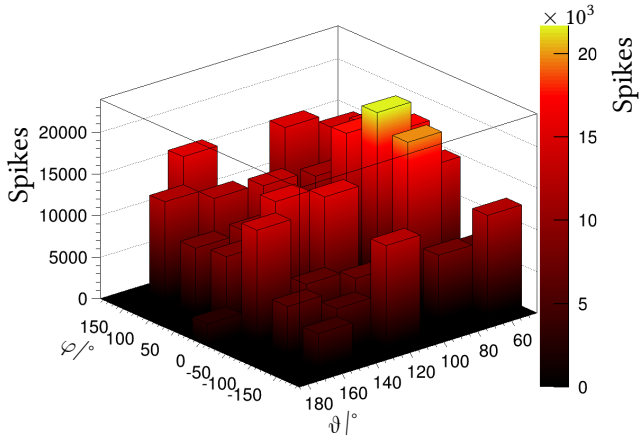

Figure 4.7: The number of distinguished spikes in the PMT's counting rates depending on the direction they are facing. The groups of constant zenith distance ϑ correspond to the horizontal PMT rings as described in section 4.1. The PMT with $\vartheta = 180°$ faces straight down, PMTs with azimuth $\varphi \approx 0°$ point towards the metal support structure the DOM is mounted on.

exception of the first bin, the Monte Carlo shows excellent agreement with the data. Comparing the data to the Monte Carlo simulations reveals several noteworthy features:

Bioluminescence The discrepancy in the singles rate can be explained by bioluminescence which was not simulated due to its strong seasonal variation. As discussed earlier, these additional single photon give a contribution to higher coincidence levels through random combinatorics. This effect has been estimated analytically and is also shown (purple histogram).

Potassium-40 The singles and twofold coincidence rates are dominated by bioluminescence while the ^{40}K decays dominate until a coincidence level of about 6. The ^{40}K coincidence rates have been determined by simulations [69].

Atmospheric Muons Above a coincidence level of 8, virtually all events are caused by atmospheric muons. For the simulation of the atmospheric muons the MUPAGE tool [52, 53] has been used.

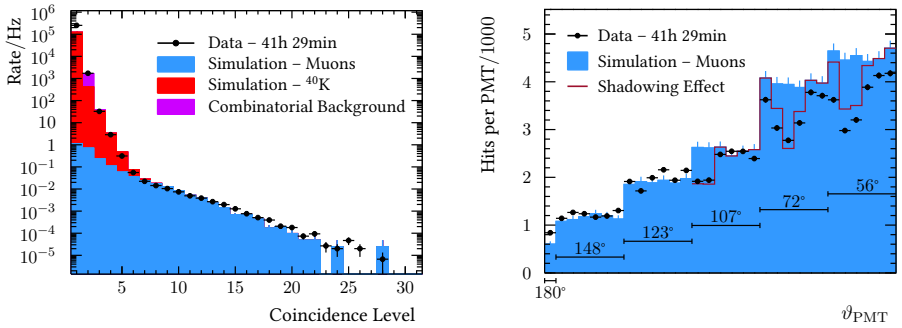

Figure 4.8: Left: The rate of events with various coincidence levels on a single DOM. The black points show the recorded data rate, the red histogram the rate from ^{40}K simulations and the blue histogram the rate from simulated, atmospheric muons. The purple histogram shows the expected rate from random coincidences by uncorrelated single hits. **Right:** The distribution of the number of hits on each PMT, considering only events with a coincidence level of at least 8. The PMTs are sorted according to their zenith distance. The left-most bin corresponds to the PMT looking straight down while the remaining bins are grouped analogue to the horizontal PMT rings of decreasing zenith angle.

The right plot of figure 4.8 shows the hit distribution over the PMTs of such a pure muon subset of events with a coincidence level of at least 8. The bins are arranged according to the zenith angle of their respective PMTs: The first bin shows the hit count of the central PMT looking straight down. The other bins are grouped by six and correspond to the different horizontal rings of PMTs in the DOM. The Monte Carlo predicts a uniform count rate for all PMTs within one ring (within statistical uncertainties) and higher counts for rings with smaller zenith angles: Atmospheric muons come from above and hit preferentially PMTs facing upwards. The data counts follow those predictions quite well with the exception of a number of points that fall significantly bellow the Monte Carlo. These bins correspond exactly to those PMT that face the ANTARES LCM on which the DOM is mounted. This mechanical support structure blocks the light from muons passing behind it. This shadowing effect was not included in the simulation but calculated by assuming all muons propagate exactly vertically and are uniformly distributed in the horizontal plane. This first order estimate describes the shadowing reasonably well and demonstrates – together with the ϑ-asymmetry in the hit count – the directional sensitivity of a single DOM.

Conclusion and Outlook

The first fully functional prototype of the new KM3NeT digital optical module with 31 small photomultiplier tubes has been tested in the deep Mediterranean Sea. It was implemented as a standalone detector on the Instrumentation Line of the ANTARES detector at a depth of about 2375 m and took data for almost one year from mid-April to the end of December of 2013. The baselines of the counting rates were stable at around 250 kHz for the full DOM or 8 kHz for an average PMT. Bursts of bioluminescence can increase the rates to up to 1.2 MHz for the full DOM. The KM3NeT-It site where the ARCA detector is to be built is about 1 km deeper than the ANTARES site and the bioluminescence activity is expected to be significantly reduced. The genuine coincidences from ^{40}K decays provide a straight-forward means for an intra-DOM timing calibration of the PMTs and demonstrate the overall nanosecond timing capability of the DOM.
The segmentation of the photocathode area allows the DOM to be sensitive to the arrival direction of detected photons. This has been shown by the ϑ-asymmetry in the number detected hits for high-CL events. It was further demonstrated in the increase in the singles rate – caused by bioluminescence – and the decrease in atmospheric muon events – caused by a shadowing effect – in the direction of the mechanical support structure on which the DOM is mounted. The suspension of the final KM3NeT string works without additional metal structures and will not cause such a shadowing effect.
The new multi-PMT design provides for a high performance optical module for future neutrino telescopes.

The Pre-Production Detection Unit (PPM-DU)

Following the in-situ tests of the new multi-PMT DOM, a prototype DU was deployed and tested at the KM3NeT-It site. The so-called PPM-DU (**P**re-**P**roduction **M**odel **D**etection **U**nit) consists of three additional multi-PMT DOMs separated by an inter-DOM spacing of about 36 m according to the ARCA string design. With this prototype, refined time-calibration and muon-identification methods have been developed. Instead of demanding at least 8 simultaneous hits on a single DOM, two-fold coincidences on three neighbouring DOMs can be used to select a pure sample of atmospheric muons [70]. Subsequently, those muons can be used to synchronise the timing between the different DOMs. With this single line, a zenith resolution of 7.6° has been achieved. The difference between simulated and reconstructed zenith angle and the event rate as a function of the zenith angle are shown in figure 4.9.

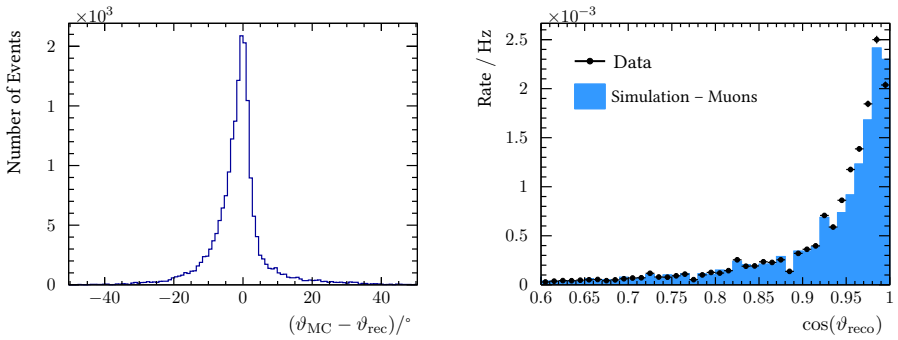

Figure 4.9: Left: The difference of simulated and reconstructed zenith angle for atmospheric muon events in the PPM-DU. **Right:** The event rate as a function of the reconstructed zenith angle for data (black dots) and Monte Carlo simulated events (blue histogram). Figures from [70].

The first full KM3NeT String

During the writing of this chapter, the first complete ARCA string was deployed on the third of December 2015 at the Italian site. The completely deployed and unfurled string was closely inspected by a remotely operated submarine and the first data was recorded the day after. After one hour of data-taking, the observation of the first atmospheric muons was reported. On the third of January 2016, the first neutrino candidate was announced [71]. Event displays for both candidates can be seen in figure 4.10.

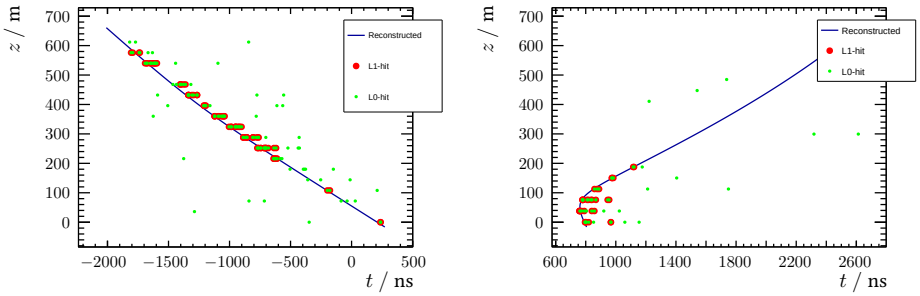

Figure 4.10: Event displays of the first deployed ARCA DU in z-t projection for **Left:** one of the first detected muon candidates and **Right:** the first reported neutrino candidate. Green dots are all hits recorded by any PMT, red dots are triggered hits used in the reconstruction and the blue line is the best fit assuming a muon track. Plots by [71]

Chapter 5

A Shower Reconstruction for ANTARES

Wer bin ich – und wenn ja, wie viele?
Richard David Precht

In the past, several attempts to develop algorithms for the reconstruction of particle showers in ANTARES have been made. So far, none of them satisfied the demands on the pointing accuracy made by point source searches. For the analysis presented in this thesis, a new shower reconstruction algorithm has been developed. As it was to be used in point source analyses, it is focused on directional accuracy and a resolution of a few degrees has been achieved. In the future, other analyses will benefit from including this shower channel as well.

5.1 Topology of underwater Particle Showers

When a neutrino induces an electromagnetic shower, the maximum intensity is not reached immediately. In fact, the number of emitted photons builds up to an energy-dependent maximum and falls off again as the shower propagates further. The shower's longitudinal intensity profile can be described by the following function [72]:

$$p(x) = x^{a-1} \frac{\mathrm{e}^{-x/b}}{b^a \Gamma(a)} \tag{5.1}$$

with:

x, the numeral of the longitudinal distance to the vertex in metres,
$a = 1.85 + 0.62 \cdot \log_{\mathrm{e}} (E/\mathrm{GeV})$ and
$b = 0.54$.

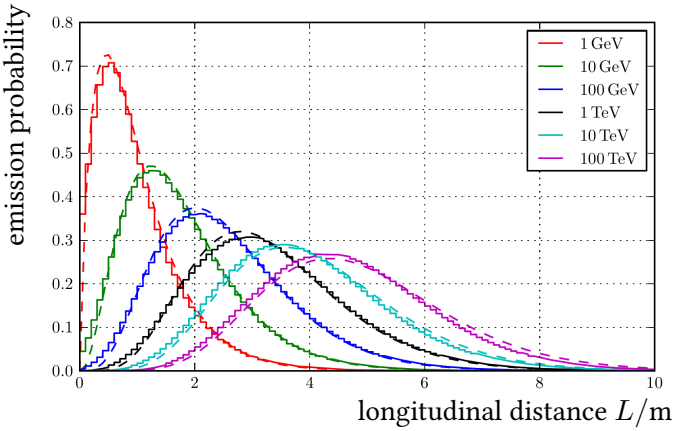

Figure 5.1: Longitudinal photon emission probability profile of electromagnetic showers in water for different shower energies. Here, L is the distance to the interaction vertex parallel to the neutrino direction. The solid histograms are filled from Monte Carlo simulations, the dashed curves are according to equation (5.1).
Figure taken from [72].

The shower's emission spectrum extends a few metres – as can be seen in figure 5.1. Compared to the distances of the various OMs in the detector, it can be approximated as a point source. Since not all charged particles created in the shower propagate in the same direction, photons no longer have to be emitted strictly under the Cherenkov angle of about 42° with respect to the neutrino direction. Instead, the emission spectrum is slightly smeared out with most of the photons still emitted under the Cherenkov angle. Figure 5.5 shows the angular dependence on the number of photons that are expected to arrive on a given PMT. This anisotropy in the number of emitted photons will be exploited in section 5.3 to reconstruct the direction of the shower and thereby in approximation of the parent neutrino. Photons γ_c that are emitted under the Cherenkov angle will arrive slightly earlier on a given PMT than photons that were emitted up- or downstream from γ_c and are hitting the same PMT (see figure 5.2). This effect is minuscule and has largely been ignored.

Naturally, an algorithm that assumes *one* common point of emission for all photons will most likely reconstruct a position along the shower axis and not the actual interaction vertex. For this reason, the reconstructed shower posi-

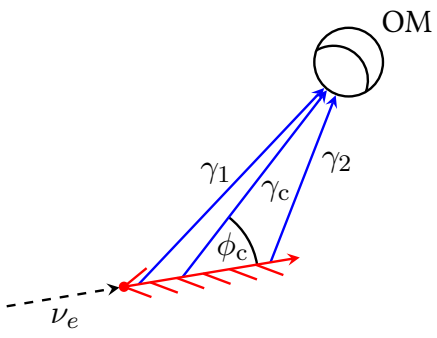

Figure 5.2: Schematic of different photons from the same shower arriving on the same optical module. A photon γ_c emitted under the Cherenkov angle with respect to the neutrino direction will arrive first at a PMT. Photons γ_1 and γ_2 that are emitted up- or downstream of γ_c will both arrive slightly later.

tion will be interpreted as the intensity weighted mean position determined from equation (5.1) and not the Monte Carlo vertex of the neutrino interaction.

5.2 Position Reconstruction

Not all hits in a time frame contain useful information about the neutrino interaction. In fact, most of the recorded hits are caused by various background sources. A proper hit selection can help to filter out these unwanted background hits. The hit selection for the reconstruction of the shower position is performed on all recorded hits in the event. It selects the subset of hits with the biggest sum of associated charge where all the hits are causally compatible with a common source of emission. The causality criterion every pair of hits has to fulfil is:

$$|\vec{r}_i - \vec{r}_j| \geq c_w \cdot |t_i - t_j| \,, \tag{5.2}$$

with:

$\vec{r}_i$, the position of the OM that recorded hit i,
t_i, the time hit i was recorded and
$c_w = 0.217\,288\,\mathrm{m\,ns^{-1}}$, the speed of light in water for the average Cherenkov light wavelength.

This inequality selects hits that could all have the same cause; but with no hit that causally connects to all other hits. In other words: All hits lie in the forward light-cone (in the sense of Minkowski causality) of a common point of origin, considering a reduced speed of light, c_w. A graphical representation of this hit selection is sketched in figure 5.3.

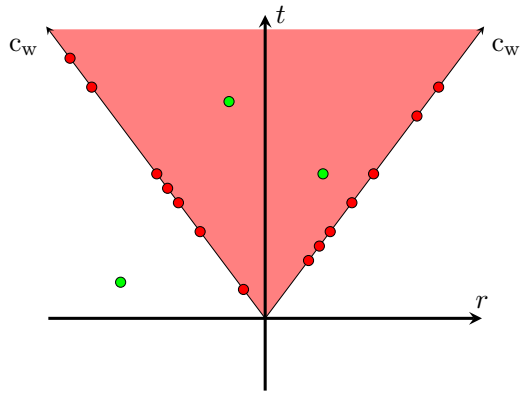

Figure 5.3: Schematic demonstration of the causality hit selection. The red area depicts the future light-cone of a yet to be determined common origin for all selected hits; considering the reduced speed of light in water, c_w. All pairs of red hits are either light-like ($\Delta r = \Delta t\, c_w$, on same edge of the light-cone) or space-like ($\Delta r > \Delta t\, c_w$, opposing edges of light-cone). These are the hits that are selected. The green hits have a time-like relation with several of the red hits ($\Delta r < \Delta t\, c_w$, within each others light-cones). They are not selected.

With this set of selected pulses, this common source of emission – i.e. the shower position – is determined, assuming the following system of quadratic equations:

$$(\vec{r}_i - \vec{r}_{\text{Shower}})^2 = c_W^2 \cdot (t_i - t_{\text{Shower}})^2, \tag{5.3}$$

with:

$1 \leq i \leq N_{\text{selected Hits}}$ and
$\vec{r}_{\text{shower}}$ and t_{shower} the shower position and time.

The system of equation is linearised by taking the difference between every pair of equations i and j:

$$\begin{aligned}(x_i - x_j) \cdot x_{\text{Shower}} + (y_i - y_j) \cdot y_{\text{Shower}} \\ +(z_i - z_j) \cdot z_{\text{Shower}} - (t_i - t_j) \cdot t_{\text{Shower}} c_w^2 \\ = \tfrac{1}{2}[|\vec{r}_i|^2 - |\vec{r}_j|^2 - c_w^2(t_i^2 - t_j^2)]\end{aligned} \tag{5.4}$$

with $i, j:\ 1 \leq i < j \leq N_{\text{selected Hits}}$.

The resulting linear equation system can be written as:

$$\mathbf{A}\vec{v} = \vec{b}, \tag{5.5}$$

with:

$\vec{v}$, the four-dimensional space-time fit for the vertex,

$$\mathbf{A} = \begin{pmatrix} (x_1 - x_2) & (y_1 - y_2) & (z_1 - z_2) & -(t_1 - t_2)\mathrm{c_w} \\ \vdots & \vdots & \vdots & \vdots \\ (x_i - x_j) & (y_i - y_j) & (z_i - z_j) & -(t_i - t_j)\mathrm{c_w} \\ \vdots & \vdots & \vdots & \vdots \\ (x_{N-1} - x_N) & (y_{N-1} - y_N) & (z_{N-1} - z_N) & -(t_{N-1} - t_N)\mathrm{c_w} \end{pmatrix},$$

$$B = \frac{1}{2} \cdot \begin{pmatrix} |\vec{r}_1|^2 - |\vec{r}_2|^2 - \mathrm{c_w}^2(t_1^2 - t_2^2) \\ \vdots \\ |\vec{r}_i|^2 - |\vec{r}_j|^2 - \mathrm{c_w}^2(t_i^2 - t_j^2) \\ \vdots \\ |\vec{r}_{N-1}|^2 - |\vec{r}_N|^2 - \mathrm{c_w}^2(t_{N-1}^2 - t_N^2) \end{pmatrix}$$

and here $N \equiv N_{\text{selected Hits}}$. This equation system is solved by the method of least linear square fit [73].

Least Linear Square Fit

Since the system of equations is over-constrained, there is no exact solution for equation (5.5) in most cases. Therefore, a residual vector $\vec{r}$ is defined:

$$\vec{r} = \mathbf{A}\vec{v} - \vec{b}. \tag{5.6}$$

The square of this vector gives a χ^2-like figure:

$$\begin{aligned} |\vec{r}|^2 &= (\mathbf{A}\vec{v} - \vec{b})^2 && (5.7)\\ &= (\mathbf{A}\vec{v} - \vec{b})^{\mathrm{T}} \cdot (\mathbf{A}\vec{v} - \vec{b}) && (5.8)\\ &= (\mathbf{A}\vec{v})^{\mathrm{T}}(\mathbf{A}\vec{v}) + \vec{b}^{\mathrm{T}}\vec{b} - \vec{b}^{\mathrm{T}}(\mathbf{A}\vec{v}) - (\mathbf{A}\vec{v})^{\mathrm{T}}\vec{b} && (5.9)\\ &= (\mathbf{A}\vec{v})^{\mathrm{T}}(\mathbf{A}\vec{v}) + \vec{b}^{\mathrm{T}}\vec{b} - 2(\mathbf{A}\vec{v})^{\mathrm{T}}\vec{b}. && (5.10) \end{aligned}$$

The minimum of $|\vec{r}|^2$ can be found by taking the derivative of equation (5.10) with respect to $\vec{v}$ and setting it to 0:

$$\frac{d}{d\vec{v}}\left[(\mathbf{A}\vec{v})^{\mathrm{T}}(\mathbf{A}\vec{v}) + \vec{b}^{\,\mathrm{T}}\vec{b} - 2(\mathbf{A}\vec{v})^{\mathrm{T}}\vec{b}\right] \stackrel{!}{=} 0, \tag{5.11}$$

$$2\mathbf{A}^{\mathrm{T}}\mathbf{A}\vec{v} - 2\mathbf{A}^{\mathrm{T}}\vec{b} \stackrel{!}{=} 0. \tag{5.12}$$

This way, $\vec{v}_{\chi^2}$ denotes the minimum χ^2-solution to equation (5.5):

$$\vec{v}_{\chi^2} = (\mathbf{A}^{\mathrm{T}}\mathbf{A})^{-1}\mathbf{A}^{\mathrm{T}}\vec{b}. \tag{5.13}$$

M-Estimator Fit

Subsequently, an M-estimator fit is performed by minimising equation (5.14) and using the previous fit result as the starting point:

$$M_{\mathrm{Est}} = \sum_{i=1}^{N_{\text{selected Hits}}} \left(q_i \cdot \sqrt{1 + t_{\mathrm{res}\,i}^2/2}\right), \tag{5.14}$$

with:

q_i, the charge of hit i,

$t_{\mathrm{res}\,i} = t_i - t_{\mathrm{shower}} - |\vec{r}_i - \vec{r}_{\mathrm{shower}}|\,/c_{\mathrm{W}}$, the *time residual* of hit i.

The M-estimator is a modified χ^2-like figure. Like the χ^2 function, the M_{Est} behaves quadratically for small values of t_{res} but becomes asymptotically linear for larger values. Thus, it is less sensitive to outliers. The minimisation is performed by the TMinuit2 class within the ROOT framework [74].

5.3 Direction Reconstruction

For the direction fit, a dedicated hit selection is performed again on the full set of hits in the event. The charges of all hits on the same PMT in a time residual window of $-200 < t_{\mathrm{res}}/\mathrm{ns} < 500$ with respect to the already performed position fit get summed up while the time of the first hit is taken as the time for the combined hit.

The reconstruction of the neutrino direction is based on the minimisation of the negative log-likelihood function that is defined by equation (5.15). This likelihood function evaluates the probabilities that a hypothetical neutrino ν with energy E_ν, direction $\vec{p}_\nu$ and creating a shower at position $\vec{r}_{\mathrm{shower}}$ causes a hit with the measured charge q on a PMT ($P_{q>0}$). It does so by comparing

the measured charge with the expectation value of the number of photons of such a shower. This expectation value depends on the neutrino energy E_ν, the distance of the hit to the shower d, the photon's emission angle from the shower ϕ and its incident angle on the PMT α. A schematic overview of the geometric variables that go into this signal part of the likelihood function can be seen in figure 5.4. The likelihood also takes into consideration that the hit could be caused by ambient background and evaluates the probability that a background event causes a charge as observed on the PMT (P_{bg}). PMTs that are expected to be working and did not record a hit which passed the hit selection are also taken into account ($P_{q=0}$).

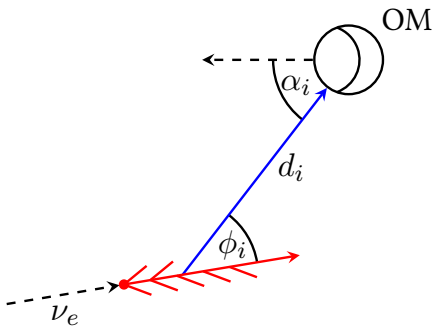

Figure 5.4: Schematic overview of the different geometric variables that are considered by the likelihood function in equation (5.15): photon emission angle ϕ_i, shower–OM distance d_i and photon incident angle α_i.

$$\begin{aligned}\mathscr{L} \;=\; & \sum_{i=1}^{N_{\text{selected Hits}}} \log\left\{P_{q>0}(q_i|E_\nu, d_i, \phi_i, \alpha_i) + P_{\text{bg}}(q_i)\right\} \\ & + \sum_{i=1}^{N_{\text{unhit PMTs}}} \log\left\{P_{q=0}(E_\nu, d_i, \phi_i)\right\} \end{aligned} \tag{5.15}$$

with:

q_i, the charge of hit i,
$P_{q_i>0}$, the probability for a hit PMT to measure its observed charge,
$P_{q=0}$, the probability of a PMT not being hit,
P_{bg}, the probability for random background to have the measured charge,
E_ν, the neutrino energy,
$d_i = |\vec{r}_i - \vec{r}_{\text{shower}}|$, the distance between the shower and PMT with hit i,
ϕ_i, the photon emission angle,
α_i, the photon impact angle on the PMT,
$\vec{r}_{\text{shower}}$, the position of the shower.

5.3.1 The Signal Term – $P_{q_i>0}(q_i|E_\nu, d_i, \phi_i, \alpha_i)$

The charge term of the likelihood function is determined from a three-dimensional table obtained from Monte Carlo simulations. It contains, for a given shower-OM distance d_i, photon-emission angle ϕ_i and photon-impact angle α_i, the expectation value of the number of photons on this PMT for a 1 TeV shower. Figure 5.5 shows a ϕ-d-slice of this table for photons which hit the PMT straight on ($\alpha \approx 0°$). The number of emitted photons – and therefore the number of photons expected on the PMT, N – is proportional to the neutrino energy. For energies different from 1 TeV, the number of photons is scaled accordingly:

$$N(E_\nu) = N_{1\,\mathrm{TeV}} \times E_\nu/1\,\mathrm{TeV} \tag{5.16}$$

The probability to detect n photons when N are expected is given by the Poisson distribution:

$$P(n|N) = \frac{N^n}{n!}\mathrm{e}^{-N}. \tag{5.17}$$

In first order, the charge Q expected to be measured by the OM is assumed to be proportional to the number of photons n arriving on the PMT:

$$Q = n \times \mathrm{PE}, \tag{5.18}$$

but this number of photons cannot be measured with absolute precision. Instead the measured charge q is afflicted by an uncertainty in form of a Gauss centred around the expected charge Q with width $\sigma \sim \sqrt{n}$. For simplicity this smearing of the charge is approximated by a continuous extension of the Poisson formula:

$$P_{\mathbb{R}}(q|N) = \frac{N^q}{\Gamma(q-1)}\mathrm{e}^{-N}. \tag{5.19}$$

However, the OMs saturate at charges above about 20 PE preventing to correctly determine the number of arriving photons. For this reason, to obtain a reasonable probability for the measured charge, the measured charge as well as the expected charge are capped to 20 PE. The proportionality between n and q and the saturation of the measured charge is visible in figure 5.6.

5.3.2 The non-hit Term – $P_{q=0}(E_\nu, d_i, \phi_i)$

The probability to have an unhit PMT is simply the Poisson probability to have zero charge while expecting N photons to arrive on the photocathode:

$$P(N) = P_{\mathbb{R}}(q = 0|N) = \mathrm{e}^{-N}. \tag{5.20}$$

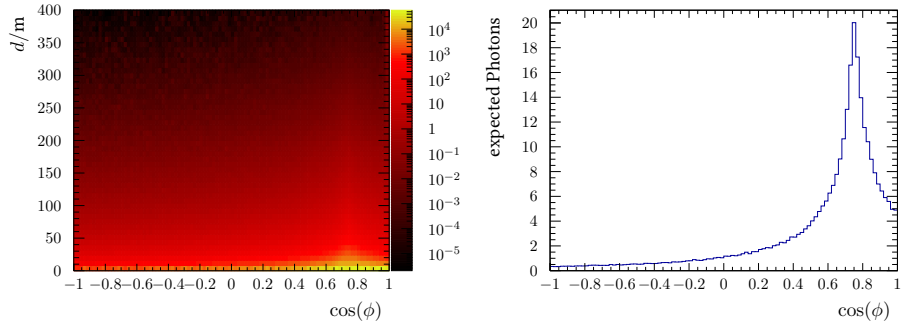

Figure 5.5: Left: Expected number of photons for a 1 TeV neutrino (ν_e, charged current interaction) with dependence on the emission angle ϕ from the neutrino direction and the distance d from the shower's position of mean intensity. **Right:** one-dimensional slice of the left histogram at $d = 100\,\mathrm{m}$

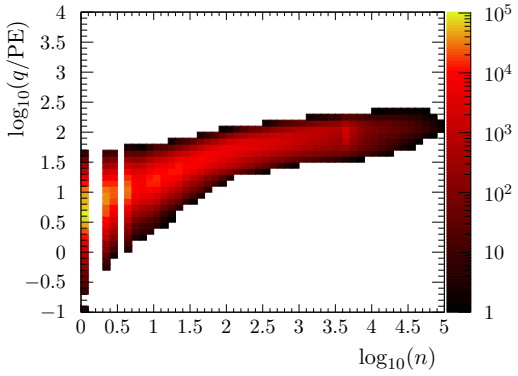

Figure 5.6: The measured charge q in relation with the number of photons n that hit the PMT. The charge is largely proportional to n up to $q \approx 20\,\mathrm{PE}$, where the charge reaches a plateau. Until there, a relation of $q/n = 1\,\mathrm{PE}$ is assumed.

5.3.3 The Background Term – $P_{\mathrm{bg}}(q_i)$

The background term gives the probability that an uncorrelated background event – ^{40}K-decay, bioluminescence etc – causes a hit with the observed charge The distribution shown in figure 5.7 has been obtained from ANTARES optical beacon runs by taking all hits into account with hit times *prior* to the beacon flash. This distribution is assumed to show the unbiased distribution of background charge. The expectation value for the shown distribution is $Q_{\mathrm{bg}} = 1.08\,\mathrm{PE}$.

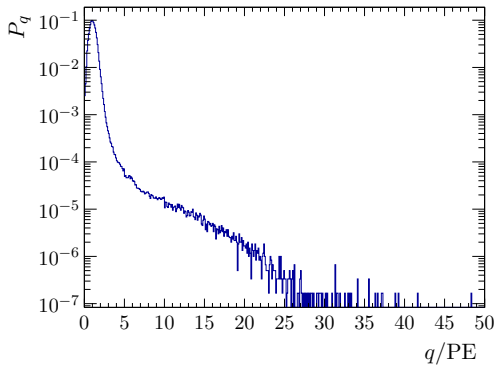

Figure 5.7: Unbiased background charge distribution obtained from triggered optical beacon runs. All hits prior to the beacon flash were taken into account.

5.3.4 Implementation

The direction fit is performed by the TMinuit2 class as well. The algorithms within TMinuit2 expect a continuous likelihood function with a well defined derivative at every point. The PDF used in the fit is provided as a table with discrete bins: Within each bin, the PDF is flat and at the bin edges it jumps from one bin value to the other. To conform with the requirements of the minimiser algorithms, the PDF is interpolated by the method of *trilinear interpolation* which is implemented in ROOT's histogram classes [75].
To find the global minimum and avoid possible local minima in the likelihood landscape, 12 starting points, corresponding to the corners of an icosahedron, are used for the fit. In the end, the fit with the best likelihood value is selected.
To prevent numerical difficulties, like taking the logarithm of 0, each addend i in equation (5.15) has a lower bound of -5. If the actual value of a hit's contribution (after taking the logarithm) is below -5 it gets set back to this value.

5.3.5 Error Estimator

The direction fit also provides an error estimate on the fit direction. After the best direction has been determined, the likelihood landscape around the fit is scanned along concentric circles of angular distances iteratively increasing in 1 degree steps. The angular distance where the difference between likelihood value and the likelihood of the best fit is bigger than 1 is used as the angular error estimate.
To evaluate the reliability of the error estimator, a pull can be defined as the ratio of the real error ξ (the angle between reconstructed shower direction and the parent neutrino direction) and the shower error estimate β_{sh}. This

pull, after the quality criteria described in chapter 6, is shown in figure 5.8. The distribution has a mean of 1.1. This average of about 1 shows that the error estimate is a good description of the uncertainty of the reconstructed direction. A Gauss fit of the peak (red line) has a mean of 0.58 and width of $\sigma = 0.4$.

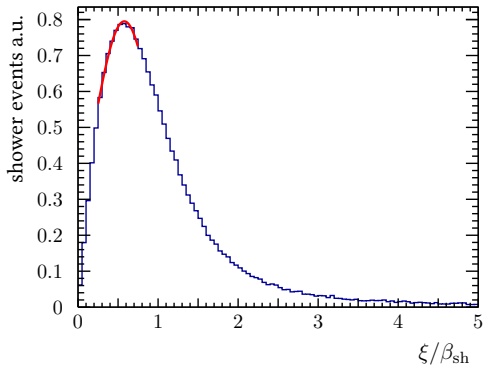

Figure 5.8: The pull distribution of the direction reconstruction as the ratio of the angular error and its estimate: ξ/β_{sh}. The distribution has a mean of 1.1; the Gauss fit of the peak (red line) has a mean of 0.58 and width of $\sigma = 0.4$.

5.4 Performance

The reconstruction performance is shown for two different scenarios: For contained events where the Monte Carlo neutrino vertex lies inside the instrumented detector volume ($\rho_{\mathrm{MC}} < 90\,\mathrm{m}$, $|z_{\mathrm{MC}}| < 200\,\mathrm{m}$, top plots of figures 5.9 and 5.10) and for a realistic selection where the position has to be reconstructed within a reasonable distance around the detector ($\rho_{\mathrm{Shower}} < 300\,\mathrm{m}$, $|z_{\mathrm{Shower}}| < 250\,\mathrm{m}$, bottom plots of the same figures). In either case, a cut on the angular error estimate of 10° has been applied.

5.4.1 Position

The shower position can be reconstructed within about one metre. Figure 5.9 shows the longitudinal (left) and perpendicular (right) offset of the position fit with respect to the Monte Carlo neutrino vertex. For electromagnetic showers (red data points), the reconstructed position along the shower axis corresponds to the mean of the shower's light emission spectrum (purple line in the figure). Hadronic showers (blue data points) have a different emission profile (see section 3.1.1) and are usually reconstructed a bit further along the shower axis. The feature in the em-shower channel just below $E_\nu = 10^7$ GeV is due to the Glashow-Resonance. Here, an anti electron neutrino interacts

with an electron from the ambient water. If, in the electron's rest frame, the incoming neutrino has an energy around 6.3 PeV, the centre of mass energy of the neutrino-electron system corresponds to the mass of a W boson and production of a W^- is highly amplified. If this W^- decays hadronically, it produces a hadronic shower that carries the whole energy of the original neutrino (in contrast to neutral current interactions where the hadronic shower only takes a fraction of the neutrino energy). The observed longitudinal offset, therefore, corresponds to a high-energy hadronic shower and is expected to lie further away than the ones for pure em-showers. For contained events, the median perpendicular distance to the neutrino axis is as low as half a metre in either charged or neutral current over a wide energy range.

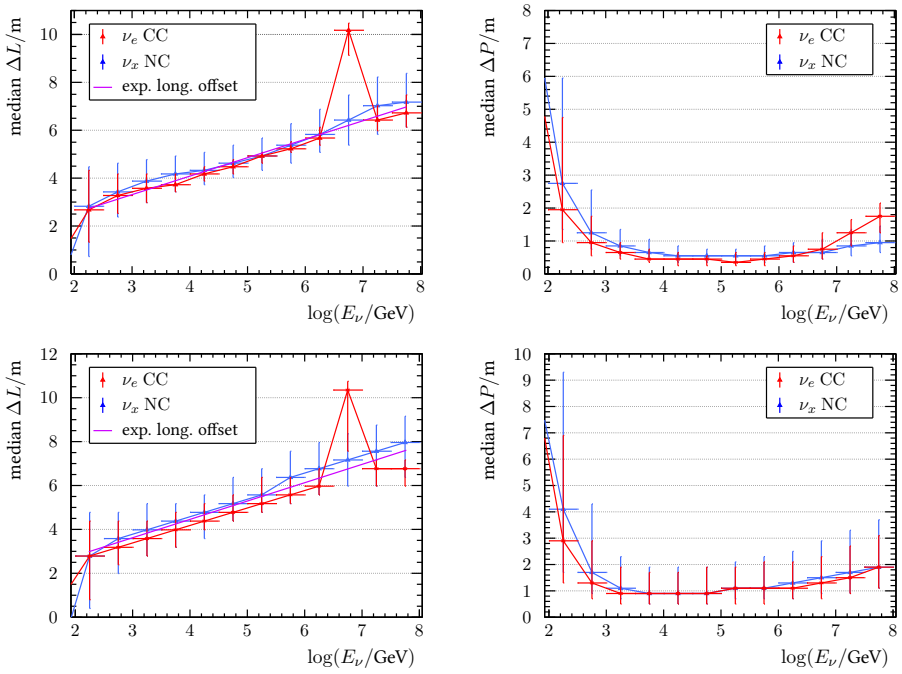

Figure 5.9: Performance of the shower position reconstruction, red for electromagnetic showers, blue for hadronic showers, the purple line is the mean of the light emission spectrum for em-showers – **Left:** The distance between the position of the neutrino interaction vertex and the reconstructed shower position along the neutrino axis. **Right:** The distance of the reconstructed shower position perpendicular to the neutrino axis. **Top:** For contained events ($\rho_{\mathrm{MC}} < 90\,\mathrm{m}$, $|z_{\mathrm{MC}}| < 200\,\mathrm{m}$). **Bottom:** For events close to the detector ($\rho_{\mathrm{Shower}} < 300\,\mathrm{m}$, $|z_{\mathrm{Shower}}| < 250\,\mathrm{m}$).

5.4.2 Direction

The angular resolution of the shower reconstruction is energy dependent. It is defined as the median angle ξ between the simulated neutrino and the reconstructed shower direction. For contained events and energies $10^3 \lesssim E_\nu/\mathrm{GeV} \lesssim 10^6$ it reaches values as low as 2.3° with $16\,\%$ of the events below 2°. Including also events outside of the detector, the angular resolution deteriorates slightly to 3°. Below a neutrino energy of 10^3 GeV, not enough light is produced to illuminate sufficient PMTs for a proper reconstruction and above $E_\nu \approx 10^6$ GeV, the PMTs are starting to saturate and the limited size of the ANTARES detector prevents accessing higher energies with proper resolutions.
In neutral current interactions, only a fraction of the neutrino energy gets transferred to the nucleus that subsequently disintegrates into a hadronic shower. The rest gets carried away by the neutrino. A hadronic shower created by a high-energy neutrino in a NC interaction has correspondingly less energy than an electromagnetic shower created by an electron neutrino of the same energy in a CC interaction. For this reason, the angular resolution for hadronic showers does not deteriorate as quickly with increasing (neutrino) energy as for electromagnetic showers (note that the horizontal axes of the left plots in figure 5.10 show the neutrino energy, not the shower energy).

5.4.3 Energy

A systematic underestimation of about $20\,\%$ in the reconstructed energy can be observed over the whole energy range. This effect is easily corrected so that the median ratio between reconstructed energy and Monte Carlo shower energy is flat at 1 (see figure 5.11). After this correction, a statistical energy resolution of $5 - 10\,\%$ has been achieved. See figure 5.10 for the performance of the direction (left) and energy (right) reconstruction.

5.4.4 Angular Resolution measured in Data

The angular resolution of the cascade reconstruction can also be measured directly in data using a sample of atmospheric muons which also have a reconstructed cascade. If the reconstructed cascade corresponds to a true em-shower which originates from the stochastic muon energy loss, the shower will have the same direction as the muon to a good approximation. As the muon is accurately reconstructed by the track fit, a sample of em-cascades of known direction can be isolated. Figure 5.12 shows the result for a loose selection. A clear population of well reconstructed showers is visible (black

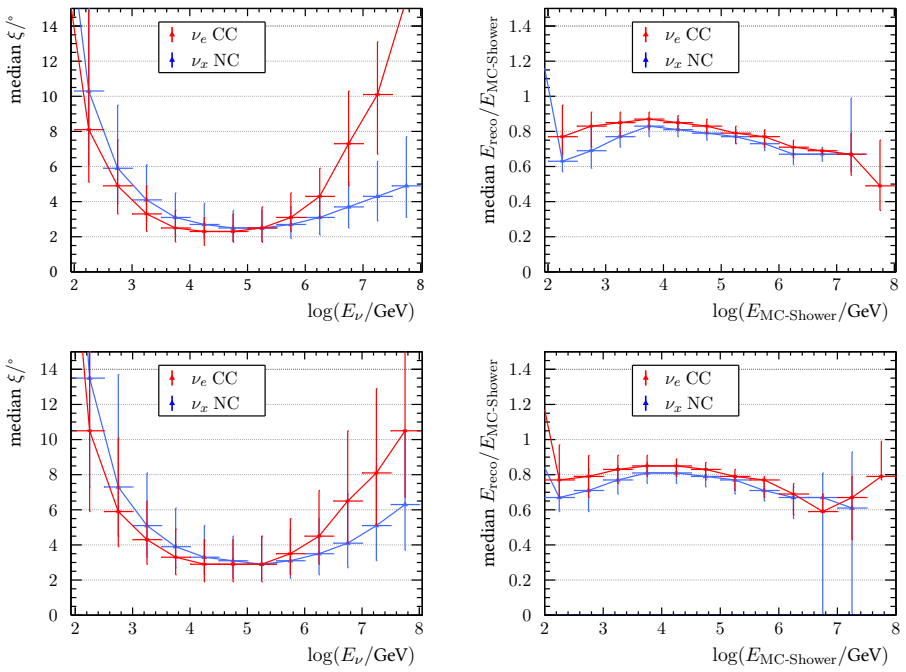

Figure 5.10: Performance of the shower energy-direction reconstruction, red for electromagnetic showers, blue for hadronic showers – **Left:** The angle between the directions of the reconstructed shower and the Monte Carlo neutrino as a function of the neutrino energy. **Right:** The ratio between reconstructed energy and the Monte Carlo shower energy as a function of the shower energy. **Top:** For contained events ($\rho_{\text{MC}} < 90\,\text{m}$, $|z_{\text{MC}}| < 200\,\text{m}$). **Bottom:** For events close to the detector ($\rho_{\text{Shower}} < 300\,\text{m}$, $|z_{\text{Shower}}| < 250\,\text{m}$).

data points); with a resolution of two to three degrees (maximum of the distribution). This peak is well modelled in simulations of atmospheric muons [52] (blue histogram), which implies the Monte Carlo can be reliably used to determine the resolution for cascades of cosmic origin. For the purple histogram, a cut of 5° on the true error between the directions of the simulated and the reconstructed muon has been applied to ensure that the population in the peak are truly well reconstructed events.

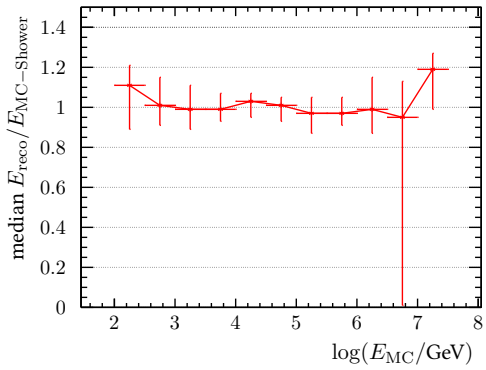

Figure 5.11: The ratio between reconstructed energy and MC shower energy for ν_e charge current events corrected for the bias seen in figure 5.10. All events close to the detector ($\rho_{\mathrm{MC}} < 90\,\mathrm{m}$, $|z_{\mathrm{MC}}| < 200\,\mathrm{m}$) are considered.

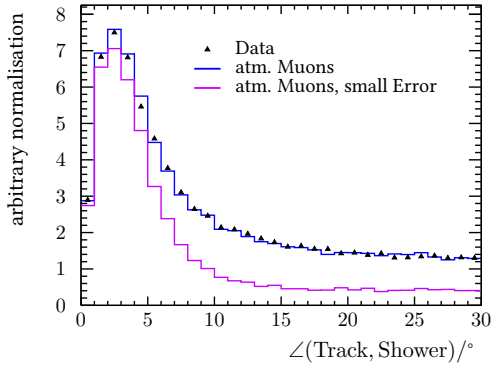

Figure 5.12: The angular separation of the reconstructed directions using track and shower hypotheses applied to the same atmospheric muon events – black: data, blue: atmospheric muons, violet: muons with a track reconstructed better than 5°.

Conclusion

An algorithm for the ANTARES neutrino telescope has been developed to reconstruct underwater particle showers caused by charged current as well as neutral current neutrino interactions. It makes use of the fact that the highly energetic, electromagnetically charged particles induce Cherenkov radiation mainly under one specific angle. The showers can be approximated as point sources of photons which emit their light at one given time. The shower position can be reconstructed with a precision in the order of 1 m. Resolutions of 2° to 3° have been achieved for the direction. After correcting a systematic under-estimation of about 20 %, an energy uncertainty of about $5 - 10$ % can be obtained.

Even though their pointing accuracy is worse by an order of magnitude compared to that of muons, their inherently low topological background makes shower events very valuable to increase sensitivities for point source searches and many other analyses.

Chapter 6

Event Selection

„Siehst, Vater, du den Erlkönig nicht?
Den Erlenkönig mit Kron und Schweif?"
„Mein Sohn, es ist ein Nebelstreif."
Der Erlkönig by Johann Wolfgang von Goethe

This chapter presents the rigour how the events for the final analysis are selected. A first step discards whole runs which do not fulfil certain quality criteria or are otherwise deemed unfit for further physics analysis. Afterwards, the cosmic signal is separated from the atmospheric background as much as possible with a set of event-by-event selection criteria. Those criteria are different for track and shower-like events. The last section of this chapter compares the events that passed the selection with the corresponding run-by-run Monte Carlo simulation.

6.1 Run Selection

The data are organised into runs. The runs considered in this analysis reach from the early 5-line period in 2007 until the end of 2013. While early runs have a duration of 2 h, the run time increased continually over the years until a duration of 12 h was reached. A data quality parameter gets assigned to every run. This quality parameter assesses the performance of the detector and the environmental conditions during the run time. A value of 1 assures that there where no major hardware problems and that the database was properly filled. Higher values put further constraints on the number of active OMs and the intensity of the ambient background. For this analysis, only runs with a data quality of 0 have been discarded.
Some runs evince events with a large number of recorded hits. Those high multiplicities are thought to be caused by OMs experiencing a voltage surge producing a flash of light – so called *sparking OMs*. Such electric sparks produce light very similar to the electromagnetic shower events this analysis is

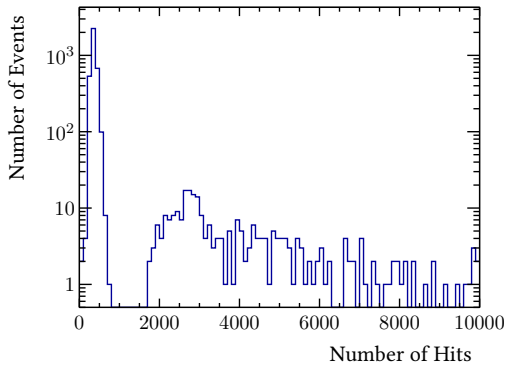

Figure 6.1: Distribution of the number of hits per event for Run 34663. The large fraction of events with over 2000 hits clearly identifies this run as sparking.

Table 6.1: Number of selected runs and corresponding live time over the years.

Year	Number of Runs	Days of Live Time
2007	1484	253.2
2008	1992	182.7
2009	1647	209.5
2010	2451	244.7
2011	3294	289.9
2012	2445	231.2
2013	1112	279.4
total	14 425	1690.5

looking. It is therefore important to identify such sparking events. Figure 6.1 shows the number of hits distribution for one run that has been found to contain sparks. This run contains events with up to 10 000 hits. With less than 1000 active OMs in the detector, this means that many PMTs must have been hit several times over. Runs containing so many events with such a high light yield are most probably caused by sparking OMs and not by cosmic neutrinos. Runs that are flagged as "sparking" were discarded. Table 6.1 presents the number of selected runs and their corresponding live time broken down by years of data taking.

6.2 Selection of Muon Tracks

The selection of muon candidates was adapted from the previous – muon only – point source analysis [76]. Events have to be triggered by the T3 or 3N trigger, reconstructed as up-going ($\cos(\vartheta_{\mathrm{tr}}) > -0.1$) , with a good quality parameter ($\Lambda_{\mathrm{tr}} > -5.2$) and a small estimated angular error ($\beta_{\mathrm{tr}} < 1^{\circ}$). The goal is to reject atmospheric background as well as ensuring a well reconstructed object with a precise direction estimate. The selection criteria are summarised in table 6.2. After this selection, 6490 muon candidates remain in the data, of which 15 % are estimated to be atmospheric muons erroneously reconstructed as up-going. Table 6.4 shows the contribution of the various channels – estimated from Monte Carlo simulation – to this number of selected events.

Table 6.2: Criteria for the muon candidate event selection and the selection efficiency after each step for atmospheric muons and neutrinos and cosmic neutrinos creating a muon track in the detector. The efficiencies are defined as the ratio of the number of events that passed a cut and the number of events after the trigger selection.

Criterion	Condition	$\varepsilon_{\mu}^{\mathrm{atm}}$	$\varepsilon_{\nu\rightarrow\mathrm{any}}^{\mathrm{atm}}$	$\varepsilon_{\nu_{\mu}\rightarrow\mu}^{E^{-2}}$
triggered	T3 or 3N	1	1	1
up-going	$\cos(\vartheta_{\mathrm{tr}}) > -0.1$	8.3×10^{-2}	0.83	0.67
Quality	$\Lambda_{\mathrm{tr}} > -5.2$	5.3×10^{-6}	0.11	0.31
Error Estimate	$\beta_{\mathrm{tr}} < 1^{\circ}$	2.6×10^{-6}	0.10	0.30

6.3 Selection of Shower Events

Due to the reduced angular resolution compared to muons and the fact that muons can also induce electromagnetic showers along their track, it is a much more elaborate task to separate the astrophysical shower signal from the showers produced by the various particles created in earth's atmosphere. The selection requires that the event was triggered by the T3 or 3N trigger and that the shower is reconstructed as up-going ($\cos(\vartheta_{\mathrm{sh}} > -0.1$) with a restriction on the angular error estimate ($\beta_{\mathrm{sh}} < 10^{\circ}$) as well as cuts on the event topology. After the selection procedure, 172 shower events remain. Table 6.3 gives an overview of all the criteria applied for the shower selection. Due to the large number of selection criteria, the exact cut values where not systematically optimised for best sensitivity or discovery potential in the point source

search. Instead, the focus was set to reduce the atmospheric muon contamination as much as possible while maintaining the cosmic signal. Some of the less obvious cuts are explained in the following:

Track Veto To avoid an overlap between the track and shower samples, events that pass the muon track selection are omitted from the shower channel.

Containment+M-Estimator Reconstructing atmospheric muons with a shower algorithm often produces "shower positions" that lie far away from the detector and have a large M_{Est} value. A rough selection on position and reconstruction quality reduces the amount of background by 70 % already before the direction fit. In this selection ρ_{sh} is the radial distance of the reconstructed shower position from the detector's vertical axis and z_{sh} is the vertical height above the detector's centre.

GridFit Ratio The GridFit algorithm was developed for another, recent analysis [77]. In a first step, it segments the full solid angle in 500 different directions. For each, the number of hits compatible with a muon track of this direction is determined. The GridFit ratio R_{GF} is the ratio between the sum of the compatible hits of all up-going and all down-going test directions: $R_{\mathrm{GF}} = \frac{\sum_{\mathrm{up}} N_{\mathrm{Hits}}}{\sum_{\mathrm{down}} N_{\mathrm{Hits}}}$. A lower number, therefore, means a higher likelihood of this event to be a down-going muon. A selection criterion combining the GridFit ratio and the number of selected shower hits – demonstrated in figure 6.2 – was devised to further suppress the atmospheric muon background.

Muon Veto To discriminate between showers and atmospheric muons even more, a dedicated likelihood has been developed. This likelihood considers only hits that coincide with another hit on the same storey within 20 ns and its PDF is based on the following parameters:

- time residual t_{res} of the hits,
- number N of on-time hits ($-20 < t_{\mathrm{res}}/\mathrm{ns} < 60$) and
- distance d of the hits to the reconstructed shower position.

The parameter to distinguish between showers and muons then is:

$$\mathscr{L}_{\mu\mathrm{Veto}} = \sum_{\mathrm{Hits}} \log\{P_{\mathrm{sig}}/P_{\mathrm{bkg}}\} + P_{\mathrm{sig}} - P_{\mathrm{bkg}},$$

with $P_{\mathrm{sig}} = P(N, d, t_{\mathrm{res}}|\mathrm{shower})$ and $P_{\mathrm{bkg}} = P(N, d, t_{\mathrm{res}}|\mathrm{muon})$. The distribution for this quantity plotted for atmospheric muons and

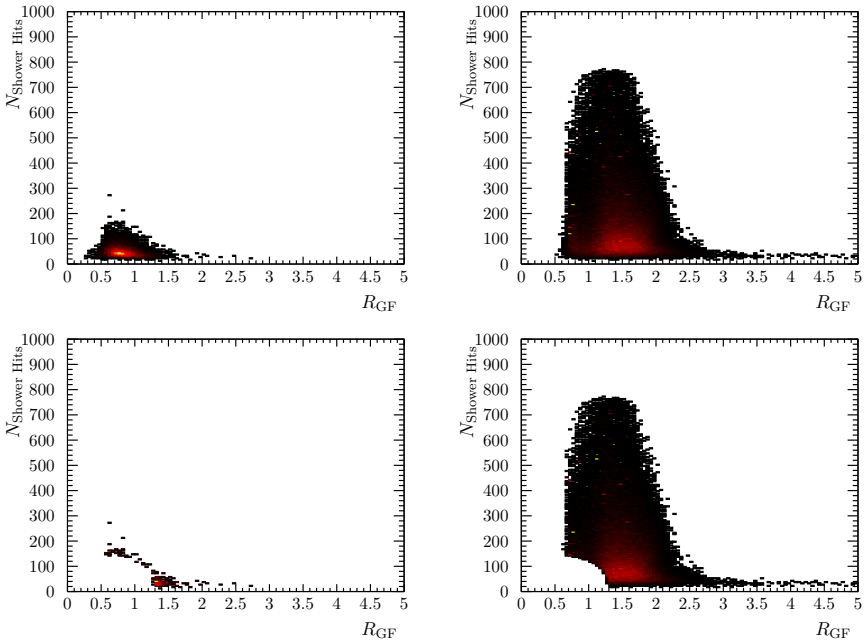

Figure 6.2: Number of selected hits versus GridFit Ratio: **Left:** for atmospheric muons – **Right:** for cosmic electron-neutrinos undergoing charged current interaction creating showers. **Top:** Before and **Bottom:** after a combined R_{GF}–N_{Hits} cut; both after the error estimator and all previous cuts listed in table 6.3.

cosmic showers is shown in figure 6.3. This method further reduces the number of atmospheric muons by more than an order of magnitude. Even so, the majority of events consists still of misreconstructed atmospheric muons.

Charge Ratio When the shower fit reconstructs a position along the muon track, one would expect photons induced by the muon to also arrive earlier than predicted by a point source hypothesis. Thus, the charge ratio between the early and on-time hits was investigated. The distribution of the ratio of those two charge-sums is shown in figure 6.4. Here, Q_{early} is the summed charge of all hits with a time residual of $-1000 \leq t_{\text{res}}/\text{ns} \leq -40$ with respect to the reconstructed shower and $Q_{\text{on-time}}$ is the summed charge of all hits with time residuals of $-30 \leq t_{\text{res}}/\text{ns} \leq 1000$.

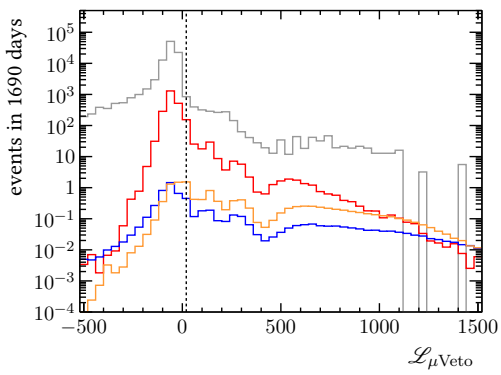

Figure 6.3: Likelihood ratio parameter to distinguish atmospheric neutrinos (red) and muons (grey) from showers caused by astrophysical neutrinos (orange). After the GridFit Ratio and all previous cuts listed in table 6.3. The dashed line marks the cut value: Everything to the left is rejected. For a legend of the colour scheme, see figure 6.5.

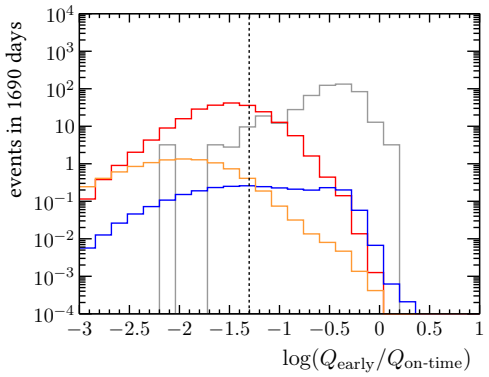

Figure 6.4: Ratio of the sum of the charges for early and on-time hits for cosmic showers (orange) and muons (grey). After the muon veto and all previous cuts listed in table 6.3. The dashed line marks the cut value: Everything to the right is rejected. For a legend of the colour scheme, see figure 6.5.

Table 6.3: Criteria for the shower event selection and the selection efficiency after each step for atmospheric muons and neutrinos and cosmic neutrinos creating a shower in the detector. The efficiencies are defined as the ratio of the number of events that passed a cut and the number of events after the trigger selection.

Criterion	Condition	$\varepsilon_{\mu}^{\text{atm}}$	$\varepsilon_{\nu\to\text{any}}^{\text{atm}}$	$\varepsilon_{\nu\to\text{sh}}^{E^{-2}}$
triggered	T3 or 3N	1	1	1
Containment	$\rho_{\text{sh}} < 300\,\text{m}$, $\lvert z_{\text{sh}}\rvert < 250\,\text{m}$	0.41	0.68	0.97
M-Estimator	$M_{\text{Est}} < 1000$	0.31	0.55	0.97
Track Veto	not selected as muon candidate	0.31	0.49	0.96
up-going	$\cos(\vartheta_{\text{sh}}) > -0.1$	0.11	0.37	0.55
Error Estimate	$\beta_{\text{sh}} < 10^{\circ}$	5×10^{-3}	4.2×10^{-2}	0.36
GridFit Ratio	$\left(\frac{R_{\text{GF}}}{1.3}\right)^3 + \left(\frac{N_{\text{sh Hits}}}{150}\right)^3 > 1$	7×10^{-4}	3.5×10^{-2}	0.32
Muon Veto	$\mathscr{L}_{\mu\text{Veto}} > 20$	1.4×10^{-5}	3.2×10^{-3}	0.27
Charge Ratio	$Q_{\text{early}}/Q_{\text{on-time}} < 0.05$	5.2×10^{-7}	2.4×10^{-3}	0.26

6.4 Data / Monte Carlo Comparison

The selection criteria to separate the signal from the background and their efficiencies have been estimated from simulations. It is therefore crucial that the Monte Carlo properly describes the data. To ensure a good agreement, several key observables can be compared. Matching data-Monte Carlo distributions would attest a good understanding of the involved physical processes and the overall detector performance. Figure 6.5 compares the various Monte Carlo channels with the final data set for the track channel and in figure 6.6 for the shower channel. The agreement between data and Monte Carlo is generally quite good but the simulation overestimates the number of events by 12 % in the track and 6 % in the shower channel. Table 6.4 also shows the total number of selected events and their prediction by the simulation.

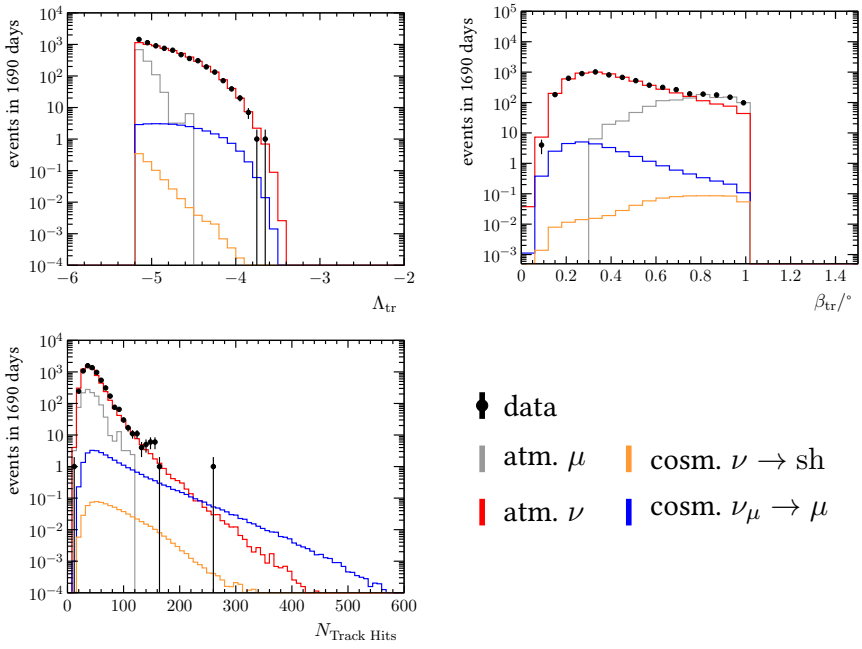

Figure 6.5: Comparison of the data with the Monte Carlo simulation in some observable quantities in the track channel. In reading order: The quality parameter Λ_{tr}, the angular error estimate β_{tr} and the number of hits selected for the final direction fit. For the cosmic neutrinos, a flux according to $d\Phi/dE = 10^{-8}\,(E/\mathrm{GeV})^{-2}\mathrm{GeV}^{-1}\,\mathrm{cm}^{-2}\,\mathrm{s}^{-1}$ was assumed. Applied are all muon track selection criteria presented in table 6.2.

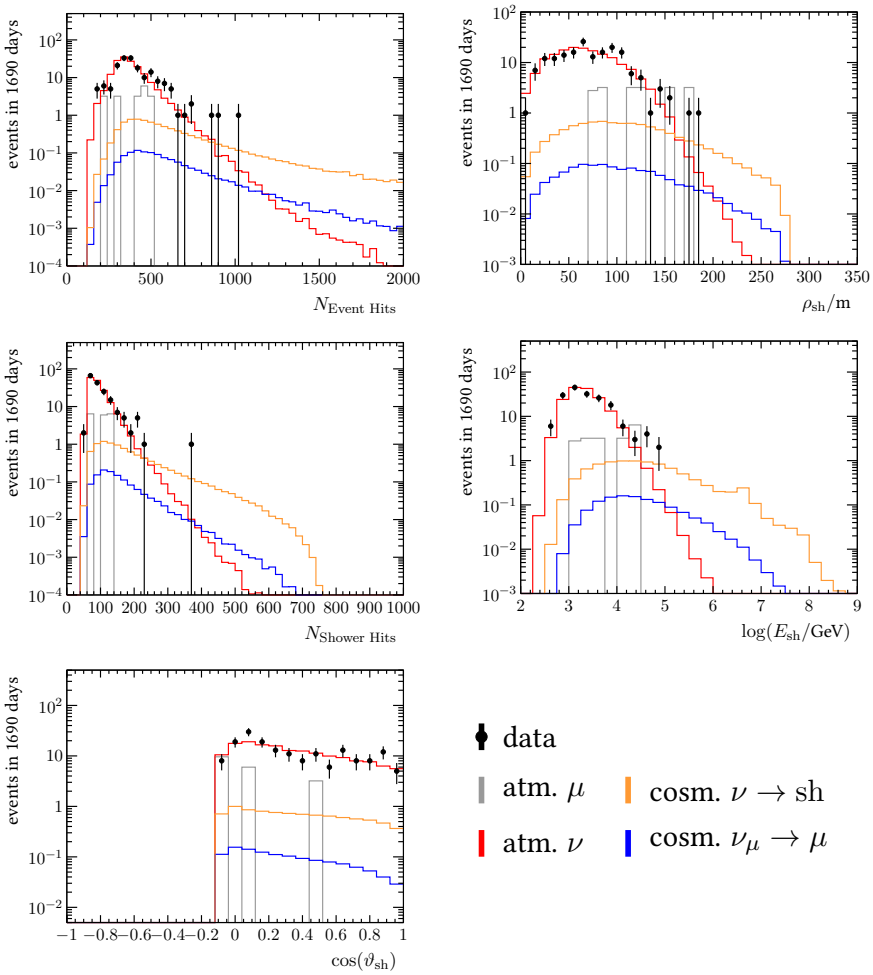

Figure 6.6: Comparison of the data with the Monte Carlo simulation in some observable quantities in the shower channel. In reading order: Number of recorded hits in the event, distance of the reconstructed shower position from the nominal detector axis, number of hits selected for the shower direction fit, reconstructed (uncorrected) shower energy and the elevation of the reconstructed shower direction. For the cosmic neutrinos, a flux according to $d\Phi/dE = 10^{-8}\,(E/\text{GeV})^{-2}\text{GeV}^{-1}\,\text{cm}^{-2}\,\text{s}^{-1}$ was assumed. Applied are all shower selection criteria presented in table 6.3.

Conclusion

A total of 14 425 runs from early 2007 until the end of 2013 have been selected for analysis. The corresponding live time is 1690.5 days. After the event selection procedure, 6490 muon track candidates and 172 showers remain in the data sample. Of the selected muon tracks, 16 % are estimated to be atmospheric muons misreconstructed as up-going, while 52 % of the shower events are caused by atmospheric muons or muon neutrinos that produce a muon track in the detector. The Monte Carlo describes the data well in shape but slightly overestimates the total number of events.
All selected track and shower events can be seen in the sky map of figure 6.7.

Table 6.4: Number of selected muon track and shower candidates and their prediction from Monte Carlo simulations. The numbers for the cosmic signal contributions are for a diffuse flux according to $d\Phi/dE = 10^{-8}\,(E/\mathrm{GeV})^{-2}\mathrm{GeV}^{-1}\,\mathrm{cm}^{-2}\,\mathrm{s}^{-1}$. The Monte Carlo slightly over-estimates the number of selected events.

Source	Muons Tracks	Showers
atm. muons	1130	18.8
atm. ν_μ CC	6099	75.2
atm. ν_x NC	18.7	63.1
atm. ν_e CC	8.36	24.7
E^{-2} ν_μ CC	28.2	1.26
E^{-2} ν_x NC	0.201	2.19
E^{-2} ν_e CC	0.544	4.09
total MC	7256	182
data	6490	172

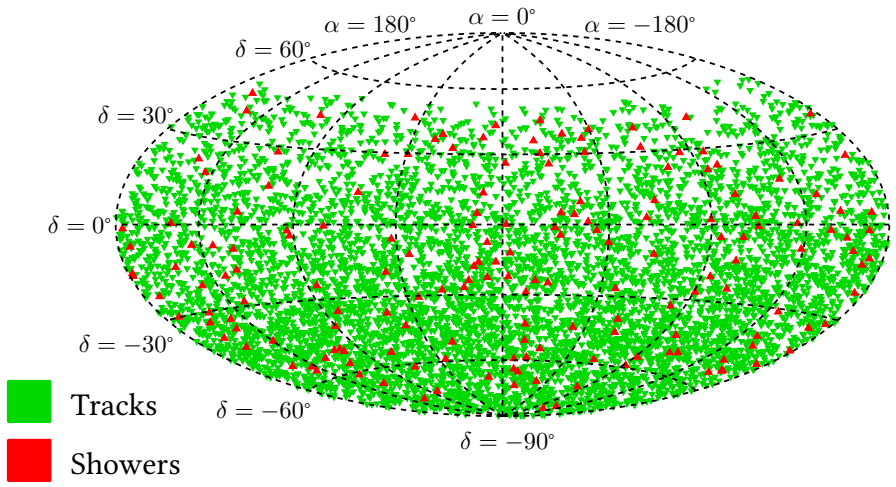

Figure 6.7: Sky map in equatorial coordinates with all track (green) and shower (red) candidates that passed the events selection criteria.

Chapter 7

Point-Source Search

"Nothing will stand in our way. I will finish what you started."
Kylo Ren – Star Wars: The Force Awakens

This chapter gives an introduction to the statistical method used in the analysis: the maximum likelihood ratio (see references [73,78,79] for more details). Subsequently, the specific implementation of an unbinned likelihood and its ingredients are discussed. Finally, the various search methods used here and the rigour of calculating limits, discovery potential and the sensitivity is presented.

7.1 Likelihood-Functions

Given a measurement x and a hypothesis H, the likelihood $\mathscr{L}(x|H) = \mathscr{L}(H)$ is defined as the probability that a hypothesis H produces the observed data x in form of a probability density function (PDF). Here, x can be a single number, one repeatedly measured observable or a set of several independent variables. $H = \{h_0, h_1, \dots\}$ represents the set of parameters that define the tested hypothesis. If all the parameters h_i are known, the hypothesis is called *simple*. If there are free or unknown parameters, then H is called a *composite hypothesis*.
Estimates for the free parameters describing such a composite hypothesis can be obtained from the measurements by finding the hypothesis $\hat{H}$ that maximises $\mathscr{L}(H)$: the *maximum likelihood estimator* (MLE). That means, all the parameters h_i must simultaneously fulfil the following equation, as long as they are not at the boundary of the allowed parameter space:

$$\frac{\partial \mathscr{L}(H)}{\partial h_i} = 0, \qquad \forall h_i \in H. \tag{7.1}$$

To quantify the level of agreement between the data and a given hypothesis, a function of the measured data, called *test statistic*, $\mathcal{Q}(x)$ can be constructed.

This function infers an associated PDF for each of the investigated hypotheses, e.g. $g(\mathcal{Q}|H_0)$ and $g(\mathcal{Q}|H_1)$. These PDFs are preferably well separated as figure (7.1) illustrates. A critical value for the test statistic, $\mathcal{Q}_{\text{crit}}$, can be defined. If the test statistic of the measured data is lower than the critical value, $\mathcal{Q}(x) < \mathcal{Q}_{\text{crit}}$, H_0 gets accepted as the preferred hypothesis. Otherwise, it gets rejected in favour of H_1.
Given a $\mathcal{Q}_{\text{crit}}$, the probability to measure a $\mathcal{Q}(x) > \mathcal{Q}_{\text{crit}}$ even though hypothesis H_0 is true and therefore falsely rejecting it, is called *significance* α:

$$\alpha = \int_{\mathcal{Q}_{\text{crit}}}^{\infty} g(\mathcal{Q}|H_0)\, d\mathcal{Q}. \tag{7.2}$$

This wrongly rejecting of H_0 is called *error of first kind*. Similarly, the probability to accept H_0 even though H_1 is true is

$$\beta = \int_{-\infty}^{\mathcal{Q}_{\text{crit}}} g(\mathcal{Q}|H_1)\, d\mathcal{Q} \tag{7.3}$$

and is considered an *error of second kind* and thus defines the *power* of the test as $(1-\beta)$ to discriminate H_0 against the alternative H_1. The significance α is also called *p-value*.

The Neyman-Pearson lemma [79] states that, for a given significance σ, the most powerful test statistic to distinguish between two simple hypotheses is the *likelihood ratio*:

$$\mathcal{Q}(x) = \frac{\mathscr{L}(x|H_0)}{\mathscr{L}(x|H_1)}. \tag{7.4}$$

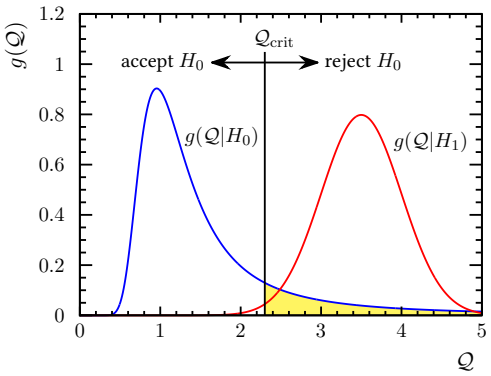

Figure 7.1: Two example PDFs g for a test statistic $\mathcal{Q}$ under the assumption of different hypotheses H_0 and H_1. A (here arbitrarily) set $\mathcal{Q}_{\text{crit}}$ determines whether H_0 gets accepted or rejected in favour of H_1 given a measurement $\mathcal{Q}(x)$. The fraction of $g(\mathcal{Q}|H_0)$ right of $\mathcal{Q}_{\text{crit}}$ (yellow area) is the significance α.
Recreated from [73].

Significances are often expressed in number of corresponding standard deviations σ of a Gaussian normal distribution, e.g. 1σ corresponds to a significance of $\alpha \approx 0.32$, 3σ to $\alpha \approx 2.7 \cdot 10^{-3}$ and 5σ corresponds to an α of about $5.7 \cdot 10^{-7}$. The latter two – especially the 5σ threshold – are often used in high energy physics: To claim a discovery, the measured data have to produce a test statistic $\mathcal{Q}(x)$ beyond a $\mathcal{Q}_{\text{crit}}$ for which $\alpha = 5\sigma$.

7.2 Search Method

The focus of the work presented in this thesis is to search for point-like sources of astrophysical neutrinos in the data provided by ANTARES. These data consist of track and shower event candidates that are distributed over the sky. The distributions of the atmospheric background and the hypothetical cosmic signal neutrinos are parametrised as described in the following subsections.
Three different searches where performed:

Full Sky Search: The whole sky is scanned for clusters of events.

Candidate List Search: The coordinates of a list of pre-selected candidates are evaluated as a possible neutrino source. The direction is fixed and only the magnitude of the signal is estimated.

Search around the Galactic Centre Similar to the full sky search, this search looks for point-sources close to the galactic centre. The restricted region is an ellipsis with semi axes of 30° and 15°. A number of high-energy IceCube events are located in this region but could not be attributed to a single point-source. For this reason, also extended sources are considered in this approach.

7.2.1 Acceptance

To make any claims about the signal coming from a cosmic source candidate, one has to translate the detector response, i.e. the number of detected signal events, into a flux (or an upper limit thereof). The flux of a cosmic point-source is usually parametrised in the form of

$$\frac{d\Phi}{dE_\nu} = \Phi_0 \left(\frac{E_\nu}{\text{GeV}} \right)^{-\gamma}, \tag{7.5}$$

with Φ_0 typically expressed in units of unitFluxNorm. If not mentioned otherwise, γ is assumed to be 2, leading to a so-called "E^{-2} spectrum". This

leaves the normalisation factor Φ_0 as the only free parameter for the flux. The declination-dependent *acceptance*, $\mathcal{A}(\delta)$, serves the purpose to translate between this flux and the detector response as the proportionality constant between the flux normalisation Φ_0 and the number of signal events N_{sig}. It can be expressed in terms of effective area:

$$\mathcal{A}(\delta) = \Phi_0^{-1} \iint dt dE_\nu \; A_{\text{eff}}(E_\nu, \delta) \frac{d\Phi}{dE_\nu}. \tag{7.6}$$

Here, the integral is over the live time of all selected runs (1690.5 days) and over an energy range large enough to include all potential events within ANTARES' sensitivity. Energies from 10^2 GeV to 10^8 GeV are considered. To put limits on this Φ_0 for various proposed candidate sources will be the main quantitative aim of this work.
Figure 7.2 shows how the acceptances for tracks (left) and showers (right) depends on the declination. Due to one of the selection criteria presented in chapter 6 – the neutrinos have to be reconstructed as up-going in the local coordinate system – the events are not uniformly distributed over the whole sky. This cut, the geographic location of ANTARES and its rotation around the Earth's axis cause this peculiar shape of the acceptance: Regions with declinations below $\delta \approx -43°$ are always visible for ANTARES and the acceptance is flat. For increasing declinations, potential sources spend less and less time below the local horizon and the acceptance falls continuously until $\delta \approx 43°$, where sources never drop below the horizon into ANTARES' field of view and the acceptance becomes zero. The plots can essentially be read as the number of events a source at a given declination would cause in the detector. At the plateau around $\sin(\delta) = -0.8$, the acceptance for muon tracks is $\mathcal{A} = 2.2 \times 10^8\,\text{GeV}^{-1}\,\text{cm}^2\,\text{s}$. Here, a muon neutrino flux with a normalisation factor of $\Phi_0 = 10^{-8}\,\text{GeV}\,\text{cm}^{-2}\,\text{s}^{-1}$ would cause $N_{\text{sig}} = \mathcal{A} \times \Phi_0 = 2.2$ signal events in the detector.
In this range of highest visibility, the shower channel contributes about $0.6/(0.6 + 2.2) \approx 21\,\%$ to the total acceptance and therefore number of expected signal events.

Tau Neutrinos

Tau neutrinos have not been simulated. To account for them anyway, the acceptances of charged current ν_e and ν_μ and neutral current events have been scaled up assuming equal cross sections and a flux ratio of 1:1:1 between the three neutrino flavours – ν_e, ν_μ and ν_τ. The total number of the neutral current interactions is estimated as three times the average between the ν_e and

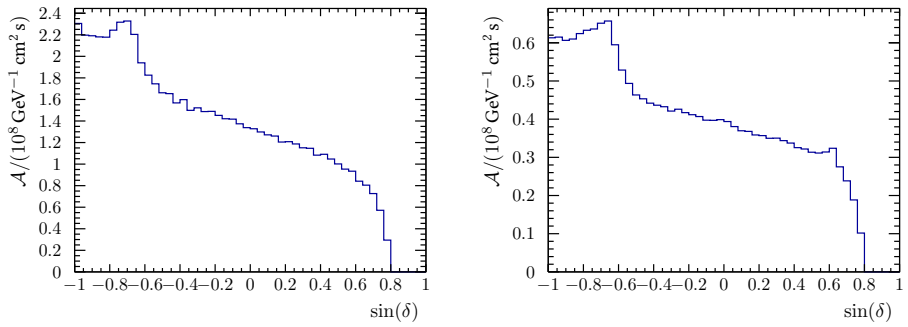

Figure 7.2: The acceptance in dependence of the declination for an E^{-2} energy spectrum with a flux normalisation factor of $\Phi_0 = 10^{-8}\,\mathrm{GeV\,cm^{-2}\,s^{-1}}$ for **Left:** Muon tracks and **Right:** Showers.

ν_μ interactions: $N_{\mathrm{tot}}^{\mathrm{NC}} = 3 \cdot (N_e^{\mathrm{NC}} + N_\mu^{\mathrm{NC}})/2$. The electron neutrino charged current interactions get scaled up by a factor of 1.81 – additional contributions of 0.17 coming from the $\tau \to e$ and 0.64 from the $\tau \to hadr.$ branching ratios of the tau decay. This implies that the hadronic τ-decay channel is approximated by the channel of electron induced em-showers. Since the reconstruction performance and selection efficiencies of hadronic and electromagnetic showers are quite similar, this approximation is justified. Like the electron neutrino charged current channel, the contribution of $\nu_\mu \to \mu$ events has been scaled up by a factor of 1.17 to account for $\tau \to \mu$ decays. This approximation ignores the one or two neutrinos produced in the tau decays (one neutrino for hadronic, two for leptonic decays) and the energy they carry away.

7.2.2 Point Spread Function

A point-source would manifest itself in the data as a cluster of events. The distribution of signal events around a hypothetical point-source is described by the point spread function (PSF) $\mathscr{F}(\xi)$. It is the PDF to find a reconstructed event with an angular distance of ξ around the direction of the original neutrino and depends on the angular resolution of the event type. Figure 7.3 shows the PSFs and the cumulative distributions of the angular errors for tracks and showers. The PSFs have been determined from Monte Carlo simulations of neutrinos with an E^{-2} energy spectrum. The figure shows that, while not reaching the superior resolution of the muon track channel, 60 % of the shower events are reconstructed within 3° of the parent neutrino.

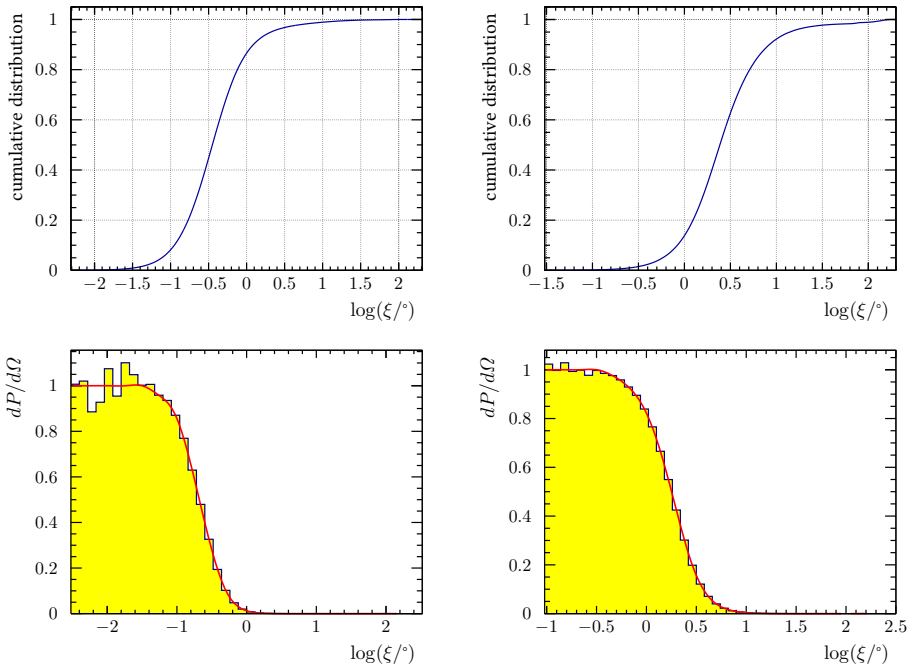

Figure 7.3: Top: Cumulative distribution of the angle between reconstructed object and Monte Carlo neutrino – **Bottom:** Point spread function for a neutrino flux with an E^{-2} spectrum. The red curve is a spline parametrisation of the yellow histogram and used in the likelihood function – **Left:** for muon tracks and **Right:** for shower events.

7.2.3 Background Rate

Given the small expected contribution of a cosmic signal in the overall data set, the background rate is directly taken from the measured data. The rate of the selected events as function of declination and right ascension can be seen in figure 7.4. The event rate shows a clear declination dependence, similar to the acceptance, but is uniform with respect to right ascension. This is due to the Earth's rotation and a sufficiently uniform exposure throughout the (sidereal) day. A constant fit to the data yields $\chi^2/N_{\mathrm{DoF}} = 102/99$ for the track channel and $\chi^2/N_{\mathrm{DoF}} = 5.3/19$ for the shower channel. The background is described by the parametrisation $\mathscr{B}(\delta)$:

$$\mathscr{B}(\delta) = \frac{dN}{d\Omega} = \frac{1}{2\pi} \cdot \frac{dN}{d\sin(\delta)}. \tag{7.7}$$

The shower channel's reduced background rate compensates for its worse angular resolution.

7.2.4 Number of selected Hits

Neutrinos generated in the atmosphere have a much softer energy spectrum than the neutrinos from an expected astrophysical E^{-2} flux. A previous study has shown, for the track channel, that using the number of selected hits N to distinguish between those two sources results in a better sensitivity than using the reconstructed energy [80]. Also in the shower channel the number of selected hits promises a better distinction between cosmic signal and atmospheric background compared to the reconstructed energy (cf. figure 6.6). The signal and background distributions are described by $\mathscr{N}_{\mathrm{sig}}(N)$ and $\mathscr{N}_{\mathrm{bkg}}(N)$, respectively. Figure 7.5 shows the distributions of the number of selected hits for tracks and showers.

7.2.5 Implementation of the Likelihood Function

All the ingredients presented in the previous sections are considered by the likelihood function:

$$\begin{aligned}\log \mathscr{L}_{\mathrm{s+b}} = &\sum_{\mathcal{S}} \sum_{i \in \mathcal{S}} \log \left[\mu^{\mathcal{S}}_{\mathrm{sig}} \cdot \mathscr{F}^{\mathcal{S}}(\xi_i) \cdot \mathscr{N}^{\mathcal{S}}_{\mathrm{sig}}(N_{\mathrm{i}}) + \mathscr{B}^{\mathcal{S}}(\delta_i) \cdot \mathscr{N}^{\mathcal{S}}_{\mathrm{bkg}}(N_{\mathrm{i}}) \right] - \mu^{\mathcal{S}}_{\mathrm{sig}} \\ &+ \mathscr{P}(\mu^{\mathrm{sh}}_{\mathrm{sig}} | \mu^{\mathrm{tr}}_{\mathrm{sig}} \cdot \mathcal{A}^{\mathrm{sh}}(\delta_{\mathrm{s}}) / \mathcal{A}^{\mathrm{tr}}(\delta_{\mathrm{s}}))\end{aligned} \tag{7.8}$$

Here, $\sum_{\mathcal{S}}$ is the sum over the different classes of events, i.e. tracks and showers and $\sum_{i \in \mathcal{S}}$ is the sum over all the events of this class. The $\mathcal{S}$ superscript

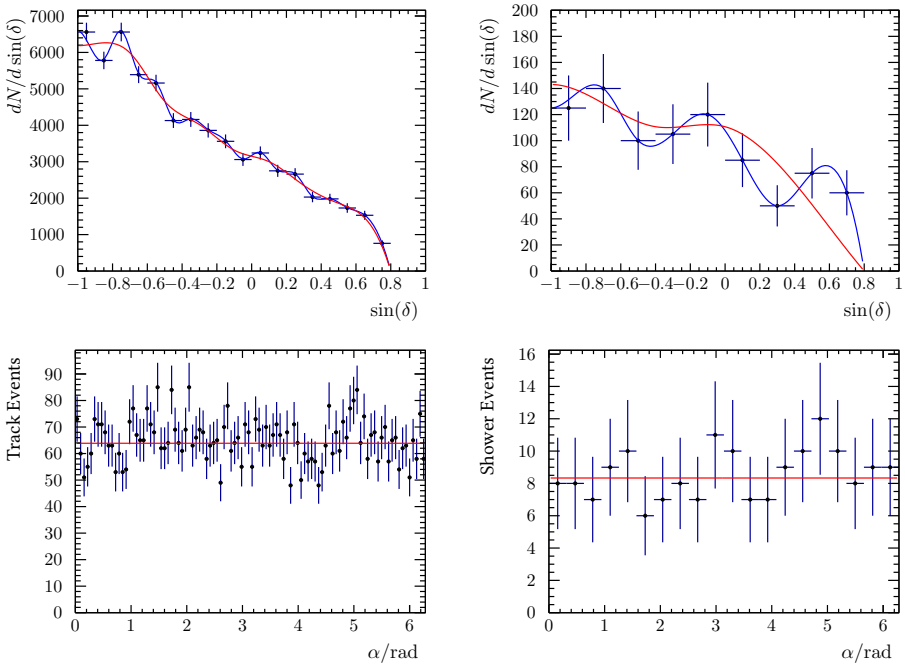

Figure 7.4: Event rate with respect to **Top:** declination and **Bottom:** right ascension for **Left:** Tracks and **Right:** Showers. The red and blue lines in the upper plots are different spline parametrisations. The red lines in the lower plots are constant fits to the data points.

on the ingredients indicates that each class has its own set thereof. The free parameters for the signal plus background hypothesis ($\mathscr{L}_{\mathrm{s+b}} = \mathscr{L}(x|H_{\mathrm{s+b}})$) are: the declination and right ascension of the source δ_{s} and α_{s} and the number of signal track and shower events $\mu^{\mathrm{tr}}_{\mathrm{sig}}$ and $\mu^{\mathrm{sh}}_{\mathrm{sig}}$.
Given an estimate of the number of signal tracks $\mu^{\mathrm{tr}}_{\mathrm{sig}}$, the ratio of the acceptances of the track and shower channels provides an expectation value for the number of signal shower events: $\hat{\mu}^{\mathrm{sh}}_{\mathrm{sig}} = \mu^{\mathrm{tr}}_{\mathrm{sig}} \cdot \mathcal{A}^{\mathrm{sh}}/\mathcal{A}^{\mathrm{tr}}$. The information of the expected ratio between the number of track and shower events is implemented with a Poisson probability function:

$$\mathscr{P}(\mu^{\mathrm{sh}}_{\mathrm{sig}}|\hat{\mu}^{\mathrm{sh}}_{\mathrm{sig}}) = \mathscr{P}(\mu^{\mathrm{sh}}_{\mathrm{sig}}|\mu^{\mathrm{tr}}_{\mathrm{sig}} \cdot \mathcal{A}^{\mathrm{sh}}(\delta_{\mathrm{s}})/\mathcal{A}^{\mathrm{tr}}(\delta_{\mathrm{s}})). \tag{7.9}$$

These parameters are estimated by maximising $\mathscr{L}_{\mathrm{s+b}}$[1], which is done by the TMinuit algorithm within the ROOT framework [74]. The background-only

[1] actually, by minimising $-\log\mathscr{L}_{\mathrm{s+b}}$

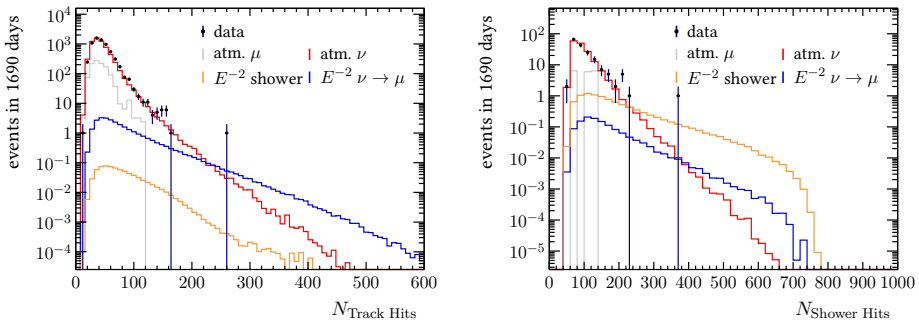

Figure 7.5: Distribution of the number of selected hits for **Left:** Tracks and **Right:** Showers. For the track channel, the blue histogram for cosmic muon neutrinos is considered signal and all the other coloured histograms are background. For the shower channel, the orange histogram is signal and the rest is considered background.

hypothesis ($\mathscr{L}_{\text{b}} = \mathscr{L}(x|H_{\text{b}})$) evaluates the likelihood at the same celestial position, δ_{s} and α_{s}, as the MLE for the signal hypothesis but sets the number of signal events to zero: $\mu_{\text{sig}}^{\text{tr}} = \mu_{\text{sig}}^{\text{sh}} = 0$.

Although the signal hypothesis is not a simple one, the Neyman-Pearson lemma is still reasonable justification for the construction of a test statistic analogue to the likelihood ratio:

$$\mathcal{Q} = \log \mathscr{L}_{\text{s+b}} - \log \mathscr{L}_{\text{b}}. \tag{7.10}$$

7.3 Pseudo Experiments

The PDF for the test statistic $\mathcal{Q}$ from equation (7.10) is not a priori known. Instead, it is determined from pseudo experiments (PEs). A PE is a randomly generated sky map. The number of generated background muon and shower events is equal to the respective number of selected events in data. They are distributed according to the declination-dependent parametrisation $\mathscr{B}^{\mathcal{S}}$ with the right ascension drawn uniformly. For each signal event, its class gets determined by random draw: A random number is thrown uniformly between 0 and 1. If the result is smaller than $\mathcal{A}^{\text{sh}}(\delta)/(\mathcal{A}^{\text{sh}}(\delta) + \mathcal{A}^{\text{tr}}(\delta))$, the event is set to be a shower. Otherwise, the event will be a track. The signal events are injected around a given source position in the sky. Their angular distance to this pseudo source is sampled from the PSF $\mathscr{F}^{\mathcal{S}}$ while the offset's polar angle around the source is again drawn uniformly. Every event gets

a number of selected hits assigned according to the corresponding PDF $\mathcal{N}_{\mathrm{sig}}^{\mathcal{S}}$ and $\mathcal{N}_{\mathrm{bkg}}^{\mathcal{S}}$, respectively. The PEs get classified according to the total number of injected signal events (integer steps from 0 to 30) and the location of the fake source (5° steps in δ_{s} between -90° to 40°). Given the rotational symmetry of the sky map, the right ascension will not get sampled and the pseudo source will always be at $\alpha_{\mathrm{s}} = 100^\circ$. For each class of PE, a large number of fake sky maps are generated. For each sky map, the MLE is determined and with it the test statistic $\mathcal{Q}$.

7.3.1 Absolute Pointing Accuracy

To find cosmic neutrino sources, the direction parameters in the detector reference frame, ϑ and ϕ, have to be translated into a coordinate system which is invariant under earth's rotation: the equatorial reference frame with declination and right-ascension, δ and α. The uncertainties on the detector's absolute position and orientation within this frame translate into a degradation of the ability to pinpoint an exact position in the sky. This uncertainty has been determined to be 0.13° in the horizontal and 0.06° in the vertical direction [81]. They are taken into account by offsetting all signal events of a PE by a $\Delta\vartheta$ and a $\Delta\phi$ which are drawn from two Gaussian distributions with the mentioned uncertainties as variances.

7.3.2 Angular Resolution Uncertainty

The angular resolutions of the muon and shower reconstruction algorithms have been determined from Monte Carlo simulations. An imprecise description of the detector performance in the Monte Carlo could lead to a better or worse performance of these reconstructions in the actual data. A different resolution has a direct impact on the detector's ability to identify a cluster of events as a possible point-source. To investigate this effect, the reconstruction has been performed on tampered Monte Carlo. For the tracks, the timing of the hits has been smeared to various degrees and a resulting $15\,\%$ uncertainty on the angular resolution has been determined [58]. The direction of the reconstructed shower depends less on the time of the hits and more on their recorded charge. For this reason, the charge of the hits has been smeared by a Gaussian with various widths and the reconstruction repeated using the modified pulse charges. The impact of the charge smearing on the angular shower resolution can be seen in figure 7.6. The estimated uncertainty on the charge calibration is $30\,\%$ [82]. This leads to an uncertainty on the angular resolution of $12\,\%$ in the shower channel.

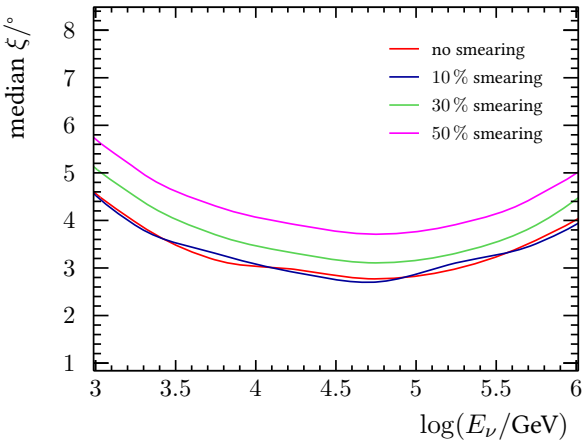

Figure 7.6: Impact of the uncertainty on the charge calibration on the angular resolution in the shower channel. The charges recorded by the PMTs have been smeared out to various degrees and the reconstruction performed again on the tampered hit information. A smearing of 10 % (blue line) makes practically no difference to the nominal angular resolution (red), a 30 % smearing (green) – the estimated uncertainty on the charge calibration – degrades the resolution by about 12 %. A smearing of 50 % (magenta) worsens the angular resolution by over 30 %.

7.3.3 Acceptance Uncertainty

The acceptance is used to translate a given neutrino flux into a number of expected signal events. Since the acceptance is merely a proportionality constant between those two quantities, an uncertainty on the acceptance has a direct impact on the mean number of events μ_s a flux would cause in the detector. The distribution of this mean signal can be expressed as:

$$\frac{dP(\mu_{\text{sig}})}{d\mathcal{Q}} = \sum_{N_{\text{sig}}} \frac{dP(N_{\text{sig}})}{d\mathcal{Q}} \cdot P(N_{\text{sig}}|\mu_{\text{sig}}), \tag{7.11}$$

with $P(N_{\text{sig}}|\mu_{\text{sig}})$ as the Poisson distribution and the sum going over all numbers of injected signal events in the PE generation. Due to the uncertainty in the acceptance, the real μ_{sig} is unknown but can be estimated as $\hat{\mu}$ with an uncertainty of $\sigma_{\hat{\mu}}$. Equation (7.11) can then be written as:

$$\frac{dP(\hat{\mu})}{d\mathcal{Q}} = \sum_{N_{\text{sig}}} \frac{dP(N_{\text{sig}})}{d\mathcal{Q}} \int P(N_{\text{sig}}|\mu_{\text{sig}})\, G(\mu_{\text{sig}}|\hat{\mu}, \sigma_{\hat{\mu}})\, d\mu_{\text{sig}}, \tag{7.12}$$

with $G(\mu_{\text{sig}}|\hat{\mu}, \sigma_{\hat{\mu}})$ as the Gauss distribution. Equation (7.12) is used with a $\sigma_{\hat{\mu}} = 15\,\%$ to calculate the sensitivity and limits. This value was obtained during a study of the impact of varying the PMT quantum efficiencies [58].

7.3.4 Background Uncertainty

To account for possible systematic uncertainties on the background, the distribution of the background rates in figure 7.4 were parametrised by two different spline functions, $R(\delta)$ and $B(\delta)$ (the red and blue lines in the top plots). The background event rate of the PEs for each declination gets determined by $\mathscr{B}(\delta) = B(\delta) + r \cdot (R(\delta) - B(\delta))$, with r being a random number drawn for each PE from a Gaussian normal distribution.

7.4 Discovery Potential and Sensitivity

If a detected signal has sufficient significance to claim a discovery, the flux of this signal can be directly calculated from the acceptance. Otherwise, upper limits on Φ_0 can be set. Before even looking for point-sources in the actual data, the experiment's capabilities to detect a signal can be estimated from the generated PEs. On the one hand, the *sensitivity*, the minimal flux that can safely be excluded, can be calculated and on the other hand, the minimum number of events needed for a discovery claim, the *discovery potential*, can be determined.
In case no discovery can be claimed from the observed data, an upper limit on the number of signal events μ_{sig} can be set as that $\hat{\mu}$ from equation (7.12) that can be excluded with a power of $(1 - \beta) = 90\,\%$, given a $\mathcal{Q}_{\text{crit}} = \mathcal{Q}_{\text{obs}}$. The sensitivity is defined as the median upper limit with a $\mathcal{Q}_{\text{crit}} = \widetilde{\mathcal{Q}}$, i.e. the median of $g(\mathcal{Q}|H_{\text{b}})$. In other words, the sensitivity is the signal flux that can be excluded with a power of at least 90 % in half of the background only PEs. To determine the potential for a discovery of a given significance α, first the corresponding $\mathcal{Q}_{\text{crit}}$ has to be found according to equation (7.2). This is done on an exponential fit of the tail of the test statistic distribution for the background-only-case (0 injected signal) as demonstrated in the left plots of figures 7.7 and 7.8. Subsequently, for every PE class of injected number of signal μ_{inj}, the fraction of the test statistic PDF that is less background compatible than $\mathcal{Q}_{\text{crit}}$ – the power of the measurement – is interpreted as the probability to reach the given significance α with μ_{inj} signal events. The discovery potential can for example be given as the probability to have a 3σ or 5σ claim as a function of the number of signal events, like in figure 8.1, or as

the declination-dependent flux needed to get a 5σ claim in $50\,\%$ of hypothetical, equivalent experiments, as shown in figure 8.2.

7.4.1 Full Sky Search

The full sky search aims to find a point-source anywhere in the visible sky. For this, subsets of potentially interesting events are selected as clusters with at least 3 tracks within a cone of 6° full opening angle or 1 shower and 1 track event within an angular distance of 10°. All of those clusters are used as seeds for the likelihood minimisation. The cluster with the highest significance is kept for the construction of the test statistic PDF. The left plot of figure 7.7 shows the distributions of the test statistic for various cases of injected signal at a source declination of $\delta_\mathrm{s} = -70^\circ$. The critical test statistic value for a significance of 5σ is at $\mathcal{Q}_{5\sigma} = 29.1$: If the measured data would produce a test statistic $\mathcal{Q}_\mathrm{obs} > \mathcal{Q}_{5\sigma}$ anywhere in the sky, a discovery of a neutrino point-source could be claimed. The right plot of this figure shows the fitted right ascension for the same pseudo experiments. The injected signal at a declination of $\alpha_\mathrm{s} = 100^\circ$ can be found in over $20\,\%$ of the cases when at least four signal events are present (blue histogram).

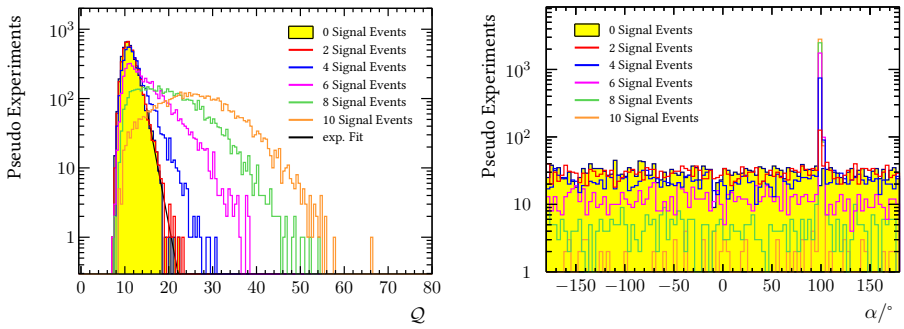

Figure 7.7: Left: Test statistic $\mathcal{Q}$ and **Right:** fitted right ascension for different numbers of injected signal events at $\delta_\mathrm{s} = -70^\circ$ and $\alpha_\mathrm{s} = 100^\circ$ for the full sky search. The background-only test statistic distribution is extrapolated by fitting the $5\,\%$ tail with an exponential. For better visibility in the left plot, the vertical axis has been cut off at 500. The peak of the background-only histogram extends well beyond a value of 3000.

7.4.2 Candidate List Search

Several known astronomical objects have been proposed to also be sources of neutrino emission. In the candidate list search the test statistic is evaluated for the position in the sky of several such objects. In this approach, the source declination and right-ascension are fixed and only the amount of signal is fitted. This method has the advantage of a reduced penalty on the significance due to the *look elsewhere effect*. Figure 7.8 on the left shows the distributions of the test statistic for the candidate list search. Comparing to the same plot for the full sky search (figure 7.7), one can see that the distributions for the various numbers of injected signal events separate much better from the background only case in this approach. On the right plot of figure 7.8 one can see that the number of injected signal events can be found back quite accurately. A number of candidates are not known astronomical sources visible with optical telescopes but muon tracks of the high energy starting events (HESE) analysis by IceCube [10]. Since those events have a non-negligible angular error estimate, the direction parameters are not fixed but fitted within a cone of twice their angular error estimate around the direction given by the IceCube tracks.
The list of candidates can be found in tables 8.1 for the astronomical objects and 8.2 for the IceCube tracks. The Galactic candidates are known gamma-ray sources in the 0.1 TeV to 100 TeV range that spend a large fraction of the time in the ANTARES field of view. Since extra-Galactic, high-energy gamma-rays can scatter or be absorbed before they reach earth, the energy threshold for extra-Galactic candidates was reduced to the GeV range.

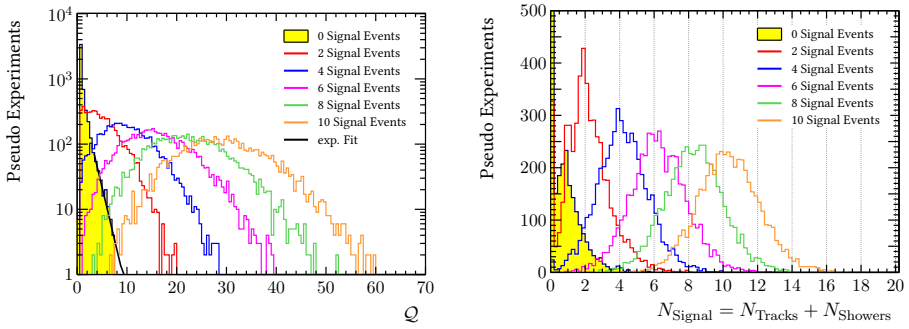

Figure 7.8: Left: Test statistic $\mathcal{Q}$ and **Right:** number of fitted signal events for different numbers of injected signal events at a declination of $\delta_s = -70°$ for the candidate list search. The background-only test statistic distribution is extrapolated by fitting the 5 % tail with an exponential.

7.4.3 Search around the Galactic Centre

A handful of the IceCube HESE events originate from a region around the Galactic Centre but could not be attributed to one common point-source. To investigate a possible effect in ANTARES a search similar to the full sky search has been performed. To increase the sensitivity, the search region has been restricted to an ellipsis around the Galactic Centre with semi axes of 30° in galactic longitude and 15° in galactic latitude. Signal has been injected along the galactic plane in 5° steps as is shown in figure 7.9.

Extended Sources

To account for the possibility that the high energy IceCube events near the Galactic Centre do not originate from one common point-source, extended sources have been investigated as well. A simple, two dimensional Gaussian $\mathcal{G}(\alpha_\mathrm{s}, \delta_\mathrm{s}, \sigma_\alpha, \sigma_\delta)$ with the central value at the Galactic Centre – $(\alpha_\mathrm{s}, \delta_\mathrm{s}) = (-93.58^\circ, -29.01^\circ)$ – and various extensions σ_α and σ_δ has been assumed as the neutrino emission profile. For every trial extension, new PEs have been generated with the signal distributed according to the extended morphology and fitted either assuming a point-source or the same extension that has been used to generate the signal. For this, the PSF $\mathscr{F}$ in the likelihood function in equation (7.8) has been convoluted with a source emission profile $\mathcal{G}$:

$$\mathscr{F}(\xi(\alpha_\mathrm{s}, \delta_\mathrm{s})) \rightarrow \iint \mathscr{F}(\xi(\alpha, \delta)) \times \mathcal{G}(\alpha_\mathrm{s}, \delta_\mathrm{s}, \sigma_\alpha, \sigma_\delta)\, d\alpha d\delta. \tag{7.13}$$

Extensions $\sigma_\alpha = \sigma_\delta$ between 0.5° and 5° have been investigated.

Alternative Energy Spectra

The IceCube collaboration reports with γ-values between 2.3 [83] and 2.6 [84] a different, softer energy spectrum than the traditionally assumed $E^{-2.0}$. The impact of different energy spectral indices on the ANTARES point source sensitivity has been investigated as well. For this, the flux parametrisation in equation (7.5) has been modified using spectral indices of $\gamma = 2.5$ and $\gamma = 3$ besides the $\gamma = 2$ that was used throughout the rest of this thesis. The sensitivities and limits were recalculated for all three spectral indices in the restricted region around the GC defined earlier.

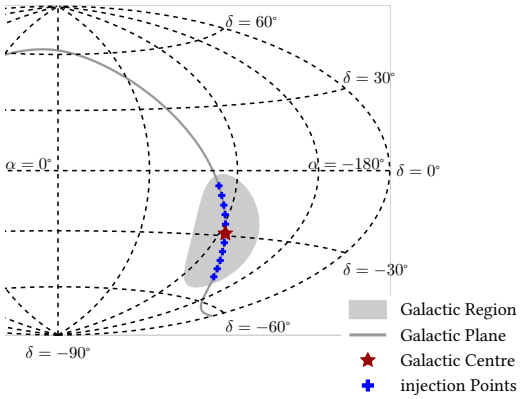

Figure 7.9: Sky map in equatorial coordinates: The grey area marks the region around the Galactic Centre that is considered in the search, the blue crosses show the injection points for the signal and the red star marks the Galactic Centre (which is itself an injection point). The grey line shows how the Galactic Plain lies in the equatorial sky.

Conclusion

A likelihood function has been implemented that not only takes the position of the events and their number of selected hits into account but also the expected ratio of track and shower events. Various search methods have been presented: A full sky search that looks for a significant excess in the event count anywhere in ANTARES's visibility; a search that restricts itself to the regions around a given list of source candidates; a search that investigates whether the Galactic Centre is not a point-like but in fact an extended source; and a search that probes neutrino flux models different from the traditional "E^{-2}" energy spectrum. It has been demonstrated on pseudo experiments that the likelihood function combined with the search methods is capable of recovering the position and intensity of injected signals of sufficient strength.

Chapter 8

Results

"And so faintly you came tapping, tapping at my chamber door,
That I scarce was sure I heard you"—here I opened wide the door;—
Darkness there and nothing more.
The Raven by Edgar Allan Poe

This chapter presents the sensitivities and discovery potentials of the various search strategies outlined in the last chapter. For every approach, its sensitivity – the capability to set upper limits in case no signal can be claimed – is presented here along with the most significant cluster of events. Upper limits on the number of detected signal and the signal flux are calculated.

8.1 Full Sky Search

The potential to claim a discovery of a neutrino source can be estimated as the signal strength needed to be able to find a cluster of events with sufficiently high significance. Figure 8.1 shows the probability that a given number of detected signal events from a source at a declination $\delta = -70^\circ$ produces a cluster that is significant enough to claim a discovery at a 3σ or 5σ level. The figures for different declinations look similar. To be able to claim a 5σ discovery in half of hypothetical, equivalent experiments anywhere in the visible sky, at least 11 signal events (tracks + showers) are needed. The declination dependency on the amount of signal needed to claim a 5σ discovery in half of the cases is shown in figure 8.2 for number of signal events (left) and flux (right). Due to the lower background rate at higher declinations[1], fewer signal events are needed to identify a significant cluster of events. In terms of flux, the discovery potential has a declination dependency analogue to the acceptance (cf. figure 7.2): It is flat for declinations below -40° where all directions

[1] caused by the requirement that the events were reconstructed as up-going, $\cos(\vartheta) > -0.1$, see chapter 6

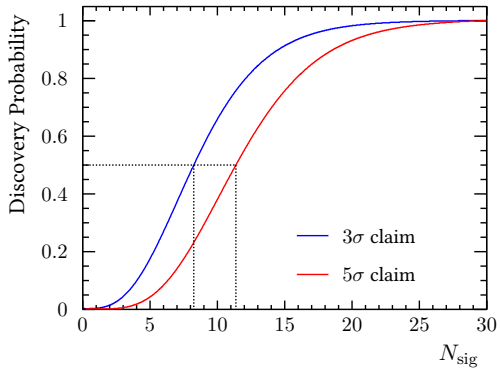

Figure 8.1: Probability for 3 and 5σ discoveries depending on the number of observed signal events at a declination of $\delta = -70^\circ$ for the full sky search. Blue for a 3σ and red for a 5σ claim.

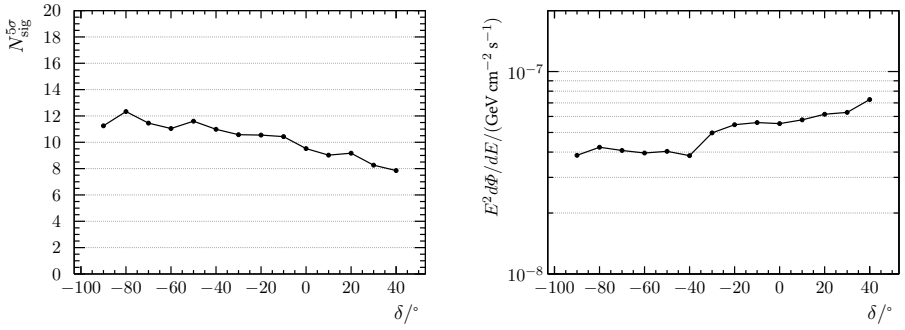

Figure 8.2: The discovery potential of the full sky search. **Left:** The number of signal events and **right:** the flux that is needed to claim a 5σ discovery in 50 % of hypothetical, equivalent experiments.

are constantly in the ANTARES field of view. For higher declinations, the discovery potential degrades until $\delta = 40^\circ$. Sources above this value are never in the field of view of the detector and cannot be detected.

The most significant cluster of events has a fitted position at right-ascension $\alpha = -47.0^\circ$ and declination $\delta = -65.0^\circ$ and is essentially the same as the one found in the last point-source analysis at $(\alpha, \delta) = (-46.8^\circ, -64.9^\circ)$ [76]. In this old search, only muon tracks found in the data set from early 2007 until the end of 2012 (one year less than in this analysis) were used. The distribution of events of this cluster can be seen in figure 8.3. It contains 17(7) tracks within $3(1)^\circ$ and 1 shower event within 10°. The number of signal events found by the likelihood function is $\mu_{\mathrm{sig}}^{\mathrm{tr}} + \mu_{\mathrm{sig}}^{\mathrm{sh}} = 7.3 + 0.0$. This cluster has post-trial significance of 4.2 % or 2.0σ with an upper limit on the neutrino flux coming from this source of $E^2 d\Phi/dE = 4.4 \times 10^{-8}\,\mathrm{GeV\,cm^{-2}\,s^{-1}}$.

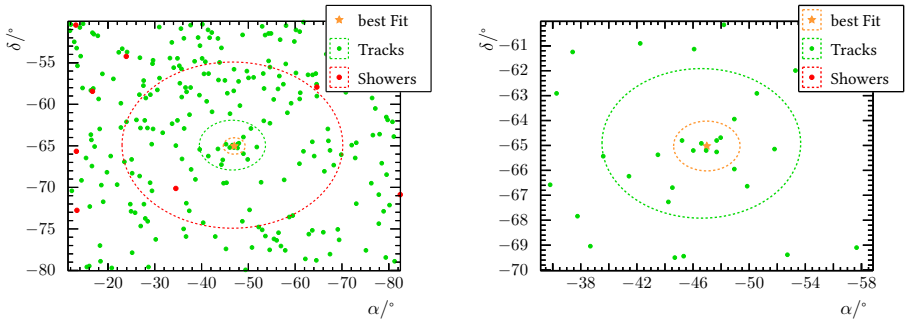

Figure 8.3: Most significant cluster in the full sky search. The fitted centre of the cluster is at $(\alpha, \delta) = (-47°, -65°)$. The significance of this cluster is $4.2\,\%$ or 2.0σ. Green dots represent the track and red dots the shower events. The events inside the dashed lines are considered in the likelihood function. The right plot is a zoom-in of the left.

From the signal strength of this most significant cluster, upper limits for the rest of the sky can be computed. These upper limits on number of signal events and flux are shown in figure 8.4 as dashed lines. This means that, with a confidence level of $90\,\%$, there are no cosmic neutrino point-sources with a flux above the dashed line anywhere in the visible sky. Otherwise, they would have produced a cluster with a significance higher than the highest one that has been found. Figure 8.4 also shows the declination-dependent sensitivity (solid lines) as the expected median upper limit of the full sky search. The declination-dependency of limit and sensitivity reflects the behaviour of discovery potential: For the number of signal events, it slowly drops for higher declinations and it follows the acceptance for the flux.

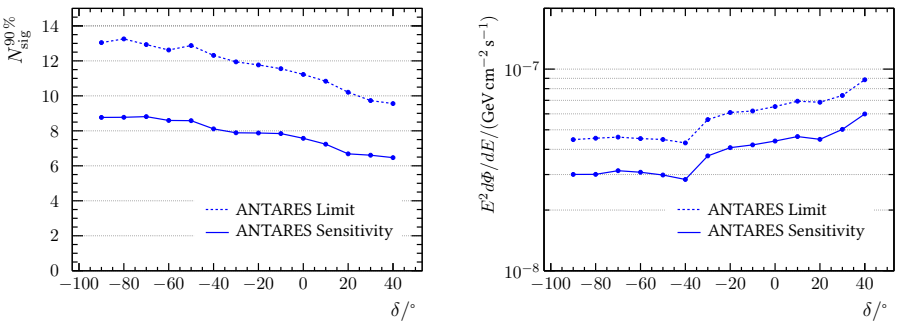

Figure 8.4: The upper limits (dashed lines) of the full sky search. The sensitivity (solid lines) as the median upper limit is shown as well. **Left:** The number of signal events and **right:** the flux that can be excluded with a power of at least $(1 - \beta) = 90\ \%$ in half of the background only cases.

Multi-spectral Follow-up

Archives of known astrophysical objects in a frequency range from radio to X-ray emission have been searched for nearby candidate sources close to the location of the most significant cluster. Two sources within 1° of the fitted cluster were identified: the AGN PKS 2047-655 at $(\alpha, \delta) = (-48.3^\circ, -65.6^\circ)$ [85] – a typical radio quasar – and the comparably small galaxy cluster AC103 at $(\alpha, \delta) = (-46.8^\circ, -64.9^\circ)$ [86].
In 2012, the H.E.S.S. collaboration conducted a follow-up investigation around the region of the ANTARES excess [87]. Since the most significant cluster at that time was practically at the same position as it is now, a comparison of the results is still valid. The H.E.S.S. detector observed the region around the ANTARES excess with an effective live time of 1.5 h. Using its default configuration, the four-telescope system was sensitive to cosmic rays of energies between 100 GeV and 100 TeV. A map of the number of very-high energy gamma-ray events exceeding the background expectation is shown in figure 8.5. The upper limits on the gamma-ray flux from the direction of the excess are shown in figure 8.6 (black dots). It is compared to the photon flux estimated from the observed upper limit on the neutrino flux [88] (red line). The H.E.S.S. data show no evidence of a gamma-ray source close to the ANTARES excess, in line with the cluster being a background fluctuation.

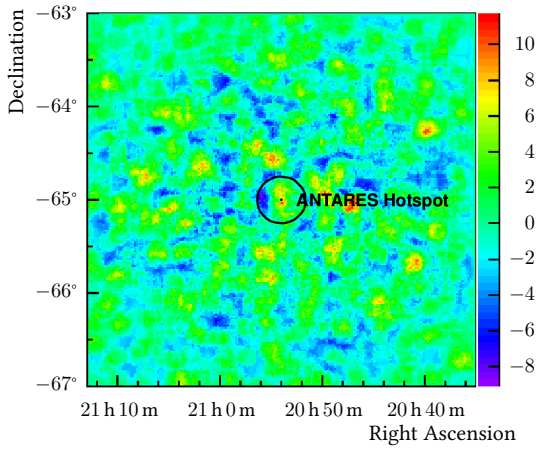

Figure 8.5: Number of very-high-energy gamma-ray events exceeding the background expectation from the H.E.S.S. observation as a follow-up to the ANTARES excess in 2012 [87].

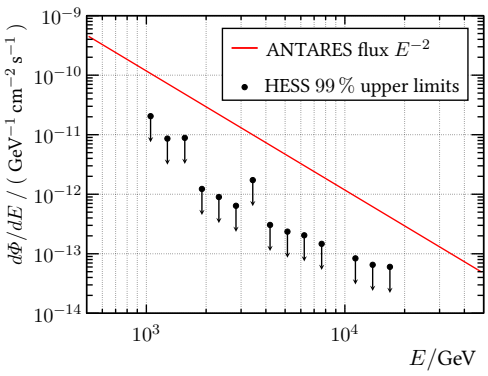

Figure 8.6: Upper limit at 99 % confidence level obtained by H.E.S.S. on the gamma-ray flux (black dots) from the region around the most significant cluster in the ANTARES full sky search. The limit is compared to the predicted neutrino flux from the fit assuming an E^{-2} spectrum (red line).
Limits reproduced from [87].

8.2 Candidate List

Investigating only at a number of pre-defined candidates increases the discovery power, since the location of the potential source is already known. Additionally, it is possible to put strong upper limits on the neutrino flux coming from any of the investigated candidates. For many of the investigated sources in the Galactic Centre region, those are the most stringent limits to date. The list of the candidates is shown in table 8.1 along with their equatorial coordinates, upper limits on the flux and on the number of signal events. For the five most significant candidates also the number of fitted signal events and the significance of the excess is given. The most signal-like cluster is around HESSJ0632+057 at $(\alpha, \delta) = (98.24°, 5.81°)$ with a significance of 20 % or 1.27σ. This cluster contains 35 track events within 10° and 3 showers within 15° around the source candidate. The distribution of events around this source is shown in figure 8.7.

Compared to IceCube [83], the ANTARES fixed-point search is more sensitive by a factor of about 2 for declinations below the Galactic Centre ($\delta_{GC} = -29°$). For higher declinations, the ANTARES sensitivity slowly degrades while the IceCube sensitivity improves by an order of magnitude for source candidates in the northern hemisphere ($\delta > 0°$). This sensitivity to fixed source candidates can be seen in figure 8.8.

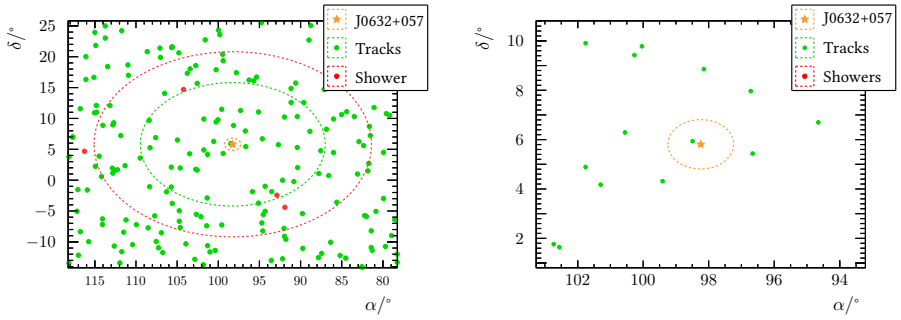

Figure 8.7: Most significant cluster in the candidate list. The candidate source HESSJ0632+057 is located at $(\alpha, \delta) = (98.24°, 5.81°)$ (orange star). The significance of this cluster is 20 % or 1.3σ. Green dots represent the track and red dots the shower events. The events inside the dashed lines are considered in the likelihood function. The right plot is a zoom-in of the left.

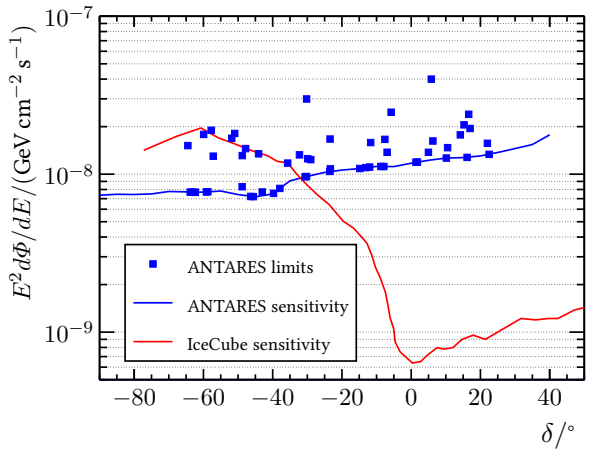

Figure 8.8: Upper limits at a 90 % confidence level on the signal flux from the investigated candidates assuming an E^{-2} spectrum (blue squares). The blue line shows the ANTARES sensitivity, the red line the sensitivity of the IceCube detector for comparison [83].

Additionally, 8 IceCube HESE track events have been investigated as possible point-sources. Due to their high energy they are likely to be created by a cosmic source and their apparent origin in the sky is in the ANTARES field of view. The coordinates of these events are shown in table 8.2 together with their angular uncertainty (given by IceCube) and upper limits on flux and number of signal events.
The HESE candidate with the largest excess in fitted signal is the IceCube track with ID 3 and $\mu_{\mathrm{sig}}^{\mathrm{tr}} + \mu_{\mathrm{sig}}^{\mathrm{sh}} = 5.3 + 0.6$. The fitted cluster is located at $(\alpha, \delta) = (130.66^\circ, -29.48^\circ)$ – which is with 3° about twice the angular error estimate away from the muon track candidate at $(\alpha, \delta) = (127.9^\circ, -31.2^\circ)$. The upper limits on the signal from this candidate are $\Phi_0^{90\,\%} = 4.3 \times 10^{-8}\,\mathrm{GeV\,cm^{-2}\,s^{-1}}$ and $N_{\mathrm{sig}}^{90\,\%} = 9.2$. The cluster is shown in figure 8.9.

Table 8.1: List of astrophysical objects used in the candidate list search. Presented are the object's coordinates in right ascension and declination and the 90 % upper limits on the flux normalisation factor Φ_0 and number of signal events N_{sig}. The candidates are sorted by the value of their test statistic. For the five most significant candidates, also the post-trial significance is given along with the fitted number of signal track and shower events.

Name	$\alpha/^\circ$	$\delta/^\circ$	$\frac{\Phi_0^{90\,\%}}{\mathrm{GeV\,cm^{-2}\,s^{-1}}}$	$N_{\mathrm{sig}}^{90\,\%}$	$\mu_{\mathrm{sig}}^{\mathrm{tr}}$	$\mu_{\mathrm{sig}}^{\mathrm{sh}}$	Significance
HESSJ0632+057	98.24	5.81	4.0e-8	6.6	1.2	0.0	1.27σ
HESSJ1741-302	-94.75	-30.2	3.0e-8	6.4	0.9	0.0	0.92σ
HESSJ1023-575	155.83	-57.76	1.9e-8	5.3	1.4	0.0	0.16σ
HESSJ1616-508	-116.03	-50.97	1.8e-8	5.2	0.0	1.1	0.10σ
ESO139-G12	-95.59	-59.94	1.8e-8	5.0	0.8	0.0	0.06σ

Name	$\alpha/^\circ$	$\delta/^\circ$	$\frac{\Phi_0^{90\,\%}}{\mathrm{GeV\,cm^{-2}\,s^{-1}}}$	$N_{\mathrm{sig}}^{90\,\%}$	Name	$\alpha/^\circ$	$\delta/^\circ$	$\frac{\Phi_0^{90\,\%}}{\mathrm{GeV\,cm^{-2}\,s^{-1}}}$	$N_{\mathrm{sig}}^{90\,\%}$
3C279	-165.95	-5.79	2.8e-8	4.5	VelaX	128.75	-45.6	7.2e-9	2.1
HESSJ1614-518	-116.42	-51.82	1.7e-8	4.9	RXJ0852.0-4622	133	-46.37	7.2e-9	2.1
PKS0235+164	39.66	16.61	2.4e-8	3.7	W28	-89.57	-23.34	1.1e-8	2.2
HESSJ1356-645	-151	-64.5	1.5e-8	4.2	QSO1730-130	-96.7	-13.1	1.1e-8	2.1
HESSJ1632-478	-111.96	-47.82	1.5e-8	4.2	RGBJ0152+017	28.17	1.79	1.2e-8	2.0
PKS0537-441	84.71	-44.08	1.4e-8	4.0	1ES1101-232	165.91	-23.49	1.0e-8	2.1
GX339-4	-104.3	-48.79	1.3e-8	3.8	RCW86	-139.32	-62.48	7.7e-9	2.1
VERJ0648+152	102.2	15.27	2.1e-8	3.2	RXJ1713.7-3946	-101.75	-39.75	7.6e-9	2.1
CirX-1	-129.83	-57.17	1.3e-8	3.6	MSH15-52	-131.47	-59.16	7.7e-9	2.2
PKS0454-234	74.27	-23.43	1.7e-8	3.4	HESSJ1912+101	-71.79	10.15	1.3e-8	2.0
Geminga	98.31	17.01	2.0e-8	3.0	HESSJ1503-582	-133.54	-58.74	7.7e-9	2.2
QSO2022-077	-53.6	-7.6	1.7e-8	3.1	PSRB1259-63	-164.3	-63.83	7.7e-9	2.2
PKS0727-11	112.58	-11.7	1.6e-8	3.0	PKS0426-380	67.17	-37.93	8.1e-9	2.1
W51C	-69.25	14.19	1.8e-8	2.8	HESSJ1303-631	-164.23	-63.2	7.7e-9	2.1
PKS0548-322	87.67	-32.27	1.3e-8	2.8	PKS2155-304	-30.28	-30.22	9.7e-9	2.1
PKS1454-354	-135.64	-35.67	1.2e-8	2.8	H2356-309	-0.22	-30.63	9.6e-9	2.1
MGROJ1908+06	-73.01	6.27	1.6e-8	2.7	PKS1406-076	-147.8	-7.9	1.1e-8	2.1
PKS1622-297	-113.5	-29.9	1.3e-8	2.7	3C454.3	-16.5	16.15	1.3e-8	2.0
Galactic Centre	-93.58	-29.01	1.2e-8	2.6	HESSJ1507-622	-133.28	-62.34	7.7e-9	2.1
HESSJ1837-069	-80.59	-6.95	1.4e-8	2.5	1ES0347-121	57.35	-11.99	1.1e-8	2.1
PKS2005-489	-57.63	-48.82	8.3e-9	2.4	W44	-75.96	1.38	1.2e-8	2.0
CentaurusA	-158.64	-43.02	7.7e-9	2.3	IC443	94.21	22.51	1.3e-8	1.9
Crab	83.63	22.01	1.6e-8	2.3	LS5039	-83.44	-14.83	1.1e-8	2.1
PKS1502+106	-133.9	10.52	1.5e-8	2.3	HESSJ1834-087	-81.31	-8.76	1.1e-8	2.1
SS433	-72.04	4.98	1.4e-8	2.3					

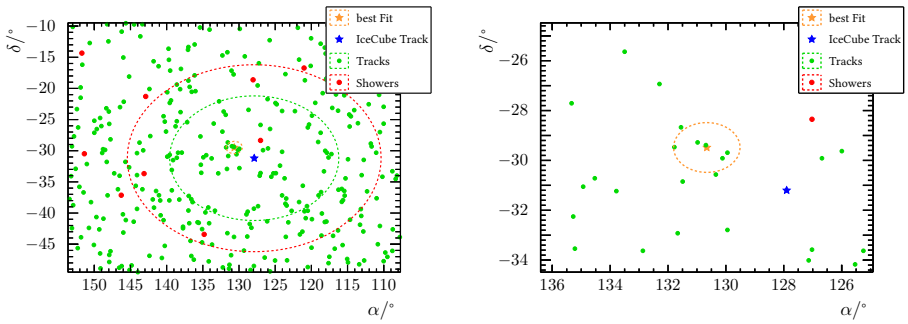

Figure 8.9: Most significant cluster around the investigated IceCube track candidates. The candidate is located at $(\alpha, \delta) = (127.9°, -31.2°)$ (blue star); the fitted position at $(130.66°, -29.48°)$ (orange star). The angular distance between the candidate and the best fit is 3°. Green dots represent the track and red dots the shower events. The events inside the dashed lines are considered in the likelihood function. The orange dashed line represents the one-degree region around the best fit. The right plot is a zoom-in of the left.

Table 8.2: The 8 muon track candidates from the IceCube point source search [10] that are in the field of view of the ANTARES detector. Presented are the equatorial coordinates, the event's angular error estimate β_{IC} and the upper limits on flux and signal events.

IceCube ID	$\alpha/°$	$\delta/°$	$\beta_{\mathrm{IC}}/°$	$\frac{\Phi_0^{90\,\%}}{\mathrm{GeV\,cm^{-2}\,s^{-1}}}$	$N_{\mathrm{sig}}^{90\,\%}$
3	127.9	-31.2	1.4	4.3e-8	9.2
5	110.6	-0.4	1.2	3.3e-8	5.7
8	182.4	-21.2	1.3	1.5e-8	3.1
13	67.9	40.3	1.2	2.3e-8	2.5
18	-14.4	24.8	1.3	5.2e-8	7.3
23	-151.3	-13.2	1.9	1.8e-8	3.4
28	164.8	-71.5	1.3	1.7e-8	4.7
37	167.3	20.7	1.2	1.7e-8	2.6

8.3 The Galactic Centre

The region around Galactic Centre (GC) contains many interesting astrophysical objects; most notably for sure the super-massive black hole Sagittarius A* at the GC itself. Additionally, a number of the IceCube HESE shower events seemingly originate from a region close to the GC. Searching for astrophysical sources in this region is about $50\,\%$ more sensitive compared to the full sky search. Due to the smaller search area, it is less probable for background events to randomly cluster together, mimicking the signature of a point source.
The most significant cluster found in this restricted region is located at $(\alpha, \delta) = (-110.0°, -50.8°)$ with a significance of $74\,\%$ or 0.33σ. The fitted number of signal events are 2.9 tracks plus 1.4 showers. The distribution of this cluster's events can be seen in figure 8.10. The declination-dependent limit and sensitivity of such a restricted point-source search is shown in figure 8.11 as the number of signal events (left) and the flux (right) that can be excluded with a power of $(1 - \beta) = 90\,\%$.

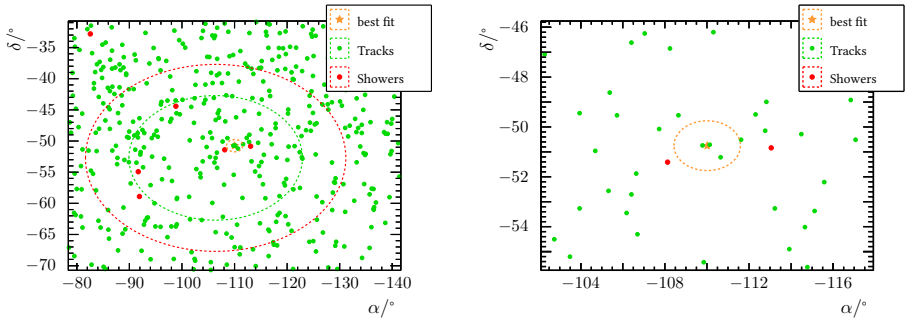

Figure 8.10: Most significant cluster in the region around the Galactic Centre. Green dots represent the track and red dots the shower events. The best fit is represented by the orange star at $(\alpha, \delta) = (-110.0°, -50.8°)$. The orange dashed line represents the one-degree region around the best fit. The events inside the red and green dashed lines are considered in the likelihood function. The right plot is a zoom-in of the left.

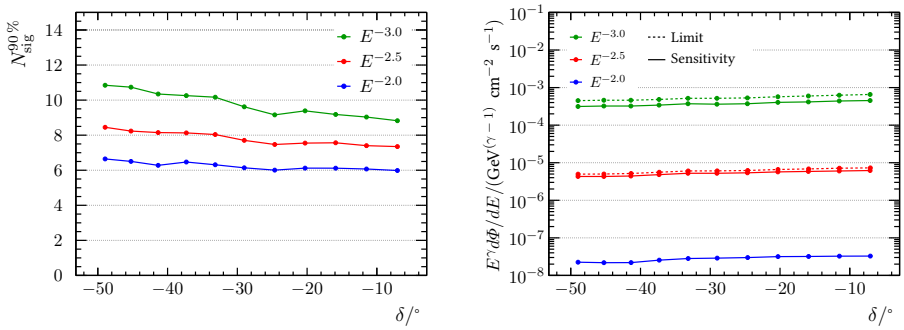

Figure 8.11: Upper limits (dashed) and sensitivity (solid) of a point-source search restricted to the region around the Galactic Centre at $(\alpha, \delta) = (-93.58°, -29.01°)$ assuming different spectral indices for the neutrino flux. **Left:** The number of signal events and **right:** the flux that can be excluded with a power of at least $(1-\beta) = 90\,\%$ in half of the background only cases.

Energy Spectra

A fit of the spectral index to the astrophysical neutrino signal detected by IceCube revealed with $\gamma = 2.3$ [83] and $\gamma = 2.6$ [84] a slightly softer spectrum than the usually used E^{-2} spectrum. For this reason, spectral indices other than the traditional $\gamma = 2$ have been investigated as well. The upper limits together with the sensitivities for these energy spectra are shown in figure 8.11. The sensitivity decreases for larger indices. A softer energy spectrum of cosmic neutrinos is less distinguishable from the also soft spectrum of atmospheric neutrinos. The big loss in sensitivity to the neutrino flux by several orders of magnitude – compared to the loss in sensitivity of only a few number of signal events – is an artefact from the flux normalisation at 1 GeV. For larger values of the spectral index γ, fewer neutrinos are emitted by the source within an energy range to which ANTARES is sensitive. The flux at the normalisation point that is necessary for a significant detection is therefore much larger.

Galactic Centre as an extended Source

Super-massive black holes are strong candidates to be accelerators of very-high energy cosmic rays and therefore for cosmic neutrino production. Furthermore, a handful of high-energy shower events have been reconstructed by the IceCube detector to have originated from a direction close to the GC but could not be attributed to a point-like source. For this reason, Sagittarius A* located at the GC has been investigated as an extended source with extensions between 0.5° and 5°. The cluster of events around the GC reconstructed by ANTARES is shown in figure 8.12. The sensitivity and upper limits for the assumption of different source extensions of the GC can be seen in figure 8.13. The sensitivity degrades with increasing extension but an improvement of up to a factor of 2 can be achieved by fitting the signal with the proper extension. The largest excess above the sensitivity was found at an extension of 1° with a pre-trial significance of 1.4σ. Upper limits on the flux and the number of signal events from the Galactic Centre assuming different extensions are presented in table 8.3.

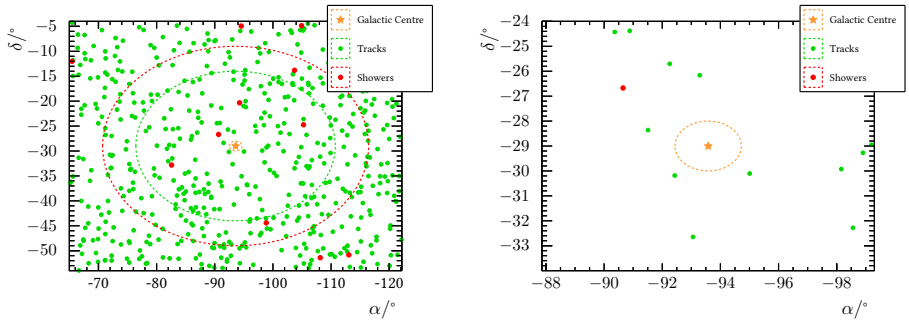

Figure 8.12: The Cluster of Events at the Galactic Centre. Green dots represent the track and red dots the shower events. The Galactic Centre is represented by the orange star at $(\alpha, \delta) = (-110.0^\circ, -50.8^\circ)$. The orange dashed line represents the one-degree region around the Galactic Centre. The events inside the red and green dashed lines are considered in the likelihood function. The right plot is a zoom-in of the left.

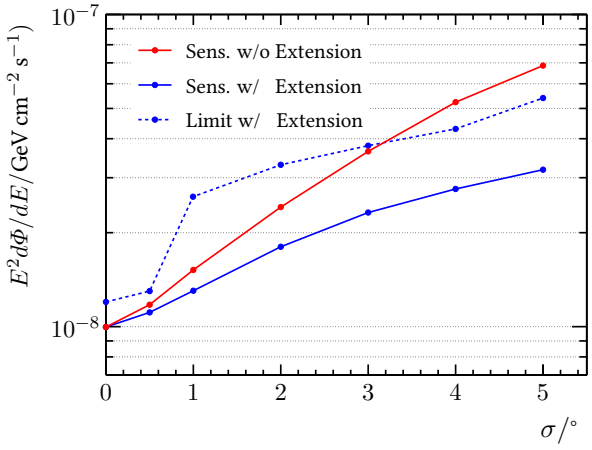

Figure 8.13: Sensitivity and upper limits of a search for an extended source at the Galactic Centre at $(\alpha, \delta) = (-93.58^\circ, -29.01^\circ)$ assuming different extensions. Red: The sensitivity for an extended source assuming a point-source. Blue: The sensitivity (solid line) and upper limit (dashed line) for an extended source using the correct extension in the likelihood function. At the highest investigated extension, a gain in sensitivity of a factor of $\gtrsim 2$ can be achieved.

Table 8.3: Upper limits on the signal flux and the number of signal events for different extensions of the Galactic Centre.

Extension	$\frac{\Phi_0^{90\,\%}}{\mathrm{GeV\,cm^{-2}\,s^{-1}}}$	$N_{\mathrm{sig}}^{90\,\%}$	μ_{tr}	μ_{sh}
0°	1.2e-08	2.61	0.0	0.0
0.5°	1.3e-08	2.83	0.0	0.0
1°	2.6e-08	5.43	0.6	0.0
2°	3.3e-08	7.09	0.7	0.0
3°	3.8e-08	8.08	0.6	0.0
4°	4.3e-08	9.21	1.5	0.3
5°	5.4e-08	11.6	2.5	0.7

Conclusion and Outlook

Various searches for cosmic neutrino sources using combined information from the track and shower channels have been performed. Even though the ANTARES sensitivity in the lower hemisphere is comparable or even better than the one presented by IceCube, no significant evidence of cosmic neutrino sources could be found. The IceCube cluster near the Galactic Centre could not be attributed to a point-source nor to an extended source at the Galactic Centre itself. Nevertheless, stringent limits were set for a flux coming from anywhere in the visible sky and even stricter limits for the flux from a number of known candidates.
The most significant cluster in the full sky search has been located at $(\alpha, \delta) = (-47.0^\circ, -65.0^\circ)$ with a significance of $4.2\,\%$ or 2.0σ. This is a confirmation of the most significant cluster found by the last point-source analysis at $(\alpha, \delta) = (-46.8^\circ, -64.9^\circ)$.
The most significant source candidate is HESSJ0632+057 – located at $(\alpha, \delta) = (98.24^\circ, 5.81^\circ)$ – with a significance of 1.3σ. Also this most significant candidate is the same as in the last analysis. The upper limits on the signal from this candidate are $E^2 d\Phi/dE = 4.3 \times 10^{-8}\,\mathrm{GeV\,cm^{-2}\,s^{-1}}$ and $N_{\mathrm{sig}}^{90\,\%} = 9.2$. Upper limits on the neutrino flux from 54 astrophysical candidates and around 8 IceCube muon tracks have been presented. They are – at the time of writing – for many sources the most stringent.
The most significant cluster of events close to the Galactic Centre is located at $(\alpha, \delta) = (-110.0^\circ, -50.8^\circ)$ with a significance of 0.33σ.
In addition to the search for point-like sources, the Galactic Centre as a possible extended source has been investigated. Upper limits for the flux and number of events assuming a Gaussian morphology with different extensions have been presented. The largest excess of the upper limit over the sensitivity was observed at an extension of 1° with a pre-trial significance of 1.4σ.

To further improve the sensitivity of the point-source search, the ANTARES track+shower dataset can be combined with the data from the IceCube detector. A combined muon-only ANTARES/IceCube analysis has already been performed recently [89].
The KM3NeT detector – currently under construction – will combine a cubic kilometre size with a high visibility towards the Galactic Centre due to its advantageous location. It is expected that it will be able to make definite statements about a neutrino flux from several cosmic candidates within a few years.

Summary

Astronomy is one of the oldest sciences. Since pre-historic times, civilisations looked at the stars and tried to explain what they saw. At first with with nothing more than the naked eye, later aided by telescopes. All over the planet, devices have been constructed to guide them on their endeavour to understand the dynamics of the heavens; from primitive stone constructions like Stonehenge to modern telescopes mounted on satellites. There is a wide array of messengers that can be used to study distant objects; from photons in form of radio waves, visible light, X- and gamma-rays to cosmic rays, neutrinos and the just recently directly observed gravitational waves. Astronomy with photons is very well established, has advanced to high-precision measurements and is the source of many spectacular images. Due to their electric charge, cosmic rays get deflected by galactic and intergalactic magnetic fields, effectively randomising their arrival directions on the Earth. With increasing energy the deflection decreases but even at the highest detected energies it may still be several degrees. The highest-energy particles ever detected where cosmic rays. However, at these energies the cosmic ray flux is so low that enormous collecting areas are necessary. Figure S.1 shows the cosmic ray energy spectrum measured by various experiments. The spectrum can be described by a power-law with two characteristic breaking points: the "knee" at $E \approx 3 \times 10^{15}$ GeV and the "ankle" at $E \approx 10^{19}$ GeV. The cause of these features and the mechanisms that allow acceleration up to the observed energies are topics of active research. To date, no astrophysical object could be identified as the source of any cosmic rays that have been detected so far.
Several models propose a production of neutrinos along the acceleration of charged nuclei, usually through nucleon-photon interactions: $p+\gamma \rightarrow \Delta^+ \rightarrow \pi^+ + n$, or nucleon-nucleon interactions: $p+p \rightarrow p+n+\pi^+$, and the subsequent pion decays. Popular candidates for these accelerations are supernova remnants, gamma-ray bursts and the super-massive black holes at the centre of many galaxies. The neutrino flux produced in these interactions is expected to follow the energy spectrum of the cosmic rays: $\frac{d\Phi_\nu}{dE} \sim E^{-2}$. In contrast to cosmic rays, neutrinos are not deflected by magnetic fields and point straight back to their source. The detection of high-energy neutrinos would also be a telltale sign for hadronic cosmic ray accelerations.

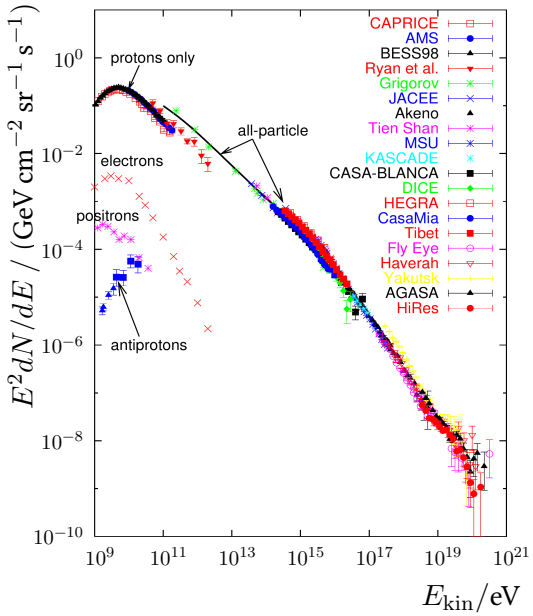

Figure S.1: The energy spectrum of various kinds of particles constituting cosmic rays. The spectrum follows a power law with different spectral indices depending on the energy. The breaking points are called the knee at $E \approx 3 \times 10^{15}$ eV and the ankle at $E \approx 10^{19}$ eV. Picture taken from [15].

The ANTARES neutrino telescope is located in the deep Mediterranean Sea, 40 km off the coast of Toulon, France. It consists of 885 optical modules arranged in a three-dimensional grid encompassing a volume of $0.01\,\mathrm{km}^3$. ANTARES was built to detect high-energy neutrinos and to associate them to an astrophysical source. The search for such sources is one of the main topics described in this manuscript. To link neutrinos to an astrophysical source, their directions have to be reconstructed from their signal in the detector. Neutrinos interact only through the weak interaction and cannot be detected directly. Instead, they can exchange W and Z bosons with the atoms of the water and rock surrounding the detector. Many of the electromagnetically charged particles created in these interactions are produced with sufficient energy to be faster than the phase velocity of light in water. In this case, the polarisations of the water molecules caused by these charged particles relax coherently and radiate energy in form of Cherenkov photons. These photons get picked up by the detector's optical modules and their signal is sent to the shore station where is stored for later analysis. The algorithm used to reconstruct the parent neutrino's direction depends on the particles that emerge in the initial interaction. In case a muon is created, the potentially kilometres-long muon track is reconstructed by a likelihood maximisation using the timing of the photon hits as input. This reconstruction algorithm for muon tracks achieves a median angular resolution of $0.4°$. If the neutrino

turns into an electron or – in case of a Z boson exchange – doesn't change its type at all, a shower of particles emerges that deposits all of its energy within a few metres as Cherenkov light. The development of a reconstruction algorithm for such showers was the second task of this PhD project. Since the extension of the shower is small compared to the size of the detector, the time profile appears isotropic for modules further away and is not useful for the reconstruction. Instead, the implemented maximum likelihood method uses the amount of photons detected by the various optical modules. This number depends on the distance between shower and optical module and the angle between the neutrino direction and the direction of the emitted photon. With this method, a median angular resolution of about 3° was achieved in the most relevant energy range of $10^3 \leq E_\nu/\mathrm{GeV} \leq 10^6$. Figure S.2 shows the angular resolution as a function of the neutrino energy.

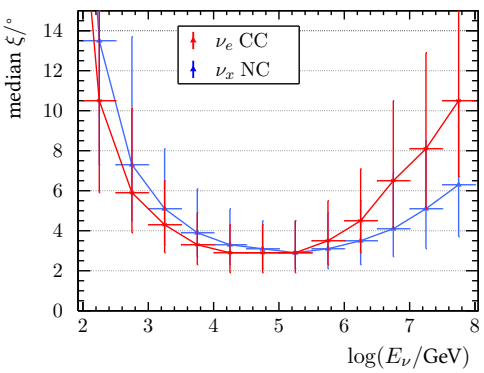

Figure S.2: The median of the angle ξ between the directions of the reconstructed shower and the Monte Carlo neutrino; red for electromagnetic showers, blue for hadronic showers. Some loose containment criteria have been applied to select events close to the detector: $\rho_{\mathrm{Shower}} < 300\,\mathrm{m}$ and $|z_{\mathrm{Shower}}| < 250\,\mathrm{m}$.

Two of the main backgrounds in a search for astrophysical neutrino sources are muons and neutrinos that were generated by cosmic rays that collide with the Earth's atmosphere. Several event-by-event selection criteria have been developed to suppress these backgrounds. Since the Earth effectively shields off atmospheric muons generated on the other side of the planet but is transparent to cosmic neutrinos, one of the selection criteria is to only use events that have been reconstructed as up-going. Data from early 2007 until the end of 2013 was analysed, corresponding to a live time of 1690.5 days. From these data, a total of 6490 muon tracks and 172 shower events were selected.
The distinguishing feature between atmospheric neutrinos and those from a cosmic source is that atmospheric neutrinos are distributed isotropically over the full sky while all neutrinos from one cosmic source come from the same direction. The only limitation here is the angular resolution of the used reconstruction algorithms which causes the reconstructed events to scatter around

the true direction of the neutrinos. To identify a neutrino source is to find such clusters of events among the background of atmospheric neutrinos. This search was performed with the method of maximising the ratio between the likelihoods of the hypothesis that the dataset consists solely of background events and the hypothesis that additionally some signal events are present. The likelihood considers the resolution of the reconstructed events in form of the point spread function – estimated from Monte Carlo simulations – and the distribution of the background events across the sky – taken directly from the observed data. Atmospheric neutrinos have a much softer energy spectrum than the E^{-2} spectrum assumed for neutrinos generated by astrophysical sources. For this reason, the number of hits selected by the reconstruction algorithm for each event is used as an energy estimator for the parent neutrino to further distinguish between cosmic signal and atmospheric background.

The sensitivity of this method was studied using pseudo experiments. Here, a large number of sky maps was generated to mimic the distribution of events we see in data. On top of this, a varying number of signal events has been injected according to the assumed E^{-2} spectrum. The intensity of the source (i.e. the number of detected signal events) and its location in the sky is determined by the maximum likelihood estimator, which is the hypothesis that maximises the likelihood function. The search for a signal in the data has

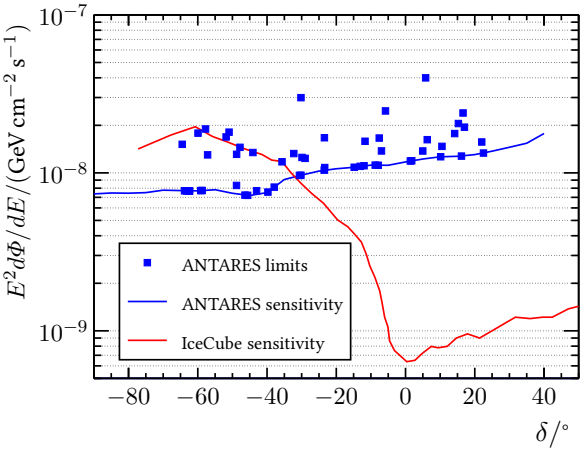

Figure S.3: Upper limits at a 90 % confidence level on the signal flux from the investigated candidates assuming an E^{-2} spectrum (blue squares). The blue line shows the ANTARES sensitivity, the red line the sensitivity of the IceCube detector for comparison [83].

been performed with three different approaches. In the full sky search, the whole sky is scanned for a point-source manifested as a cluster of events. In the candidate list search, the presence of a signal was tested for a pre-defined list of 54 directions of known astrophysical objects. Similar to the full sky search, the Galactic Centre search looks for a signal cluster anywhere in a region around the Galactic Centre. This region is an ellipsis with semi-axes of 30° and 15°. In addition to the point-source searches, the Galactic Centre has been tested as an extended source with widths between 0.5° and 5°.
No significant signal could be found anywhere in the visible sky. The most significant cluster in the full sky search has been located at $(\alpha, \delta) = (-47.0^\circ, -65.0^\circ)$ with a significance of $4.2\,\%$ and is essentially the same cluster as in the previous analysis. The source candidate with the most significant cluster around it is HESSJ0632+057, located at $(\alpha, \delta) = (98.24^\circ, 5.81^\circ)$, with an upper limit on the signal flux of $\Phi_0^{90\,\%} = 4.3 \times 10^{-8}$. Also this most significant candidate is the same as in the last analysis. On all other candidates limits could be set as well; which are the most stringent for many astrophysical objects in the lower hemisphere. These limits and the ANTARES sensitivity are shown in figure S.3 and compared to the IceCube sensitivity. The Galactic Centre could neither be identified as a point-source nor as an extended source. The biggest excess of the upper limit over the sensitivity was observed at an assumed Galactic Centre extension of 1° with a pre-trial significance of 1.4σ.

Samenvatting

Astronomie is een van de oudste wetenschappen. Sinds de prehistorie hebben beschavingen naar de sterren getuurd en geprobeerd te verklaren wat ze zagen. Aanvankelijk met niets dan het blote oog, maar later met behulp van telescopen. Wereldwijd zijn er apparaten gebouwd om hen bij te staan in hun poging de dynamiek van de hemelen te doorgronden; van primitieve stenen constructies als Stonehenge tot moderne satelliettelescopen. Er is een plethora aan boodschappers waarmee verweggelegen objecten bestudeerd kunnen worden; van fotonen in de vorm van radiogolven, zichtbaar licht, gamma- en röntgenstraling tot kosmische straling, neutrino's en de onlangs geobserveerde gravitatiegolven. Astronomie met fotonen kent een lange geschiedenis, maakt zeer precieze metingen mogelijk en levert spectaculaire afbeeldingen op. Kosmische stralen worden vanwege hun elektrische lading afgebogen door galactische en intergalactische magnetische velden, waardoor hun aankomstrichting op Aarde verstoord wordt. Naarmate de energie toeneemt neemt de afbuiging af, maar zelfs bij de hoogste energieën gaat het nog steeds om enkele graden. De hoogst-energetische deeltjes die ooit gedecteerd zijn, zijn kosmische stralen. Echter, bij deze energieën is de kosmische stralingsflux zo laag dat enorme detectie-opervlakken noodzakelijk worden. Afbeelding S.1 toont het door verscheidene experimenten gemeten energiespectrum van kosmische straling. Het kan benaderd worden door een machtswet met twee karakteristieke knikpunten: de 'knie' bij $E \approx 3 \times 10^{15}$ eV en de 'enkel' bij $E \approx 10^{19}$ eV. De oorzaak van deze knikpunten en de onderliggende mechanismen die versnelling to de geobserveerde energieën mogelijk maken worden nog steeds onderzocht. Tot nu toe is er geen enkel astrofysisch object geïdentificeerd als mogelijke bron van de gedecteerde kosmische straling. Verscheide modellen voorspellen dat neutrinoproductie plaatsvindt op plekken waar geladen atoomkernen versneld worden, meestal door de interactie van kerndeeljes met fotonen ($p + \gamma \rightarrow \Delta^+ \rightarrow \pi^+ + n$), of met andere kerndeeltjes ($p + p \rightarrow p + n + \pi^+$), en het verval van de daarbij ontstane pionen. Supernovaresten, gammaflitsen en de superzware zwarte gaten in veel sterrenstelsels zijn veelgenoemde kandidaten voor de versnelling van deze atoomkernen. De neutrinoflux van zulke interacties volgt naar verwachting het energiespectrum van de kosmische straling: $\frac{d\Phi_\nu}{dE} \sim E^{-2}$. In tegenstelling

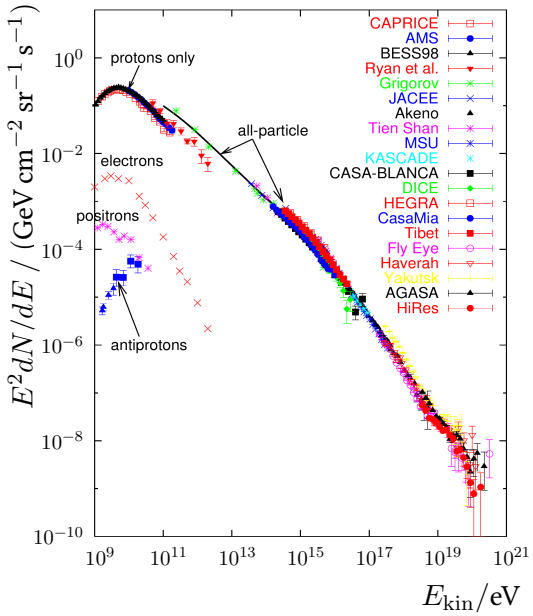

Afbeelding S.1: Het energiespectrum van verscheidene soorten kosmische stralingsdeeltjes. Het spectrum volgt een machtswet met verschillende spectrale indices afhankelijk van de energie. De knikpunten staan bekend als de 'knie' bij $E \approx 3 \times 10^{15}$ eV en de 'enkel' bij $E \approx 10^{19}$ eV. Afbeelding van [15].

tot kosmische straling worden neutrino's niet afgebogen door magnetische velden en wijst hun richting direct terug naar hun bron. De detectie van hoog-energetische neutrino's zou ook een kenmerkende eigenschap zijn van hadronische versnellingsmechanismen als bron van kosmische straling.
De ANTARES neutrinotelescoop bevindt zich diep in de Middellandse Zee, 40 km buiten de kust van Toulon in Frankrijk. Hij bestaat uit 885 optische modules, gerangschikt in een driedimensionaal rooster dat een volume beslaat van 0.01 km^3. ANTARES werd gebouwd om hoog-energetische neutrino's te detecteren en ze te kunnen correleren aan een astrofysische bron. De zoektocht naar zulke bronnen is één van de hoofdonderwerpen van dit manuscript. Om neutrino's te kunnen koppelen aan een astrofysische bron moet hun richting gereconstrueerd worden uit het signaal dat ze veroorzaken in de detector. Neutrino's interageren alleen door middel van de zwakke koppeling en kunnen daardoor alleen indirect gedetecteerd worden wanneer ze een W- of Z-boson uitwisselen met de atomen in het omringende water en gesteente. Veel van de elektromagnetisch geladen deeltjes die in deze interacties geproduceerd worden hebben zoveel energie dat hun snelheid hoger is dan de fasesnelheid van licht in water. In dat geval depolariseren de door de geladen deeltjes gepolariseerde watermoleculen op een coherente manier, waarbij energie uitgestraald wordt in de vorm van Cherenkov-fotonen. Deze fotonen worden opgevangen door de optische modules van de detector en

het signaal wordt verzonden naar het kuststation, waar de data opgeslagen worden voor latere nalyse. Het algoritme waarmee de neutrinorichting gereconstrueerd wordt hangt af van de deeltjes die ontstaan in de primaire interactie. Wanneer er een muon geproduceerd wordt, wordt het - mogelijk kilometers lange - spoor ('track') van het muon gereconstrueerd door middel van een likelihood maximalisatie op basis van de timing van de *hits*. Dit reconstructie-algoritme voor tracks bereikt een hoekresolutie van 0.4° (mediaan van de verdeling). Als het neutrino daarentegen verandert in een elektron of – in het geval van de uitwisseling van een Z-boson – helemaal niet verandert, onstaat er een deeltjesdouche ('shower') die al zijn energie binnen enkele meters afgeeft in de vorm van Cherenkovstraling. Het ontwikkelen van een reconstructie-algoritme voor zulke showers was het tweede onderdeel van dit PhD project. Aangezien de fysieke afmeting van de showers klein is vergeleken met de detector, lijkt het tijdsprofiel isotroop voor verweggelegen modules en is daarom niet nuttig voor de reconstructie. In plaats daarvan is de gebruikte *maximum-likelihood* methode gebaseerd op het aantal fotonen dat gedetecteerd wordt door de verscheidene optische modules. Dit aantal hangt af van de afstand tussen de shower en de optische module en de hoek tussen de neutrinorichting en de richting van het uitgezonden foton. Met deze methode kon een hoekresolutie van ongeveer 3° (mediaan van de verdeling) bereikt worden in het meest relevante energiebereik van $10^3 \leq E_\nu/\mathrm{GeV} \leq 10^6$. Afbeelding S.2 toont de hoekresolutie als functie van de neutrino-energie.

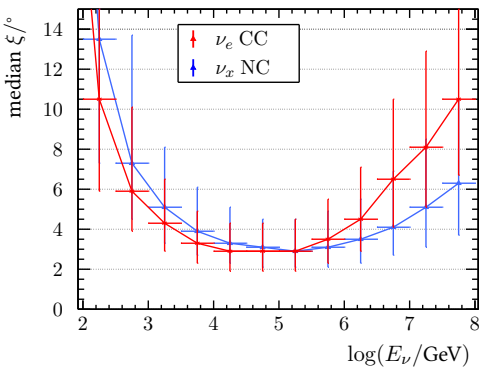

Afbeelding S.2: The median van de verdeling van de hoek ξ tussen de gereconstructueerde *shower* en het Monte Carlo neutrino: rood voor elektromagnetische *showers*, blauw voor hadronische *showers*. De volgende selectiecriteria zijn toegepast om *events* dicht bij de detector te selecteren: $\rho_{\mathrm{Shower}} < 300\,\mathrm{m}$ en $|z_{\mathrm{Shower}}| < 250\,\mathrm{m}$.

Twee van de belangrijkste achtergronden bij een zoektosch naar astrofysische neutrino's zijn muonen en neutrino's die ontstaan wanneer kosmische straling op de Aardatmosfeer botst. Meerdere selectiecriteria zijn ontwikkeld om deze achtergronden te onderdrukken. Omdat de Aarde atmosferische muo-

nen van de andere kant van de planeet tegenhoudt, maar transparant is voor kosmische neutrino's, is een van de selectiecriteria dat er alleen *events* gebruikt worden die als opgaand gereconstrueerd zijn. Data genomen van begin 2007 tot eind 2013 zijn geanalyseerd, overeenkomend met een levensduur van 1690.5 dagen. Uit deze data zijn in totaal 6490 muon *tracks* en 172 *shower events* geselecteerd. Het onderscheidende kenmerk van atmosferische neutrino's ten opzicht van die van een kosmische bron is dat atmosferische neutrino's isotroop verdeeld zijn over de gehele hemel, terwijl alle neutrino's van één kosmische bron uit dezelfde richting komen. De enige beperking hierbij is dat de hoekresolutie van de gebruikte reconstructie-algoritmes er voor zorgen dat de gereconstrueerde *events* verspreid raken rondom de daadwerkelijke neutrinorichting. Om een neutrinobron te kunnen identificeren staat gelijk aan het vinden van zulke clusters van *events* tussen de achtergrond van atmosferische neutrino's. Deze zoektocht is gedaan door de *likelihood ratio* te maximaliseren van de hypothese dat de data volledig uit achtergrond bestaan ten opzichte van de hypothese dat er ook signaal-*events* bij zitten. In de *likelihood* zitten de resolutie van de gereconstrueerde *events* in de vorm van de *point spread function* – die geschat wordt door middel van Monte Carlo simulaties – en de verdeling van de achtergrond over de hemel – direct verkregen uit de geobserveerde data – verweven. Atmosferische neutrino's hebben een veel zachter energiespectrum dan het E^{-2}-spectrum dat aangenomen wordt voor neutrino's van astrofysische bronnen. Daarom wordt het aantal door het reconstructie-algoritme geselecteerde hits bij elk event gebruikt om de energie van het neutrino af te schatten, om verder onderscheid te kunnen maken tussen het signaal van kosmische neutrino's en de achtergrond van atmosferische neutrino's.

De gevoeligheid van deze methode is bestudeerd door middel van pseudo-experimenten. Talloze *sky maps* zijn gegenereerd om de verdeling van events die we in de data zien na te bootsen. Daarbij werd er een variabel aantal signaalevents geïnjecteerd volgens het aangenomen E^{-2}-spectrum. De bronintensiteit (i.e. het aantal gedetecteerde signaalevents) en de positie in de hemel wordt bepaald door middel van de *maximum likelihood estimator*: de hypothese die de *likelihood function* maximaliseert. De zoektocht naar een signaal in de data is uitgevoerd met drie verschillende methoden. In de volledige hemel-zoektocht, wordt de hele hemel afgeplozen op zoek naar een puntbron die zichtbaar is als een cluster van events.

In de kandidatenlijst-zoektocht, wordt de aanwezigheid van een signaal getest voor een vooraf gedfeiniëerde lijst met 54 richtingen van bekende astrofysische objecten. Net als de volledige hemel-zoektocht, zoekt de Melkwegcentrum-

zoektocht naar een signaalcluster in een gebied rondom het Melkwegcentrum. Dit gebied is een ellips met semi-assen van 30° en 15°. Naast een zoektocht naar puntbronnen is het Melkwegcentrum getest als uitgebreide bron met breedtes tussen $0.5°$ en $5°$. In geen van de genoemde zoektochten werd er een significante signaal gevonden. De significantste cluster in de volledige hemel-zoektocht werd gevonden bij $(\alpha, \delta) = (-47.0°, -65.0°)$ met een significantie van $4.2\,\%$ en is in principe dezelfde cluster als in de vorige analyse. De bronkandidaat met de significantste cluster is HESSJ0632+057 gepositioneerd op $(\alpha, \delta) = (98.24°, 5.81°)$, met een bovengrens aan de signaalflux van $\Phi_0^{90\,\%} = 4.3 \times 10^{-8}$. Ook deze significantste kandidaat is dezelfde als in de vorige analyse. Er konden ook limieten gesteld worden voor alle andere kandidaten; dit zijn de strengste limieten op veel astrofysische objecten in het zuidelijk halfrond. Deze limieten worden samen met de gevoeligheid van ANTARES getoond in Afbeelding S.3 and vergeleken met de gevoeligheid van IceCube. Het Melkwegcentrum kon noch als puntbron, noch als uitgebreide bron geïdentificeerd worden. De grootste uitschieter van de bovengrens boven de gevoeligheid was te zien bij een afmeting van het Melkwegcentrum van 1° met een significantie (zonder correctie voor de *trials factor*) van 1.4σ.

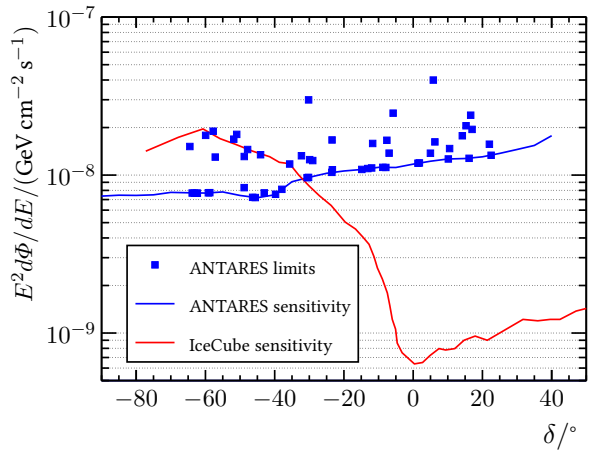

Afbeelding S.3: Gevoeligheid van de kandidatenlijst studie voor de flux van een potentiële puntbron met een E^{-2} spectrum als functie van de declinatie van de bron. De gevoeliheid van ANTARES (blauw) en IceCube (rood) zoals gegeven in [83] worden getoond. De blauwe vierkanten tonen de bovengrenzen (met 90 % C.L.) aan de potentiële neutrinoflux van de onderzochte kandidaten.

Zusammenfassung

Astronomie ist eine der ältesten Wissenschaften. Seit Urzeiten blickten die Menschen in die Sterne und versuchten zu erklären, was sie sahen. Anfangs mit nichts anderem als den bloßen Augen, später unterstützt durch Teleskope. Überall auf der Welt wurden Konstrukte errichtet, die sie dabei unterstützen sollten, die Bewegungen des Himmelsgewölbes zu verstehen; angefangen bei primitiven Steingebilden wie Stonehenge bis hin zu modernen Teleskopen, die als Satelliten die Erde umrunden. Es gibt ein weites Feld an Boten, die genutzt werden können, um ferne Objekte zu studieren; von Photonen in Form von Radiowellen, sichtbarem Licht, Röntgen- und Gammastrahlen hin zu kosmischer Strahlung, Neutrinos und die erst kürzlich direkt nachgewiesenen Gravitationswellen. Astronomie mit Photon ist bereits sehr etabliert, zu Hochpräzisionsmessungen avanciert und für eine Unmenge an phantastischen Bildern verantwortlich.

Aufgrund ihrer elektrischen Ladung werden kosmische Strahlen von galaktischen und intergalaktischen magnetischen Feldern abgelenkt, was zu völlig zufälligen Ankunftsrichtung auf der Erde führt. Zwar verkleinert sich die Ablenkung mit zunehmender Energie der Teilchen, bei den höchsten bekannten Energien kann sie trotzdem noch mehrere Grad betragen. Die Teilchen mit den höchsten jemals gemessenen Energien waren Bestandteil der kosmischen Strahlung. Allerdings ist der Teilchenfluss bei solch hohen Energien so gering, dass enorme Kollektorflächen nötig sind. Abbildung Z.1 zeigt das Energiespektrum der kosmischen Strahlung; gemessen von verschiedenen Experimenten. Das Spektrum kann mit einer Potenzfunktion mit zwei charakteristischen Umbruchstellen beschrieben werden: dem „Knie“ bei etwa $E \approx 3 \cdot 10^{15}$ GeV und dem „Knöchel“ bei $E \approx 10^{19}$ GeV. Der Grund für diese Merkmale und die Mechanismen, die subatomare Teilchen auf die beobachteten Energien beschleunigen können, sind Gegenstand aktiver Forschung. Bis heute konnten keine astrophysikalischen Objekte als Ursprung bereits beobachteter kosmischer Strahlung identifiziert werden.

Viele Modelle sagen eine Neutrinoproduktion während der Beschleunigung geladener Teilchen voraus, entweder durch Nukleon-Photon Interaktionen: $p + \gamma \to \Delta^+ \to \pi^+ + n$, oder Nukleon-Nukleon Interaktionen: $p + p \to p + n + \pi^+$, und anschließenden Pionzerfällen. Beliebte Kandidaten für diese kos-

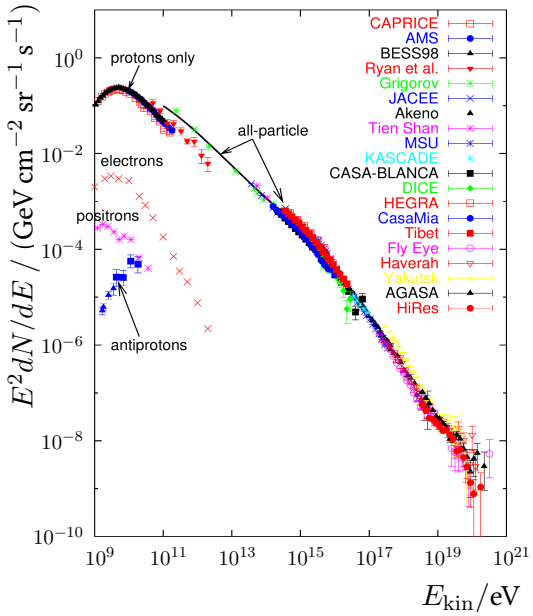

Abbildung Z.1: Das Energiespektrum verschiedener Teilchenarten, die die kosmische Strahlung bilden. Das Spektrum folgt einem Potenzgesetz mit energieabhängigen Spektralindizes. Die Umbruchstellen werden „Knie“ und „Knöchel“ genannt und liegen bei $E \approx 3 \cdot 10^{15}$ eV und $E \approx 10^{19}$ eV.
Abbildung von [15].

mischen Beschleuniger sind Supernovaüberreste, Gammastrahlenblitze und die supermassiven Schwarzen Löcher im Zentrum vieler Galaxien. Es wird erwartet, dass der Neutrinofluss, der in diesen Interaktionen produziert wird, dem Energiespektrum der kosmischen Strahlung folgt: $\frac{d\Phi_\nu}{dE} \sim E^{-2}$. Im Gegensatz zur kosmischen Strahlung werden Neutrinos nicht von magnetischen Feldern abgelenkt und zeigen genau auf ihren Ursprungsort zurück. Das Nachweisen hochenergetischer Neutrinos wäre genauso ein starker Hinweis auf die Beschleunigung kosmischer Strahlung.
Das ANTARES Neutrino Teleskop befindet sich in den Tiefen des Mittelmeers, 40 km vor der Küste Toulons in Frankreich. Es besteht aus 885 optischen Modulen, die in einem dreidimensionalen Gitter angeordnet sind und ein Volumen von $0{,}01\,\mathrm{km}^3$ einschließen. ANTARES wurde gebaut um hochenergetische Neutrinos nachzuweisen und sie einer astrophysikalischen Quelle zuzuordnen. Die Suche nach solchen Quellen ist eines der Hauptthemen, die in diesem Manuskript beschrieben werden. Um Neutrinos mit einer astrophysikalischen Quelle zu verknüpfen muss ihre Richtung aus dem Signal rekonstruiert werden, dass sie im Detektor hinterlassen. Neutrinos interagieren ausschließlich über die schwache Wechselwirkung und können nur indirekt nachgewiesen werden. So können sie W und Z Bosonen mit den Atomen des Wassers und des Felsgesteins, das den Detektor umgibt, austauschen. Viele, der in diesen Wechselwirkungen erzeugten Teilchen, sind

relativistisch und haben eine Geschwindigkeit, die höher ist als die Phasengeschwindigkeit des Lichts im Wasser. In solchen Fällen entspannen sich die Polarisierungen der Wassermoleküle, die durch diese geladenen Teilchen verursacht wurden, kohärent und strahlen Energie in Form von Tscherenkov-Photonen ab. Diese Photonen werden durch die optischen Module des Detektors aufgelesen und deren Signale zur Küstenstation gesendet, wo sie für spätere Analysen gespeichert werden.

Der Algorithmus, der zur Bestimmung der Richtung des ursprünglichen Neutrinos verwendet werden muss, hängt von der Art der Teilchens ab, die in der Wechselwirkung erzeugt werden. In dem Falle, dass ein Myon erzeugt wird, wird die eventuell kilometerlange Myonspur durch eine Likelihood-Funktion rekonstruiert, die auf den Zeitstempeln der Photondetektionen beruht. Dieser Myonrekonstruktionsalgorithmus erreicht eine Auflösung von $0{,}4^\circ$. Falls sich das Neutrino in ein Elektron umwandelt oder – im Falle eines Z Bosonaustausches – seinen Typ nicht verändert, wird ein Schauer an Elementarteilchen erzeugt. Dieser Schauer gibt seine gesamte Energie innerhalb weniger Meter als Tscherenkovlicht ab. Die Entwicklung eines Rekonstruktionsalgorithmus für ebensolche Schauerereignisse war die zweite Aufgabe dieses Promotionsprojektes. Da die Ausdehnung des Schauers, verglichen mit den Ausmaßen des Detektors, klein ist, erscheint das Zeitprofil der Photonemissionen isotropisch für weiter entfernte Module und ist für die Rekonstruktion ungeeignet. Stattdessen macht sich die implementierte Maximum-Likelihood-Funktion die Anzahl der Photonen zunutze, die auf den unterschiedlichen Detektormodulen erwartet werden. Diese Anzahl hängt von der Entfernung des Moduls zum Schauer, dem Winkel zwischen Neutrinorichtung und Richtung der Photonemission und dem Einfallswinkel des Photons auf dem optischen Modul ab. Mit dieser Methode wurde eine Richtungsauflösung von etwa 3° in dem relevanten Energiebereich zwischen 10^3 GeV und 10^6 GeV erreicht. Abbildung Z.2 zeigt die Richtungsauflösung als Funktion der Neutrinoenergie.

Zwei der Hauptuntergründe bei einer Suche nach astrophysikalischen Neutrinos sind Myonen und Neutrinos, die in der Erdatmosphäre durch die Kollisionen von Teilchen der kosmischen Strahlung erzeugt werden. Mehrere ereignisweise angewandten Selektionkriterien wurden entwickelt um diese Untegründe zu unterdrücken. Da die Erde atmosphärische Myonen effektiv abschirmt, jedoch transparent für kosmische Neutrinos ist, beinhaltet eines dieser Kriterien, dass die Ereignisse als „aufwärts gehend“ rekonstruiert werden müssen. Daten von Anfang 2007 bis Ende 2013, was einer effektiven Laufzeit von 1690.5 Tagen entspricht, wurden analysiert. Aus diesen Daten wurden 6490 Myon- und 172 Schauerereignisse ausgewählt.

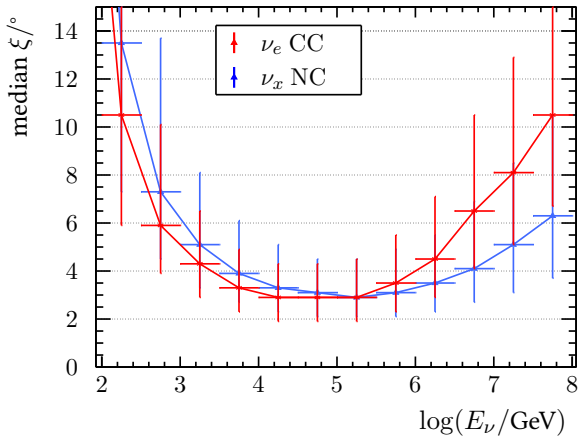

Abbildung Z.2: Der Median des Winkels ξ zwischen der rekonstruierten Richtung des Schauers und der Richtung des simulierten Neutrinos: rot für elektromagnetische Schauer und blau für hadronische Schauer. Um Ereignisse in der näheren Umgebung des Detektors auszuwählen, wurden lose Schnitte auf die rekonstruierte Position angewandt: $\rho_{\mathrm{Shower}} < 300\,\mathrm{m}$ und $|z_{\mathrm{Shower}}| < 250\,\mathrm{m}$.

Das unterscheidende Merkmal zwischen atmosphärischen Neutrinos und denen von kosmischen Quellen ist, dass atmosphärische Neutrinos gleichmäßig aus allen Richtungen kommen, während astrophysikalische Neutrinos aus der selben Richtung, eben der ihrer kosmischen Quelle, kommen. Die einzige Einschränkung zu diesem Fakt ist die Richtungsauflösung der verwendeten Rekonstruktionsalgorithmen, welche ein Streuen der rekonstruierten Richtungen um ihre wahre Richtung verursacht. Eine Neutrinoquelle zu identifizieren, bedeutet, solch eine Ansammlung an Ereignissen im Untergrund der atmosphärischen Neutrinos zu finden. Für diese Suche wurde die Methode der maximalen Likelihood-Quotienten verwendet. Hierbei wird der Quotient zwischen einer Likelihood-Funktion unter der Annahme, in den Daten befänden sich nur Untergrundereignisse, mit der Funktion unter der Annahme, es befänden sich zusätzlich auch Signalereignisse in den Daten, maximiert. Die Likelihood-Funktion berücksichtigt die Auflösung der rekonstruierten Ereignisse in Form der Punktbildfunktion, welche aus Monte Carlo Simulationen abgeschätzt wurde, und der Verteilung der Untegrundereignissen über den Himmel, wobei hier direkt die aufgezeichneten Daten verwendet wurden. Atmosphärische Neutrinos haben ein viel weicheres Energiespektrum als das für kosmische Neutrinos angenommene E^{-2}-Spektrum. Aus diesem

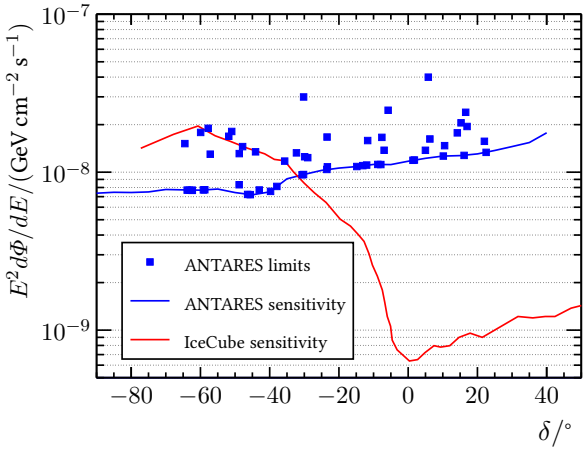

Abbildung Z.3: Obergrenzen bei 90 % Konfidenzniveau auf den Signalfluss der untersuchten Kandidaten unter Annahme eines E^{-2}-Spektrums (blaue Quadrate). Die blaue Line zeigt die ANTARES Sensitivität: die erwartete, mittlere Obergrenze. Die rote Linie zeigt die IceCube Sensitivität als Vergleich [83].

Grund wird die Anzahl an von Photonen getroffenen Detektormodulen, die von den Rekonstruktionsalgorithmen ausgewählt wurden, verwendet um die Energie des Mutterneutrinos abzuschätzen, was zusätzlich hilft, kosmisches Signal von atmosphärischem Untergrund zu unterscheiden.

Die Sensitivität dieser Methode wurde mit Pseudoexperimenten untersucht. Hierfür wurde eine große Zahl zufallsgenerierter Neutrinoereignisverteilungen erzeugt, die die Verteilung, die wir in den Daten sehen können, nachahmen. Darüber hinaus wurde eine unterschiedliche Anzahl an Signalereignissen, die dem erwarteten E^{-2}-Spektrum folgen, an bestimmten Positionen auf der Himmelskarte hinzugefügt. Die Intensität des Signals (das heißt, die Anzahl an erfassten Signalereignissen) und seine Position im Himmel wurden mit dem Maximum-Likelihood-Schätzer, die Hypothese, die die Likelihood-Funktion maximiert, bestimmt. Die Suche nach einem Signal in den Daten wurde mit drei verschiedenen Verfahren durchgeführt. In der Ganzhimmelssuche wurde der gesamte Himmel nach einer Punktquelle in Form eine Ereignisanhäufung abgesucht. Weiterhin wurde eine Liste an 54 bekannten astrophysikalischen Objekten, welche auch Kandidaten für Neutrinoproduktion sind, auf ein Neutrino Signal untersucht. Ähnlich zur Ganzhimmelssuche, wurde die Region um das Galaktische Zentrum nach möglichen Neutrinoquellen abgesucht. Diese Region wurde als Ellipse mit Halbachsen zu 30° und

15° definiert. Zusätzlich zu der Suche nach Punktquellen wurde das Galaktische Zentrum als mögliche ausgedehnte Quelle untersucht. Nirgendwo im Sichtfeld des Detektors konnte eine Neutrinoquelle gefunden werden. Die signifikanteste Ereignisanhäufung in der Ganzhimmelssuche wurde bei den Koordinaten $(\alpha, \delta) = (-47{,}0^\circ, -65{,}0^\circ)$ bei einer Signifikanz von $4{,}2\,\%$ gefunden. Dies ist im Grunde die selbe Stelle, die auch schon während der letzten Untersuchung bestimmt wurde. Der Kandidat mit der signifikantesten Signalanhäufung ist HESSJ0632+057, welcher sich bei den Koordinaten $(\alpha, \delta) = (98{,}24^\circ, 5{,}81^\circ)$ befindet. Die Obergrenze auf den Neutrinofluss von diesem Objekt wurde zu $\Phi_0^{90\,\%} = 4{,}3 \times 10^{-8}$ bestimmt. Während der vorherigen Untersuchung wurde auch dieser Kandidat bereits als der mit der signifikantesten Ereignisanhäufung identifiziert. Auch auf den möglichen Neutrinofluss von allen anderen Kandidaten konnten Obergrenzen bestimmt werden. Für viele Objekte in der südlichen Hemisphäre sind dies die restriktivsten Grenzen zur Zeit. Diese Obergrenzen und die ANTARES Sensitivität auf Punktquellen sind zusammen mit der Sensitivität des IceCube Detektors in Abbildung Z.3 gezeigt. Das Galaktische Zentrum konnte weder als Punktquelle noch als ausgedehnte Neutrinoquelle identifiziert werden. Der höchste Exzess über dem Erwartungswert wurde jedoch für eine Ausdehnung von 1° mit einer Signifikanz von 1.4σ gefunden.

Acknowledgements

"What should we do next? Somethin' good? Somethin' bad? Bit of both?"
Peter Quill – Guardians of the Galaxy

After such a four-year journey it is all but inevitable to meet numerous persons who shape you as a person and a researcher, your work and ultimately the manuscript that is your dissertation. First and foremost I have to thank Aart Heijboer for taking me on as a PhD candidate. His expertise on hypothesis testing and code design taught me a lot and will prove invaluable for my future work. I also learned a lot from the many discussions with Ronald Bruijn, Maarten de Jong, Paul Kooijmann and Dorothea Samtleben and their constant pushing to "try harder" and improve myself. Without you, many of the presented results wouldn't be in the shape they are. Special thanks go to Stephan Schulte who introduced me to the work flow of the ANTARES data framework and always had an open ear for my questions and problems. The whole rest of our group at Nikhef deserves mentioning as well. The innumerable discussions at the coffee table, our board game nights and all our activities outside Nikhef will always stay with me. Thanks, Arien, Claudio, Daan, Erwin, Karel, Martijn, Robert and Tri.

There are way too many people from the other groups and experiments here at Nikhef to mention them all by name. I hope you can forgive me for not starting this list that is bound to be incomplete. Rest assure that I will never forget my time with you here at Nikhef.

Being part of the international collaborations that are the ANTARES and KM3NeT experiments, I met many outstanding personalities. Lots of them deserve my thanks for working on various other tasks and ensuring that I could do my work and for providing a great atmosphere during our collaboration meetings: Antoine, Bruny, Fabian, Julia, Jürgen, Luigi, Mora, Paschal, Thomas, and Veronique, only to name a few.

I am particularly grateful for Agata Trovato who made sure that I did not lose my mind during the last months of this project. It goes almost without saying that I am forever in debt to my parents and the rest of my family for never doubting my choices and always supporting me on my endeavours.

Bibliography

[1] E.C. Krupp. *Echoes of the Ancient Skies: The Astronomy of Lost Civilizations*. Astronomy Series. Dover Publications, 2003. (cited on page 1)

[2] C.L.N. Ruggles. *Ancient Astronomy*. 2005. (cited on page 1)

[3] E.C. Krupp. *Light in the Temples*. 1988. in C.L.N. Ruggles: Records in Stone: Papers in Memory of Alexander Thom. (cited on page 1)

[4] V. F. Hess. Über Beobachtungen der durchdringenden Strahlung bei sieben Freiballonfahrten. *Physikalische Zeitschrift*, 13:1084–1091, 1912. (cited on page 3)

[5] K. Hirata, T. Kajita, M. Koshiba, M. Nakahata, and Y. Oyama. Observation of a neutrino burst from the supernova SN1987A. *Physical Review Letters*, 58:1490–1493, 1987. (cited on page 3)

[6] R. M. Bionta, G. Blewitt, C. B. Bratton, D. Casper, and A. Ciocio. Observation of a neutrino burst in coincidence with supernova 1987A in the Large Magellanic Cloud. *Physical Review Letters*, 58:1494–1496, 1987. (cited on page 3)

[7] B. T. Cleveland, Timothy Daily, Raymond Davis Jr., James R. Distel, Kenneth Lande, C. K. Lee, Paul S. Wildenhain and Jack Ullman . Measurement of the solar electron neutrino flux with the Homestake chlorine detector. *The Astrophysical Journal*, 496:505–526, 1998. (cited on page 3)

[8] A. B. Balantekin and W. C. Haxton. Neutrino oscillations. *Progress in Particle and Nuclear Physics*, 71:150–161, 2013. (cited on page 3)

[9] The SNO Collaboration. Measurement of the rate of $\nu_e + d \rightarrow p + p + e^-$ interactions produced by ^{8}B solar neutrinos at the Sudbury Neutrino Observatory. *Physical Review Letters*, 87:071301, 2001. (cited on page 3)

[10] The IceCube Collaboration. Observation of High-Energy Astrophysical Neutrinos in Three Years of IceCube Data. *Physical Review Letters*, 113:101101, 2014. (cited on pages 4, 14, 15, 90, and 101)

[11] K.v. Meyenn. *Wissenschaftlicher Briefwechsel mit Bohr, Einstein, Heisenberg u.a. Band II: 1930–1939*. Springer-Verlag Berlin Heidelberg, 1985. (cited on page 5)

[12] C. L. Cowan, F. Reines, F. B. Harrison et al. Detection of the Free Neutrino: A Confirmation. *Science*, 124:103–104, 1956. (cited on page 5)

[13] G. Danby, J.-M. Gaillard, K. Goulianos et al. Observation of High-Energy Neutrino Reactions and the Existence of Two Kinds of Neutrinos. *Physical Review Letters*, 9:36–44, 1962. (cited on page 5)

[14] DONUT Collaboration, K. Kodama, N. Ushida et al. Observation of tau neutrino interactions. *Physics Letters B*, 504:218–224, 2001. (cited on page 5)

[15] A. M. Hillas. Cosmic Rays: Recent Progress and some Current Questions. 2006. arXiv:astro-ph/0607109 and therein. (cited on pages 7, 108, 114, and 120)

[16] Pierre Auger Collaboration. Properties and performance of the prototype instrument for the Pierre Auger Observatory. *Nuclear Instruments and Methods*, A523:50–95, 2004. (cited on page 6)

[17] The Pierre Auger Collaboration. Update on the correlation of the highest energy cosmic rays with nearby extragalactic matter. *Astroparticle Physics*, 34:314–326, 2010. (cited on pages 7 and 8)

[18] Particle Data Group. 2015 Review of Particle Physics. *Chinese Physics C*, 38, 2014 and 2015 update. (cited on pages 7 and 21)

[19] Enrico Fermi. Galactic magnetic fields and the origin of cosmic radiation. *The Astrophysical Journal*, 119, 1954. (cited on page 7)

[20] G. F. Krymskii. A regular mechanism for the acceleration of charged particles on the front of a shock wave. *Akademiia Nauk SSSR Doklady*, 234:1306–1308, 1977. (cited on page 8)

[21] V.L. Ginzburg, Y.M. Khazan and V.S. Ptuskin. Origin of Cosmic Rays: Galactic Models with Halo - I. Proton Nucleon Component. *Astrophysics and Space Science*, 68:295–314, 1980. (cited on page 8)

[22] F. Aharonian et al. Detection of TeV γ-ray emission from the shell-type supernova remnant RX J0852.0-4622 with H.E.S.S. *Astronomy and Astrophysics*, 437:L7–L10, 2005. (cited on page 9)

[23] F. Aharonian et al. A detailed spectral and morphological study of the gamma-ray supernova remnant RX J1713.7-3946. *Astronomy and Astrophysics*, 449:223–242, 2006. (cited on page 9)

[24] T.C. Weekes et al. Observation of TeV gamma rays from the crab nebula using the atmospheric Cerenkov Imaging Technique. *The Astrophysical Journal*, 342:379–395, 1989. (cited on page 9)

[25] The H.E.S.S. Collaboration. First detection of a VHE gamma-ray spectral maximum from a cosmic source: H.E.S.S. discovery of the Vela X nebula. *Astronomy and Astrophysics*, 448:L43–L47, 2006. (cited on page 10)

[26] W Bednarek. Neutrinos from the pulsar wind nebulae. *Astronomy and Astrophysics*, 407:1–6, 2003. (cited on page 10)

[27] C. Distefano, D. Guetta, Eli Waxman et al. Neutrino Flux Predictions for known Galactic Microquasars. *The Astrophysical Journal*, 575:378, 2002. (cited on page 10)

[28] The H.E.S.S. Collaboration. The H.E.S.S. Survey of the inner galaxy in very high-energy gamma-rays. *The Astrophysical Journal*, 636:777–797, 2008. (cited on page 10)

[29] Gregory Dobler, Douglas P. Finkbeiner, Ilias Cholis, Tracy Slatyer and Neal Weiner. The *Fermi* Haze: A Gamma-Ray Counterpart to the Microwave Haze. *The Astrophysical Journal*, 717:825, 2010. (cited on page 10)

[30] Meng Su, Tracy R. Slatyer, and Douglas P. Finkbeiner. Giant Gamma-Ray Bubbles From *Fermi*-LAT: Active Galactic Nucleus Activity or bipolar Galactic Wind? *The Astrophysical Journal*, 724:1044, 2010. (cited on page 10)

[31] Demosthenes Kazanas, Kelgo Fukumura, Ehud Behar, Ioannis Contopou-Los, and Chris Shrader. Toward a Unified AGN Structure. *Astronomical Review*, 7:92–123, 2012. (cited on page 10)

[32] Tsvi Piran. Gamma-Ray Bursts and the Fireball Model. *Physics Reports*, 314:575–667, 1999. (cited on page 11)

[33] B. Gendre, G. Stratta, J.L. Atteia et al. The ultra-long Gamma-Ray Burst 111209A: the collapse of a blue supergiant? *The Astrophysical Journal*, 766:30, 2013. (cited on page 11)

[34] E. Waxman. Cosmological gamma-ray bursts and the highest energy cosmic rays. *Physical Review Letters*, 75:386–389, 1995. (cited on page 11)

[35] K. Greisen. End to the cosmic ray spectrum? *Physical Review Letters*, 16:748–750, 1966. (cited on page 11)

[36] G. T. Zatsepin and V. A. Kuzmin. Upper limit of the spectrum of cosmic rays. *Journal of Experimental and Theoretical Physics Letters*, 4:78–80, 1966. (cited on page 11)

[37] Lukas Nellen, Karl Mannheim and Peter L. Biermann. Neutrino production through hadronic cascades in AGN accretion disks. *Physical Review D*, 47:5270–5274, 1993. (cited on page 12)

[38] Z. Maki, M. Nakagawa and S. Sakata. Remarks on the Unified Model of Elementary Particles. *Progress of Theoretical Physics*, 28:870–880, 1962. (cited on page 13)

[39] B. Pontecorvo. Neutrino Experiments and the Problem of Conservation of Leptonic Charge. *Zh. Eksp. Teor. Fiz.*, 53:1717–1725, 1967. (cited on page 13)

[40] John G Learned and Sandip Pakvasa. Detecting ν_τ oscillations at PeV energies. *Astroparticle Physics*, 3:267–274, 1995. (cited on page 13)

[41] Raj Gandhi, Chris Quigg, Mary Hall Reno, and Ina Sarcevic. Neutrino interactions at ultrahigh energies. *Physical Review D*, 58:093009, 1998. (cited on page 18)

[42] The ANTARES Collaboration. A Deep Sea Telescope for High Energy Neutrinos. arxiv:astro-ph/9907432. (cited on page 18)

[43] E. Bugaev S. Klimushin and I. Sokalski. Precise parametrizations of muon energy losses in water. In *Proceedings of the 28th International Cosmic Ray Conference*, 2001. (cited on page 20)

[44] The ANTARES Collaboration. ANTARES: the first undersea neutrino telescope. *Nuclear Instruments and Methods*, A656:11–38, 2011. (cited on page 22)

[45] The ANTARES Collaboration. AMADEUS - The Acoustic Neutrino Detection Test System of the ANTARES Deep-Sea Neutrino Telescope. *Nuclear Instruments and Methods A*, 626:128–143, 2011. (cited on page 23)

[46] The ANTARES Collaboration. The ANTARES optical module. *Nuclear Instruments and Methods A*, 484:369–383, 2002. (cited on pages 24 and 40)

[47] The ANTARES Collaboration. Study of large hemispherical photomultiplier tubes for the ANTARES neutrino telescope. *Nuclear Instruments and Methods in Physics Research Section A*, 555:132–141, 2005. (cited on page 24)

[48] The ANTARES Collaboration. The positioning system of the ANTARES Neutrino Telescope. *Journal of Instrumentation*, 7:T08002, 2012. (cited on page 28)

[49] The ANTARES Collaboration. Time calibration of the ANTARES neutrino telescope. *Astroparticle Physics*, 34:539–549, 2011. (cited on pages 28 and 40)

[50] Maria Laura Costantini and Francesco Vissani. Expected neutrino signal from supernova remnant RX J1713.7-3946 and flavor oscillations. *Astroparticle Physics*, 23:477–485, 2005. (cited on page 31)

[51] D. Bailey. *Monte Carlo tools and analysis methods for understanding the ANTARES experiment and predicting its sensitivity to Dark Matter*. PhD thesis, Wolfson College, Oxford, 2002. (cited on page 32)

[52] Y. Becherini et al. A parametrisation of single and multiple muons in the deep water or ice. *Astroparticle Physics*, 25:1–13, 2006. (cited on pages 32, 47, and 64)

[53] A. Margiotta G. Carminati and M. Spurio. Atmospheric MUons from PArametric formulas: A Fast GEnerator for neutrino telescopes (MUPAGE). *Computer Physics Communications*, 179:915–923, 2008. (cited on pages 32 and 47)

[54] Vivek Agrawal, T. K. Gaisser, Paolo Lipari, Todor Stanev. Atmospheric neutrino flux above 1 GeV. *Physical Review D*, 53:1314–1323, 1996. (cited on page 32)

[55] *GEANT program manual, CERN program library long writeup, W5013*, 1993. (cited on page 33)

[56] Maarten de Jong. The ANTARES Trigger Software, 2005. ANTARES Internal Note. (cited on page 33)

[57] Adrian J. Heijboer. *Track Reconstruction and Point Source Searches with ANTARES*. PhD thesis, 2004. (cited on pages 34 and 36)

[58] Claudio Bogazzi. *Search for cosmic neutrinos with ANTARES*. PhD thesis, Nikhef, 2014. (cited on pages 86 and 88)

[59] KM3NeT Technical Design Report [ISBN 978-90-6488-033-9]. (cited on page 39)

[60] The KM3NeT Collaboration. Letter of Intent for KM3NeT2.0. arXiv:1601.07459 [astro-ph.IM], 2016. (cited on page 39)

[61] The KM3NeT Collaboration. Deep sea tests of a prototype of the KM3NeT digital optical module. *The European Physical Journal C*, 74(9):1–8, 2014. (cited on page 39)

[62] The KM3NeT Collaboration. Expansion cone for the 3-inch PMTs of the KM3NeT optical modules. *Journal of Instrumentation*, 8:T03006, 2013. (cited on page 40)

[63] P. Timmer et al. Very low power, high voltage base for a Photo Multiplier Tube for the KM3NeT deep sea neutrino telescope. *Journal of Instrumentation*, 5(12):C12049, 2010. (cited on page 40)

[64] J. Hogenbirk et al. A photonic readout and data acquisition system for deep-sea neutrino telescopes. *Nuclear Instruments and Methods A*, 626-627 Supplement:S166–S168, 2011. (cited on page 40)

[65] A. Belias and K. Manolopoulos. Readout and data acquisition for KM3NeT. *AIP Conference Proceedings*, 1535:260–264, 2013. (cited on page 40)

[66] S. Aiello et al. The optical modules of the phase-2 of the NEMO project. *Journal of Instrumentation*, 8(07):P07001, 2013. (cited on page 40)

[67] E.G. Anassontzis et al. The optical module for the NESTOR neutrino telescope. *Nuclear Instruments and Methods A*, 479:439–455, 2002. (cited on page 40)

[68] The ANTARES Collaboration. The ANTARES optical beacon system. *Nuclear Instruments and Methods in Physics A*, 578:498–509, 2007. (cited on page 40)

[69] Jürgen Brunner. e-mail correspondence. (cited on page 47)

[70] The KM3NeT Collaboration. The prototype detection unit of the KM3NeT detector. *European Physical Journal C*, 76:1–12, 2016. (cited on pages 49 and 50)

[71] Karel Melis. Nikhef, internal correspondence. (cited on page 50)

[72] Claudio Kopper. *Performance Studies for the KM3NeT Neutrino Telescope*. PhD thesis, ECAP, 2010. (cited on pages 51 and 52)

[73] G. Cowan. *Statistical Data Analysis*. Oxford science publications. Clarendon Press, 1998. (cited on pages 55, 77, and 78)

[74] The ROOT Data Analysis Framework. `www.root.cern.ch`. (cited on pages 56 and 84)

[75] The ROOT Data Analysis Framework – TH3::Interpolate(Double_t x, Double_t y, Double_t z). (cited on page 60)

[76] The ANTARES Collaboration. Searches for Point-like and Extended Neutrino Sources Close to the Galactic Center Using the ANTARES Neutrino Telescope. *The Astrophysical Journal Letters*, 786(1):L5, 2014. (cited on pages 69 and 94)

[77] Erwin L. Visser. *Neutrinos from the Milky Way*. PhD thesis, Nikhef, 2015. (cited on page 70)

[78] F. James. *Statistical Methods in Experimental Physics*. World Scientific Publishing, 2006. (cited on page 77)

[79] J. Neyman and E. S. Pearson. On the problem of the most efficient tests of statistical hypotheses. *Philosophical Transactions of the Royal Society of London A: Mathematical, Physical and Engineering Sciences*, 231(694-706):289–337, 1933. (cited on pages 77 and 78)

[80] Claudio Bogazzi and Aart Heijboer. Point Source Search with 2007-2010 data v3. Internal Note. (cited on page 83)

[81] Garabed Halladjian. *Recherche de neutrinos cosmiques de haute-énergie émis par des sources ponctuelles avec ANTARES*. PhD thesis, 2010. (cited on page 86)

[82] Antoine Kouchner. Antares : étalonnage de l'électronique frontale, étude de muons atmosphériques, et recherche de neutrinos cosmiques. Habilitation, Diderot U., Paris, 2010. (cited on page 86)

[83] The IceCube Collaboration. Searches for Extended and Point-like Neutrino Sources with Four Years of IceCube Data. *The Astrophysical Journal*, 796(2):109. (cited on pages 91, 98, 99, 103, 110, 117, and 123)

[84] The IceCube Collaboration. Observation of Astrophysical Neutrinos in Four Years of IceCube Data. arXiv:1510.05223 [astro-ph.HE]. (cited on pages 91 and 103)

[85] J. G. Bolton, P. W. Butler. The Parkes 2700 MHz Survey (Eighth Part): Catalogue for the Declination zone $-65°$ to $-75°$. *Austrialian Journal of Physics Supplement*, 34:33, 1975. (cited on page 96)

[86] George O. Abell. The Distribution of Rich Clusters of Galaxies. *Astrophysical Journal Supplement*, 3:211, 1958. (cited on page 96)

[87] Fabian Schüssler. Multiwavelength study of the region around the ANTARES neutrino excess. In *Proceedings of the 33rd International Cosmic Ray Conference*, 2013. (cited on pages 96 and 97)

[88] R. J. White. The Sensitivity of KM3NeT to Potential Neutrino Signals from Extragalactic Gamma-Ray Sources. In *Proceedings of the 30th International Cosmic Ray Conference*, 2007. (cited on page 96)

[89] The ANTARES and IceCube Collaborations. First combined search for neutrino point-sources in the Southern Hemisphere with the ANTARES and IceCube neutrino telescopes. 2015. arXiv:1511.02149 [hep-ex], submitted to Astroparticle Physics. (cited on page 106)